

ALMA MATER STUDIORUM · UNIVERSITÀ DI BOLOGNA

Scuola di Scienze
Corso di Laurea Magistrale in Fisica del Sistema Terra

Geodetic strain rates and seismicity rates along the Apennines

Relatore:
Prof.ssa M. E. Belardinelli

Presentata da:
Riccardo Nucci

Correlatore:
Dott. Enrico Serpelloni

Sessione II
Anno Accademico 2020/2021

Abstract

The Apennines are a tectonically active belt that was site of strong historical earthquakes, including the recent L'Aquila (2009) and Amatrice-Visso-Norcia seismic sequences (2016-2017). Interseismic strain build-up is now precisely measurable using space geodetic techniques. On the other hand, the increasing density of GPS stations permits us to estimate the horizontal strain rate with greater spatial resolution than in the past. In this thesis I study the correlation between horizontal geodetic strain rates and seismicity rates through the Apennines, studying possible implications for seismic hazard assessment. I use a new GPS velocity dataset to analyze the state of deformation through computations of the strain rate field. I use three algorithms for this computation, already described in the scientific literature, and discuss strengths and limitations of each one. I select one strain rate map over the others and I develop an analysis following the approach of a recent study to investigate the relationship between observed strain rates and seismicity rates along the Apennines, verifying if the hypotheses that sustain the approach are verified. In particular, I discuss if the geodetic strain rate is representative of the strain that causes earthquakes through comparison between moment tensors of past earthquakes and estimated geodetic strain rate tensors. I compute the background seismicity rates from a recent earthquake catalog for Italy and test if independent events follow a Poisson process in time. Finally, I divide the region in different deformation areas based on strain rate values and I analyze the distribution of background seismicity in these domains, correlating the seismicity rate with the geodetic strain rate. The relationship between seismicity rate and strain rate is approximately linear but with an important dependence on the resolution of the strain rate map. I describe the implications on eventual computation of quantities that define the seismogenic potential analyzing which parameters of the approach influence the results.

Sommario

Gli Appennini sono una regione tettonicamente attiva che è stata luogo di forti terremoti storici in passato, tra i quali il recente L'Aquila (2009) e le sequenze di Amatrice-Visso-Norcia (2016-2017). L'accumulo di deformazione durante la fase intersismica è oggi misurabile con precisione attraverso le tecniche geodetiche. D'altra parte, una densità di stazioni GPS sempre maggiore permette di stimare il tasso di deformazione orizzontale con più risoluzione spaziale che in passato. In questa tesi studio la correlazione tra tassi di deformazione geodetica orizzontale e tassi di sismicità negli Appennini, esaminando possibili implicazioni per valutazioni del potenziale sismogenico. Uso un nuovo dataset di velocità GPS analizzando lo stato di deformazione attraverso il calcolo dello strain rate geodetico. Per questo calcolo utilizzo tre algoritmi, tra quelli presenti in letteratura scientifica, e discuto punti di forza e limitazioni di ciascuno. Seleziono poi una mappa di strain rate tra le altre e sviluppo un'analisi seguendo l'approccio di uno studio recente per investigare la relazione tra tassi di sismicità e tassi di deformazione lungo la catena Appenninica. Per farlo, verifico se le ipotesi che sostengono l'approccio sono verificate. In particolare, discuto se lo strain geodetico calcolato è rappresentativo della deformazione che causa i terremoti durante la fase cosismica. Per prima cosa confronto lo strain rate geodetico e tensori momento di terremoti passati. Calcolo poi la sismicità di background a partire da un nuovo catalogo sismico per l'Italia e testo se gli eventi indipendenti seguono un processo di Poisson nel tempo. Infine, divido la regione di studio in aree a diversa deformazione sulla base dei tassi di deformazione e analizzando la distribuzione della sismicità di background in questi eventi e analizzando la relazione tra tassi di deformazione e tassi sismicità. Mostro che vi è una relazione è approssimativamente lineare ma con una dipendenza importante dalla risoluzione della mappa di strain rate. Descrivo poi alcune implicazioni che questa relazione avrebbe su stime di due quantità che concorrono a definire il potenziale sismogenico analizzando quali sono i parametri all'interno dell'approccio che possono influenzare maggiormente dette stime.

Contents

1	Introduction	1
2	Method introduction	4
2.1	The Geodetic Strain Rate	4
2.2	Seismic Cycle and Moment	6
2.3	Gutenberg-Richter law and Moment conservation	9
2.4	Coulomb failure model and Kostrov equation	13
3	Velocity field from GPS data	15
3.1	GPS dataset	15
3.2	Filtering and analysis of the GPS velocity field	18
4	Computation of geodetic strain rate	24
4.1	The nearest neighbors algorithm	24
4.2	The VISR algorithm	30
4.3	Wavelets method	40
4.4	Discussion of the resulting strain rate field	50
5	Comparison of seismic and geodetic strain rate	54
6	Earthquake catalogue declustering and Poisson distribution assumption	62
6.1	Declustering method description	62
6.2	Implementation and results	64
6.3	Poisson distribution verification	74
7	Relationship between strain rate and seismicity rate	76
7.1	Spatial density of earthquakes and strain rate	76
7.2	Strain rate and seismicity rate	84
7.3	Implications for seismic hazard estimates	89
8	Conclusions and future developments	93
	Bibliography	98

Chapter 1

Introduction

Improvements in geodesy and geodetic techniques permit us to measure the Earth's surface displacements with sub-millimeter precision. In Italy, the growing density of continuously-recording Global Positioning System (GPS) stations can be employed to map with great accuracy the surface strain rate during the interseismic phase of the earthquake cycle. This information is used to understand where and to what extent deformation is accumulated and can provide important constraints for seismic hazard models.

The probabilistic seismic hazard analysis (PSHA) aims to combine information of different nature, such as seismic catalogs, geological information on active faults and focal mechanisms of past earthquakes, in order to describe the distribution of the future shaking, that may occur at a site. A fundamental challenge in PSHA is to quantify and combine different types of uncertainties. In Italy, the latest *Italian seismic hazard model* (MPS19, Meletti et al. 2021) contains two geodetically-derived earthquake rate models in which seismicity rates are derived from the geodetic strain rate field. These models provide a different and independent level of information with respect to other models, since they are almost completely independent from the Italian Parametric Earthquake Catalogue (CPTI15, Rovida et al. 2022). Even for the importance in hazard estimates, the development of reliable geodetic models is an active present-day challenge of research.

The Apennines are dominated by extensional deformation that is measured by seismology, observing a prevalence of extensional focal mechanisms, by geology, given the presence of normal faults, and by geodesy, from the surface velocity field. In the outer part of the chain, on the Adriatic side, compression tectonics occur in the correspondence of the northern Apennine arc (Pondrelli et al. 2020). The Apennines are sites of strong historical and instrumental seismicity and were place of recent destructive earthquakes: L'Aquila in 2009, the 2012 Emilia seismic sequence and 2016-2017 sequence in central Italy. This thesis focuses on the Apennines chain and has a dual purpose: 1) to explore different methods to compute

strain rates from the GPS velocity field and 2) to investigate the correlation between seismicity and geodetic strain rate and its implications in possible evaluation of seismogenic potential.

Using a new GPS velocity dataset, three methods to estimate the strain rate field from GPS velocity field are tested, from the most widely used, and pros and cons of each method are examined. Then, part of the method outlined by Stevens and Avouac 2021 for the India-Asia collision zone is applied to the Apennines. The whole method can lead to a seismicity model that relies on geodetic deformation and that can be used for probabilistic seismic hazard analyses. In this thesis, we examine if the hypothesis of the method are fulfilled and focus on the discussion of the relationship between geodetic strain rate and seismicity rate. These hypotheses closely follow the ones presented in Stevens and Avouac 2021 and are numerated and summarized in the followings.

1. The interseismic loading is stationary.

The time series, derived by GPS observation and considered in this thesis, are at least 6 years long; station velocities estimated from these time series overall cover a time-span of 26 years. The hypothesis is that the geodetic strain rate, that can be computed from this velocity dataset, is representative of the tectonic loading distribution that has driven past seismicity and that will drive the future one.

2. The geodetic strain rate reflects the stress rate on the seismogenic faults.

The stress field in the Apennines has a variability that causes an uneven pattern of earthquake focal mechanisms. In fully elastic conditions one can expect the stress rate to be proportional to the geodetic strain rate. The hypothesis can hold if the geodetic data have enough spatial resolution to represent the elastic loading on the faults, caused by heterogeneity of the stress field.

3. Earthquakes are triggered by the tectonic stresses or by stress changes induced by previous earthquakes. With the term *background seismicity* one refers to earthquakes driven by interseismic loading, while the terms *dependent seismicity* refers to aftershocks or earthquake sequences. Background seismicity is assumed to contains independent events that follow a Poisson process in time.

In the case of the Apennines' seismicity, background seismicity will be identified and the poissonian distribution of its inter-event times will be verified.

4. The earthquake spatial distribution has a spatial density that depends, at first order, on the level of the deformation rate.

This hypothesis states that we can ignore, at the first order, the spatial geometry and distribution of the faults and focus on the geodetic deformation rate to analyze seismicity.

5. The rate of earthquake nucleation is proportional to the stress rate.

Such a relationship is expected from the Coulomb failure model and from more complicated models (as the *rate and state* models). On the other hand, following the hypothesis 2, if the stress rate is proportional to geodetic strain rate, we expect a linear relationship between geodetic strain rate and seismicity rate. A key point of this thesis is proving that, for the Apennines, there is a correlation between strain rate and seismicity rate.

In chapter 2, the main theoretical concepts used in this thesis are presented. Chapter 3 exposes the GPS velocity dataset used in this work and how it was used in order to estimate reliable strain rate fields. In chapter 4, three methods to compute the strain rate field are examined and one method is chosen over the other in the subsequent analyses. Chapter 5 discusses if the geodetic strain rate is representative of the accumulating elastic strain that earthquakes release (hypothesis 1 and 2). The chapter 6 is about the declustering of the considered seismic catalog and the verification that independent event follow a Poisson process in time (hypothesis 3). Last, chapter 7 examines the dependence of the spatial distribution of seismicity on the deformation rate (hypothesis 4) and the relationship between strain rates and seismicity rates (hypothesis 5). Finally, the implications of this relationship on the seismogenic potential is discussed.

Chapter 2

Method introduction

In this chapter, part of the concepts and equations used in this thesis are presented. In section 2.1 the strain rate and its invariants are presented. In section 2.2 the concept of earthquake cycle is exposed. In section 2.3 I derive a form of seismic moment conservation already proposed in literature (Stevens and Avouac 2021), providing a constraint on the maximum magnitude earthquake. The section 2.4 concerns the Coulomb failure model according to which Ader et al. 2014 proposed a linear relationship between seismicity rate and stress rate.

2.1 The Geodetic Strain Rate

In this thesis the theoretical background is based on the *theory of elasticity*, as a mean to explain the deformation at which the Earth crust is subjected. The fundamental equation in this theory is the relationship between the stress tensor σ_{ij} and the strain tensor ϵ_{kl} in an elastic medium:

$$\sigma_{ij} = C_{ijkl}\epsilon_{kl} \quad (2.1)$$

where the fourth-order tensor C_{ijkl} summarizes the elastic proprieties of the medium (which is called tensor of elastic constants) and the second-order strain tensor ϵ_{kl} is defined from the spatial gradients of the displacement vector u_i as:

$$\epsilon_{kl} = \frac{1}{2} \left(\frac{\partial u_k}{\partial x_l} + \frac{\partial u_l}{\partial x_k} \right) \quad (2.2)$$

From the definition of the strain tensor clearly results that $\epsilon_{ij} = \epsilon_{ji}$, i.e. the strain is a symmetric tensor. If an homogeneous and isotropic elastic medium is considered, the equation (2.1) simplifies into a form described by the Lamé elastic

parameters λ and μ for the medium:

$$\sigma_{ij} = \lambda \epsilon_{kk} \delta_{ij} + 2\mu \epsilon_{ij} \quad (2.3)$$

Advancements in geodesy and in geodetic techniques permit us to measure displacements at the Earth surface with great accuracy. In this thesis we consider velocity estimates obtained from the analysis of several years of GPS measurements of ground displacements in the Apennines. The main physical quantity that can be obtained from these data, of interest for this work and for any seismotectonic application of GPS velocities, is the *geodetic strain rate*, defined as the spatial derivative of the strain rate tensor in (2.2) with respect to time:

$$\dot{\epsilon}_{ij} = \frac{1}{2} \left(\frac{\partial v_i}{\partial x_j} + \frac{\partial v_j}{\partial x_i} \right) \quad (2.4)$$

where v_i is the velocity field that can be measured at the Earth surface. Actually, the GPS geodetic data are *discrete* in space; this means that the values of the velocity field are known at the positions of GPS instruments. From this, different algorithms exist, that compute the strain rate field from the knowledge of positions and velocities of GPS geodetic stations. In general, different techniques provide different estimates of geodetic strain rate. A purpose of this thesis is to use different algorithms, among the most widely used, to compute the continuous velocity field and then the geodetic strain rate, discussing the impact of each method on the final geodetic strain rate map and evaluating how to select a map among the others.

In the analysis of the velocity data, only the horizontal components of the velocity field are considered in this work. The definition of the geodetic strain rate in (2.2) then holds for $i, j = 1, 2$ (indices that label the horizontal axes).

The geodetic strain rate tensor in (2.4) depends on the velocity field v_i at the Earth surface that is the result of GPS velocity measures performed with respect to a certain *reference frame*. This means that the geodetic strain rate itself is a physical quantity related to the same reference frame. The *invariants* of the geodetic strain rate are scalar quantities that don't change from one reference frame to another. For a second-order tensor, three principal independent scalar invariants exist; in this thesis we consider the first invariant (*dilatation*) D and the second invariant I_2 of the geodetic strain rate $\dot{\epsilon}_{ij}$ that are defined as:

$$D = \dot{\epsilon}_{kk} \quad (2.5a)$$

$$I_2 = \sqrt{\dot{\epsilon}_{ij} \dot{\epsilon}_{ij}} \quad (2.5b)$$

These definitions will be used in chapter 4 in order to treat the intrinsic character-

istics of the deformation rate that don't depend on the choice of a reference frame for velocities. Assuming plain strain deformation with the vertical axis as the axis of translational invariance, the previous equations reduce to:

$$D = \dot{\epsilon}_{11} + \dot{\epsilon}_{22} \quad (2.6a)$$

$$I_2 = \sqrt{\dot{\epsilon}_{11}^2 + \dot{\epsilon}_{22}^2 + 2\dot{\epsilon}_{12}^2} \quad (2.6b)$$

2.2 Seismic Cycle and Moment

In this thesis we rely on a generalized form of Reid's elastic rebound theory. The original theory states that earthquakes release elastic strain that is accumulated before their occurrence. We can recognize earthquake occurrence as part of a *cycle* composed of different phases (see Figure 2.1):

- The first phase is called *interseismic*. It coincides in time with the period between earthquakes and it is characterized by strain accumulation near the fault structures. The strain build-up, assumed to be linear in time, is caused by partial or total locking of the faults together with the long term motion imposed by plate tectonics.
- The second is called *coseismic* and happens with earthquakes occurrence. During this phase, part of the accumulated budget of strain is released through relative displacements of the neighboring portions of the fault. In a simplified way we can say that a seismic event starts on a fault when the shear stress on the fault surface reaches a certain threshold value (see section 2.4).
- The third is the *postseismic* phase that follows a seismic event. It is a period of transient deformation that can be caused by several processes (e.g. afterslip, viscoelastic relaxation or pore-fluid migration). The strain is released through timescales ranging from days to decades, depending on the driving process.

In this study, focused on the Apennines, any type of periodical behavior of earthquakes' occurrence is not assumed. Instead, this conceptual model is used to formalize the idea that, as average over the long term, coseismic and postseismic phases release the elastic strain that is accumulated during the interseismic phase. It is important to note that not all the deformation accumulated during the interseismic phase is released seismically, i.e. radiating seismic waves. For example, aseismic slip can result from postseismic relaxation (afterslip) or spontaneous slip events (Avouac 2015). This behaviour will be taken into account in section 2.3.

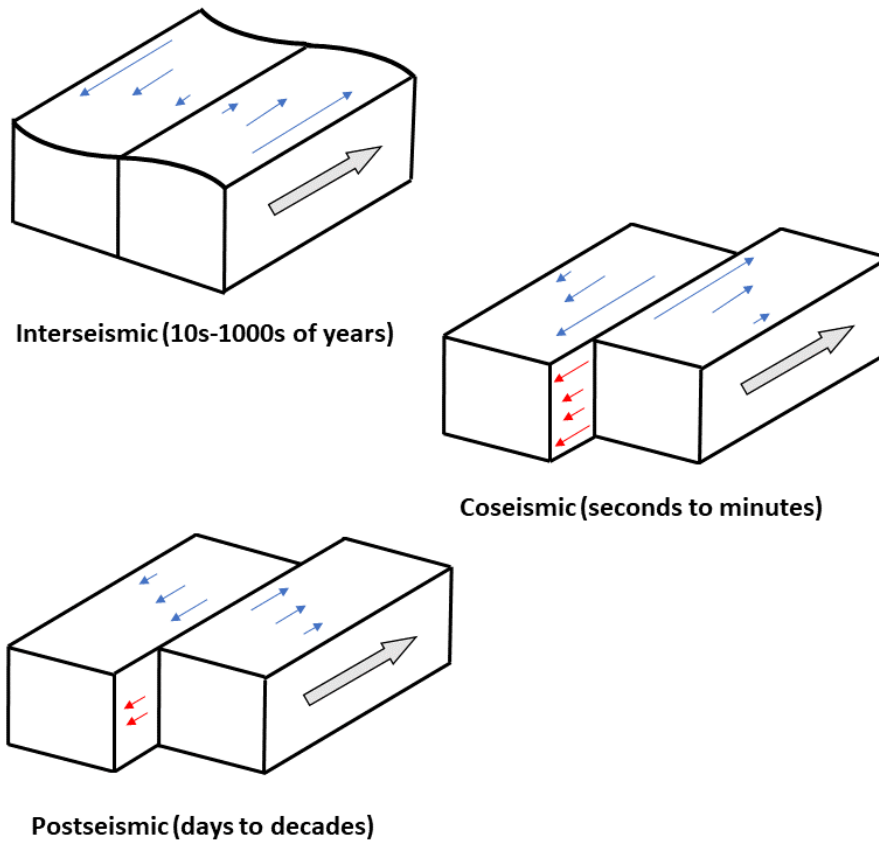


Figure 2.1: *Schematic representation of the earthquake cycle showing the three phases: interseismic, coseismic and postseismic. Grey arrows represent the long term motion of the two plates defining the fault; blue arrows represent surface displacements and red arrows the displacement on the fault surface. Postseismic slip is assumed to occur at intermediate depth, with respect to the vertical extension of the fault surface.*

Let's consider a fault, mathematically represented by a dislocation in an homogeneous medium. On the long-term, the slip on the fault is entirely due to the motion of tectonic plates (long term slip), that can be considered stationary in time. During the interseismic period, some portions of the fault are locked while others creep aseismically. To account for this behavior we define on each point of the dislocation surface a quantity called *interseismic coupling* χ_i , defined as the ratio between the slip deficit s_d during the interseismic period, which is assumed to be linearly increasing with time with a constant rate \dot{s}_d (i.e. the long term slip minus the actual interseismic slip) and the long term slip:

$$\chi_i = \frac{s_d}{s_{long-term}} = \frac{s_d}{V\Delta t} = \frac{\dot{s}_d}{V} \quad (2.7)$$

where in the second expression we write the long term slip as the product between the relative plate velocity V and the duration Δt of the interseismic phase. The fully locked portions on the fault surface will have $\chi_i = 1$ while creeping portions will have $\chi_i = 0$; in intermediate situations $0 < \chi_i < 1$.

For a shear dislocation subjected to a certain slip \mathbf{s} in an homogeneous and isotropic space, the *scalar seismic moment* M_0 is defined as the integral on the dislocation surface Σ of the slip modulus times the rigidity μ of the medium:

$$M_0 = \mu \int_{\Sigma} s(\xi_1, \xi_2) d\Sigma(\boldsymbol{\xi}) = \mu S A_{\Sigma} \quad (2.8)$$

where S is the mean slip on the fault surface and A_{Σ} is the area of the fault surface. The scalar seismic moment M_0 is a measure of the elastic energy released during the earthquake, as a proxy of the intensity of the same earthquake. It is also related to the definition of the moment magnitude M_w through the Hanks and Kanamori relation:

$$M_w = c \log_{10} M_0 - d \quad (2.9)$$

where c and d are two constants respectively equal to $2/3$ and 6 , if the seismic moment is expressed in Newton times meters (Nm).

During the interseismic period, a seismic moment deficit is accumulated on the locked portions on the fault surface meaning that slip deficit increases on these parts. The *moment build-up rate* is the time derivative of the seismic moment deficit and, as function of the slip deficit rate \dot{s}_d , and then of χ_i through equation (2.7); can be expressed as:

$$\dot{M}_0 = \mu \int_{\Sigma} \dot{s}_d(\xi_1, \xi_2) d\Sigma(\boldsymbol{\xi}) = \mu V \int_{\Sigma} \chi_i(\xi_1, \xi_2) d\Sigma(\boldsymbol{\xi}) \quad (2.10)$$

The earthquake cycle concept is expressed by saying that the moment build-up accumulated during the interseismic period must be equal, on the long term, to the moment deficit released through seismic or aseismic processes. The main idea is then that there is a certain moment *budget* that increase during the interseismic period through the (2.10) that is fully or partially released through earthquakes, depending on the importance of aseismic processes. In the next section this concept is exposed more formally and its implications on the maximum magnitude event are considered.

2.3 Gutenberg-Richter law and Moment conservation

The Gutenberg-Richter law is one of the most remarkable and ubiquitous features of worldwide seismicity (Marzocchi and Sandri 2003). It states that in a given seismic province the number N of earthquakes with magnitude greater than, or equal to, M , that occur in a given period of time, follows a relation of the form:

$$\log_{10} N = a - bM \quad (2.11)$$

where a and b are two coefficients characterizing the seismic province. Specifically, a is an expression of the seismicity activity of the considered region and b provides the information on how N scales with M . The b parameter is considered very important and has a value typically close to 1. If we intend M to be the moment magnitude M_w , we can use the Hanks and Kanamori relation (2.9) to write the magnitude as function of the seismic scalar moment M_0 ; we can then rewrite equation (2.11) as:

$$N = AM_0^{-\beta} \quad (2.12)$$

where $A = 10^{a+bd}$ and $\beta = cb$.

Actually, it is reasonable to think that the Gutenberg-Richter law couldn't hold for arbitrary size magnitudes; for a certain area, an earthquake having magnitude greater than a certain threshold M_{max} can't occur because of the finite extension of the fault surfaces (and not because it is statistically unlikely to occur). Equation (2.11) must then hold until a maximum magnitude M_{max} . Assuming a *truncated* form of the (2.11) accounting for the maximum magnitude (usually called truncated Gutenberg Richter or truncated Pareto) we can write (2.12) as:

$$N = AM_0^{-\beta} [1 - H(M_0 - M_0^{max})] \quad (2.13)$$

where H is the Heaviside function and $N(M_0)$ is the number of earthquake with seismic moment equal or larger than M_0 . The density of earthquakes n is defined as the number of earthquakes with seismic moment between M_0 and $M_0 + dM_0$ in the given period of time. It can be expressed, using the last equation, as:

$$n = -\frac{dN}{dM_0} = A\beta M_0^{-\beta-1} [1 - H(M_0 - M_0^{max})] + A(M_0)^{-\beta} \delta(M_0^{max} - M_0) \quad (2.14)$$

where δ is the Dirac delta function and the minus sign appears because $n(M_0)dM_0 = N(M_0) - N(M_0 + dM_0)$. If a given time lapse Δt is considered, assuming a constant production of earthquakes with time within the same time lapse, we can interpret N in equations (2.11), (2.12) and (2.13) as the same rate of production, that is the number of earthquakes per unit time (*frequency*) with magnitude or seismic moment equal or larger than a given threshold (as a function of the threshold) and n in equation (2.14) as density of earthquakes per unit time, provided that the coefficient a is replaced with:

$$a' = a - \log(\Delta t), \quad A' = 10^{a'+bd} \quad (2.15)$$

We state that, on the long term, a fraction α of the moment built up rate in equation (2.10) must be equal to the moment released through earthquakes while the fraction $1 - \alpha$ is released through aseismic processes. We can then write a kind of *moment conservation* equation as:

$$\alpha \dot{M}_0 = \int_0^{+\infty} M_0 n(M_0) dM_0 \quad (2.16)$$

Substituting equation (2.14) with $A = A'$ in the last equation we get:

$$\alpha \dot{M}_0 = \frac{A'}{1 - \beta} (M_0^{max})^{1-\beta} \quad (2.17)$$

Expressing A' as function of N and M_0 through

$$N = A' M_0^{-\beta} [1 - H(M_0 - M_0^{max})] \quad (2.18)$$

(we can do it assuming $M_0 \leq M_0^{max}$) we can finally write:

$$N(M_0) = (1 - \beta) \frac{\alpha \dot{M}_0}{(M_0^{max})^{1-\beta}} M_0^{-\beta} \quad (2.19)$$

This equation has the form of the Gutenberg-Richter law (equation (2.12)) but now the parameter A' is written in terms of the maximum moment and the moment build-up rate. Taking the logarithm of equation (2.12) evaluated for $M_0 = M_0^{max}$ and using the Hanks and Kanamori relation (2.9) to replace the maximum moment M_0^{max} with the maximum magnitude M_w^{max} , we obtain:

$$\log_{10} N^{max} = -\frac{M_w^{max}}{c} - \frac{d}{c} + \log_{10} \dot{M}_0 + \log_{10} \alpha(1 - \beta) \quad (2.20)$$

where N^{max} is $N(M_0^{max})$. This equation coincides with the equation 5 of Avouac 2015 once we set the c and d parameters of the Hanks and Kanamori relation respectively to $2/3$ and 6 ($\beta = cb = 2/3b$). The equation can be transformed into an expression for M_{max} using (2.11) evaluated for $M_w = M_w^{max}$:

$$M_w^{max} = \frac{1}{(1/c - b)} \left(-\frac{d}{c} + \log_{10} \alpha \dot{M}_0 + \log_{10} (1 - cb) - a' \right) \quad (2.21)$$

According to the authors this equation provides a constraint on the maximum magnitude event occurring in a given region and a given time lapse Δt that depends on the moment build-up rate, on the fraction α of transient slip that is seismic and on the b parameter of the Gutenberg Richter. Equation (2.20) is graphically represented in figure Figure 2.2 together with the Gutenberg-Richter law for different values of a .

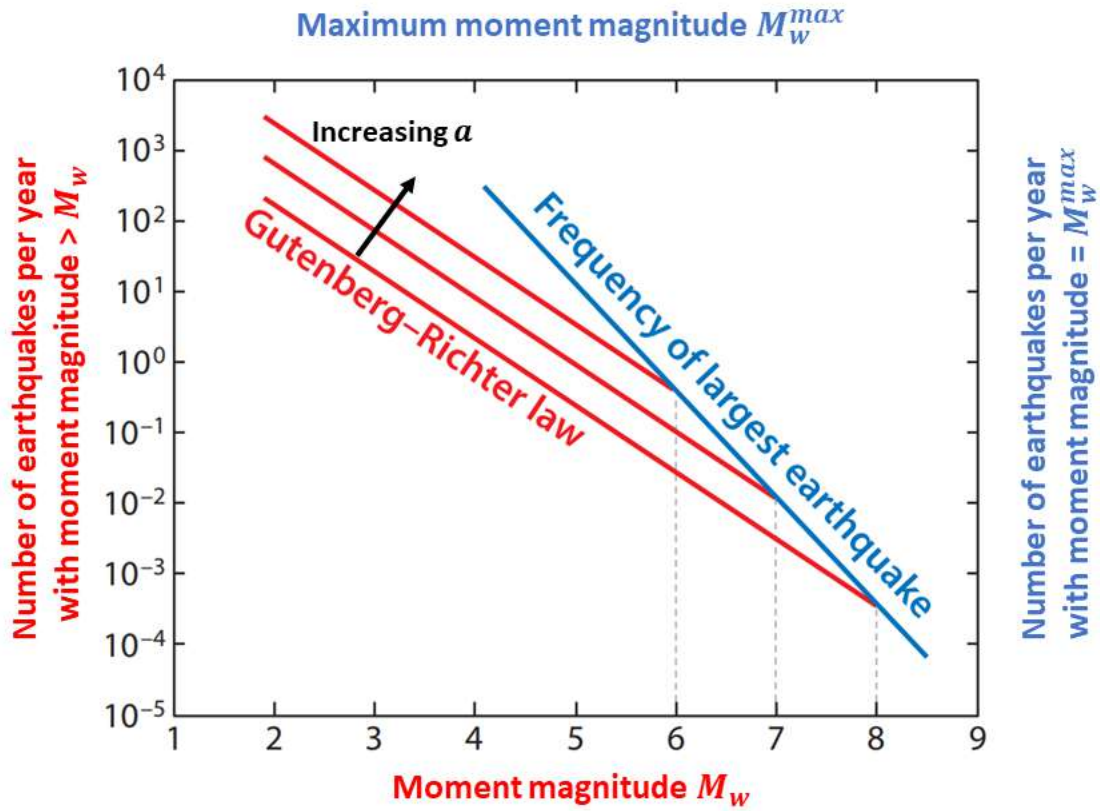


Figure 2.2: Earthquakes are assumed to obey the Gutenberg–Richter law (red lines shows the Gutenberg Richter for different values of the a parameter). The ordinate shows, on a logarithmic scale, the number of events with moment magnitude M_w equal to or larger than a given value reported along the abscissa. The frequency of the maximum magnitude event is determined assuming that the moment balance in (2.16) holds; the frequency then depends on α and β of equation (2.20). Image re-drawn from Avouac 2015

2.4 Coulomb failure model and Kostrov equation

The Coulomb failure model is the simplest way to describe the relation between stress and earthquake occurrence on a fault. Considering a single fault, Coulomb suggested that shear failure occurs when the shear stress τ acting on the fault reaches a threshold value:

$$\tau = \mu\sigma_n + c \quad (2.22)$$

where c is a cohesion coefficient, μ is the coefficient of internal friction and σ_n is the stress normal to the fault (assumed positive for compression). In presence of pore pressure p , σ_n has to be replaced with the effective normal stress, defined as $\sigma_{eff} = \sigma_n - p$. A measure of proximity to failure is the Coulomb failure stress (CFS) σ_c , defined as:

$$\sigma_c = \tau - \sigma_{eff} - c \quad (2.23)$$

Negative values of σ_c imply that the failure threshold has not yet been reached. When the failure threshold is reached or exceeded ($\sigma_c \geq 0$) the fault produces an earthquake and the shear stress on the fault drops to a lower value.

Ader et al. 2014 state that the seismicity rate \dot{N}_e is proportional to the stress rate $\dot{\tau}$. In particular, for a population of faults on which the stresses τ are uniformly distributed up to τ_f the observed seismicity rate is proportional, if the normal stress is kept constant, to the shear stress rate:

$$\dot{N}_e \propto \dot{\tau}(t) \quad (2.24)$$

Actually this relationship is true only if the stress τ has non-decreasing behaviour. If $\tau(t)$ decreases the seismicity will stop and it will resume when the stress on the fault will have increased back to a value greater than its preceding largest value (Ader et al. 2014).

The Coulomb failure is a simple model that doesn't account for the time-dependent behaviour of earthquake nucleation. More sophisticated models exist that take into account more complicated constitutive laws for a fault and can result in different relations between stress rate and seismicity. An important example is a *rate and state model* in which the friction coefficient depends on the slip and on the slip rate. In the case of a rate and state model, it is again demonstrated that the seismicity rate is proportional to the stress rate if the loading rate is constant or varies at a timescale longer than the nucleation time (Ader et al. 2014).

In general, the strain rate is not proportional to the stress rate but the relationship is given by equation (2.3). The proportionality is achieved when the trace $\dot{\epsilon}_{kk}$ of the strain rate is zero. Kostrov 1974 proposes a relationship between seismic moment tensors resulting from earthquakes nucleation in a seismogenic volume ΔV and the mean strain $\bar{\epsilon}_{ij}$ released in the volume:

$$\bar{\epsilon}_{ij} = \frac{1}{2\mu\Delta V} \sum_k M_{ij}^k \quad (2.25)$$

where μ is the rigidity of the medium and the sum is over all the seismic moment tensors inside the volume, labelled by the letter k . Ward 1994 showed that the relation (2.25) between the average crustal strain and the released seismic moment could also be used to map the moment build-up rate as a function of the average strain rate $\dot{\bar{\epsilon}}_{ij}$ of the crust during the interseismic phase. One critical assumption of Ward 1994 is that the average strain rate over the seismogenic volume ΔV could be replaced by the strain rate measured at the surface.

$$\dot{M}_{ij} = 2\mu\Delta V \dot{\epsilon}_{ij} \quad (2.26)$$

where $\dot{\epsilon}_{ij}$ is referred to be the strain rate at the surface. If we assume that no tensile dislocation can be produced then $\dot{M}_{kk} = 0$ and also $\dot{\epsilon}_{kk} = 0$. In this simple case, the proportionality between strain rate and stress rate is then expected and then, according to (2.24), a proportionality between strain rate and seismicity rate holds. This arguments are clearly subjected to numerous approximations. One of the targets of this thesis is to explore the relationship between strain rate and seismicity rate in the Apennines: first of all evaluating if a strong correlation exists and then what could be the suggested pattern.

Chapter 3

Velocity field from GPS data

3.1 GPS dataset

In this study, it is used part of the velocity data from the whole velocity dataset produced by INGV sector in Bologna, analyzing raw GPS observations from more than 4000 GPS stations operating in Euro-Mediterranean, Eurasian and African regions (Serpelloni et al. 2022). The velocity data are the result of a processing scheme consisting in 3 steps. In the first one, GPS dataset is divided into smaller sub-networks and processing is performed independently for each of them: the GAMIT module of GAMIT/GLOBK software, a suite of programs developed by MIT, is used to process phase data to estimate relative positions of ground stations and satellite orbits, atmospheric delays and Earth orientation parameters. In the second step, GLOBK software is used to realize a global reference frame by minimizing velocities of IGS (International GNSS Service) core stations, a set of high quality IGS stations used as tie-stations, and to estimate a transformation with respect to the GPS realization of the ITRF2014 frame. In the third step, displacement time series are analyzed and linear velocity estimates are determined by a least-square procedure on different parameters accounting for: linear trend, annual and semi-annual seasonal components, equipment change offsets, coseismic offsets and postseismic relaxation. White plus Flicker noise models are used to estimate uncertainties on linear velocity estimates.

The length of time series determines accuracy and precision of estimated linear velocities; in addition to semi-annual and annual signals in time series, long period noise and multi-annual loading signals also impact significantly on linear velocity estimates. It would be beneficial to have an hint on the minimum time series length required to have velocity estimates that stabilize around the values obtainable using the longest time series. Serpelloni et al. 2022 analyze a large number of GNSS stations in the Euro-Mediterranean region with a 12-year almost complete

observation history; it is shown that a minimum value for time series length in order to obtain velocity estimates consistent with the best estimated value from the whole time span is ~ 6 years for east and north velocity components. In this work, accordingly with this constraint, we consider stations with records longer than 6 years.

We consider horizontal velocity data in a region centered around Italy of latitude $36-48^\circ\text{N}$ and longitude $5-20^\circ\text{E}$ in which velocities are minimized with respect to the Tyrrhenian block (i.e. it is considered a Tyrrhenian fixed reference frame for the velocity field). The resulting field is shown in Figure 3.1. Here, the velocity estimates for GPS stations located near active volcanic areas are not accurate and not representative of the long term tectonic deformation because of the non-linear transient signals recorded in time series (caused by magma dynamics, unrest episodes and other processes). The overall field for the selected area includes a total of 1024 GPS stations including stations outside Italian boundaries. All the velocity values result from at least 6 years records, standing inside an interval between 1995 and 2021.

In the next section we will discuss filters and masks applied on data in order to obtain an input field for strain rate computations free, as much as possible, from non-coherent and non-tectonic signals.

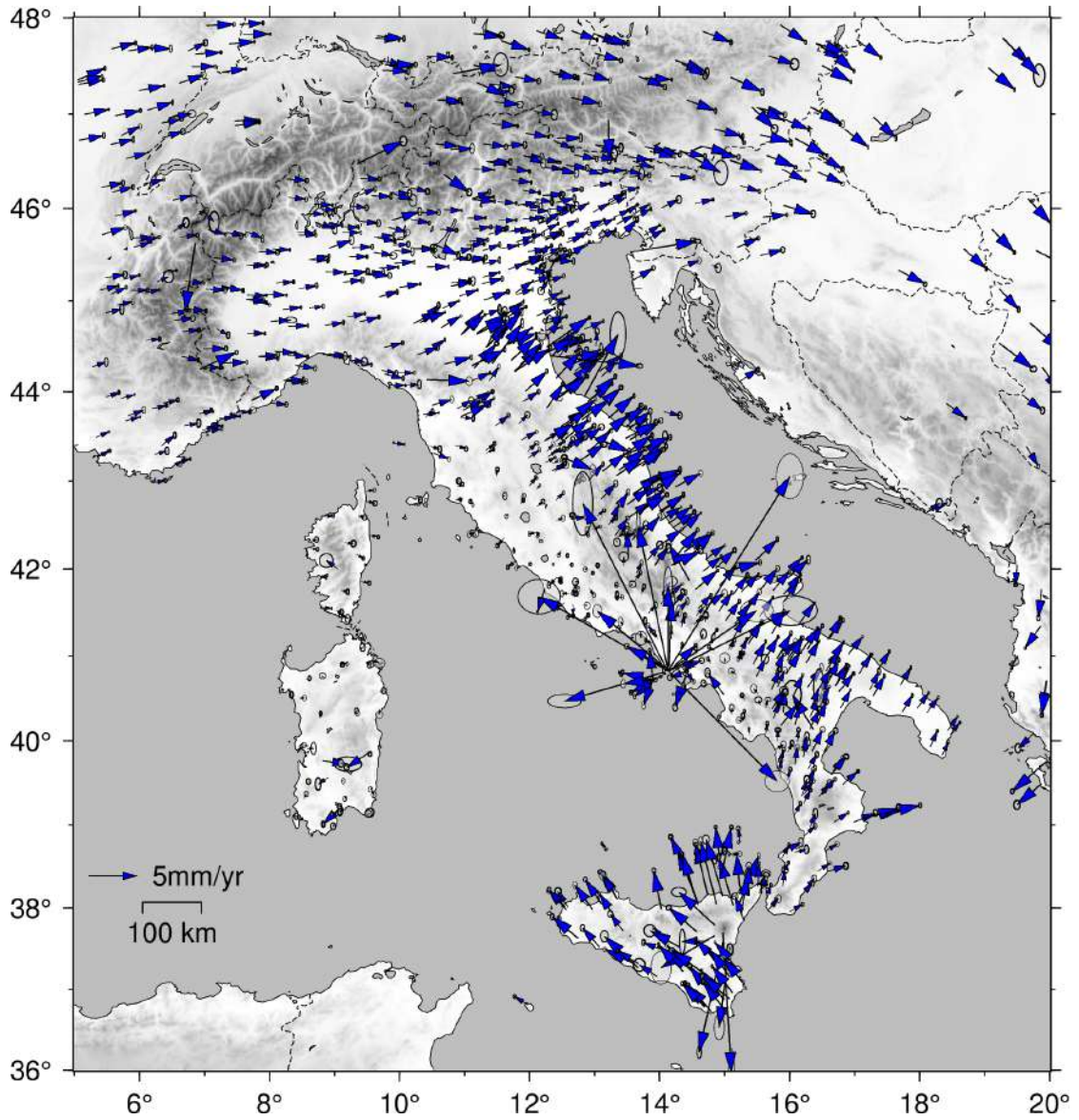


Figure 3.1: Horizontal GPS velocity field with 95% error ellipses in a Tyrrhenian fixed reference frame. The plotted dataset consists of stations with records longer than 6 years in a time-window from 1995 to 2022.

3.2 Filtering and analysis of the GPS velocity field

In this study, we are interested in spatial variations of the horizontal interseismic velocity field, caused by tectonic processes. However, the velocity field shown in Figure 3.1 is an overall field that includes signals other than tectonic (e.g. signals caused by volcanic deformation). Moreover, stations very close to each other can provide slightly different velocity values, caused by local conditions, that result in steep velocity gradients when using numerical algorithms. In order to overcome these issues, a filtering procedure on the overall field is applied through the following steps:

- Stations, whose velocities are significantly affected by volcanic deformation, are excluded from the dataset. We identify as major areas of influence three volcanic zones with active deformation: the Vesuvio and Campi Flegrei area, Ischia, the Etna volcano and the Colli Albani zone. We exclude stations inside these areas delimiting the regions with circular masks, as shown in Figure 3.2. This results in excluding 39 stations inside 4 circular masks.
- We exclude from the dataset stations in the Crotona area. The GPS velocities standing on the sea-side of Crotona are higher, in modulus, than velocities in neighbor zones and also differently oriented; at least part of these anomalies can be ascribed to the seaward motion of a megaslide in the Crotona basin (as shown in Minelli et al. 2013 and Zecchin et al. 2018). We remove from the dataset 4 stations in this area.
- There are several stations installed on offshore platforms in the northern Adriatic sea, whose time series are influenced by on-site gas extraction activity. Therefore, a total of 18 stations, with poor quality time series leading to not reliable linear velocity estimates, are removed.
- In order to identify inconsistent velocities in the dataset, we use the wavelets method to find out outliers in the field (see section 4.3 for a description of the method). Indeed, we find that the wavelets method is more robust to outliers than the other adopted methods to compute the strain rate. We apply the wavelets algorithm with a resolution parameter $q_{max} = 8$ on the overall velocity field in Figure 3.1. We find that residuals on East and North velocity components are roughly gaussian and not linear correlated; we then decide to exclude from the dataset stations, standing out of an ellipse having semi-axes equal to 4 times the standard deviation for residuals respectively on East and North component (Figure 3.3).

- There are stations that are very close to each other (few meters); this can lead to bad estimates of strain rate, due to difference in stations velocities on small distances. We decide, on the basis of distances distribution from each station to its neighbor, to apply a weighted mean for velocity of stations closer than 100 m, using as weights the uncertainties on the GPS velocities (Figure 3.4).

The resulting velocity field, after these steps, is shown in Figure 3.5 and contains 899 stations.

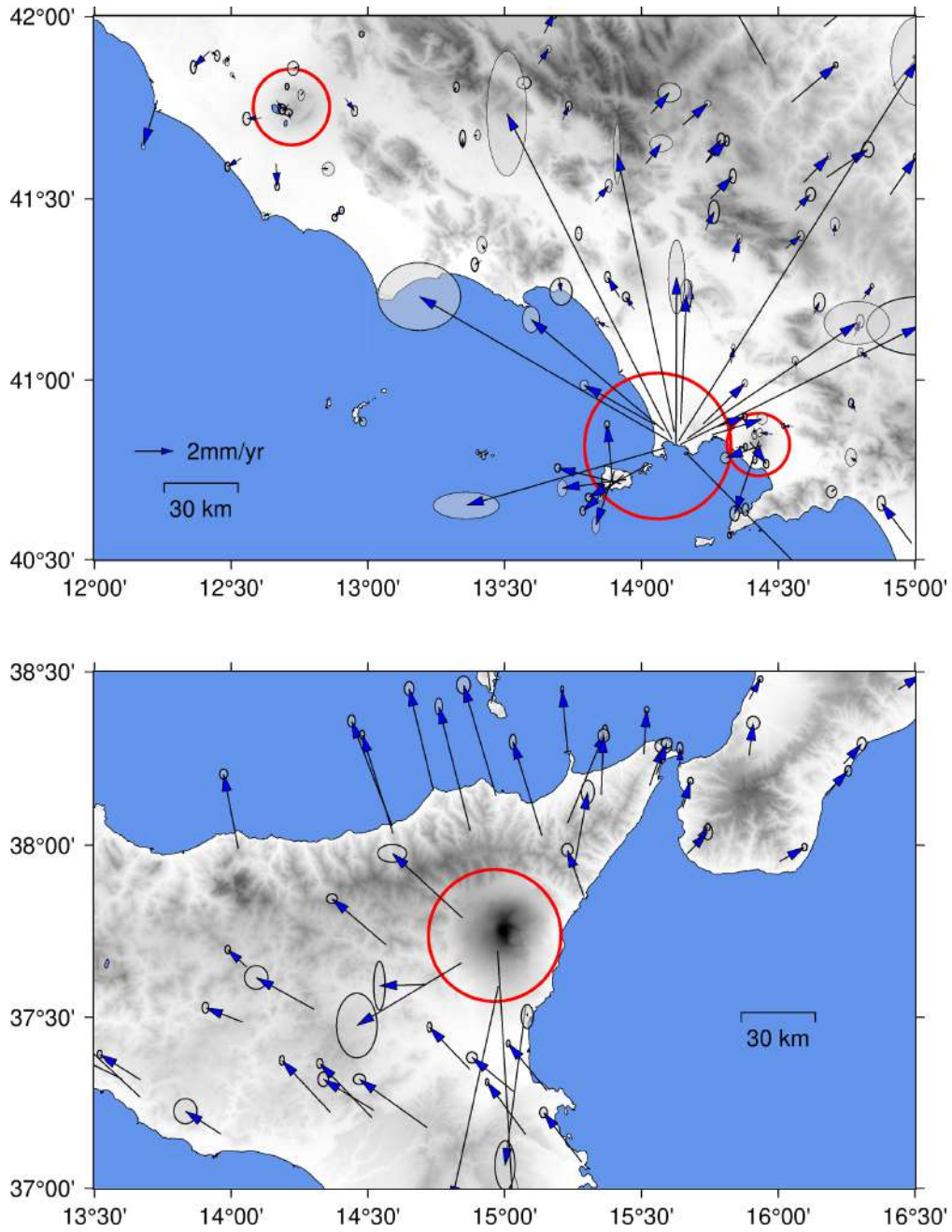


Figure 3.2: *Circular masks for volcanic areas (red circles) and GPS velocities (blue arrows). Top: Colli Albani, Ischia, Campi Flegrei and Vesuvio masks. Bottom: Etna mask.*

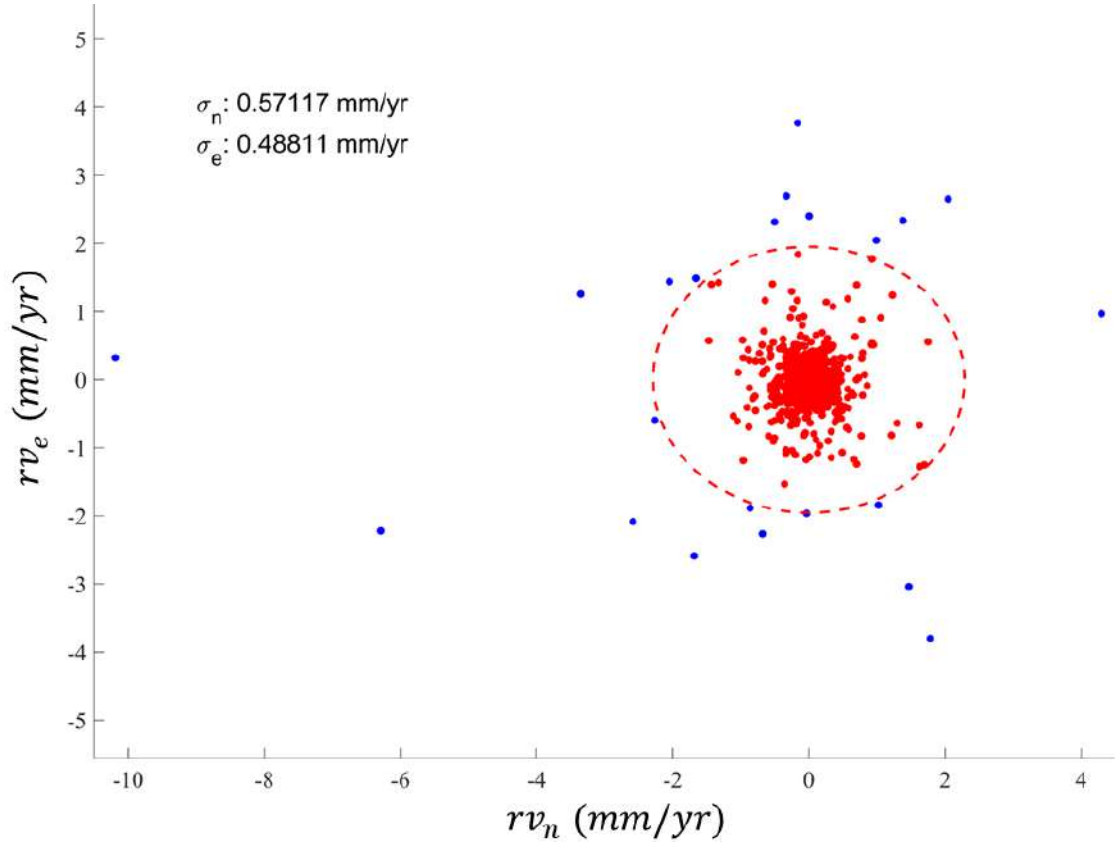


Figure 3.3: *Plot of residuals after wavelets algorithm with $q_{max} = 8$. On the x-axis: residual velocity rv_n for the north velocity component (mm/yr); on the y-axis: residual velocity rv_e for the east component (mm/yr). Red points represent kept stations: they stand inside an ellipse with horizontal semi-axis of 2.29 mm/yr (4 times the standard deviation σ_n for the north component) and vertical semi-axis of 1.95 mm/yr (4 times the standard deviation σ_n for the east component). Blue points represent stations excluded from the dataset.*

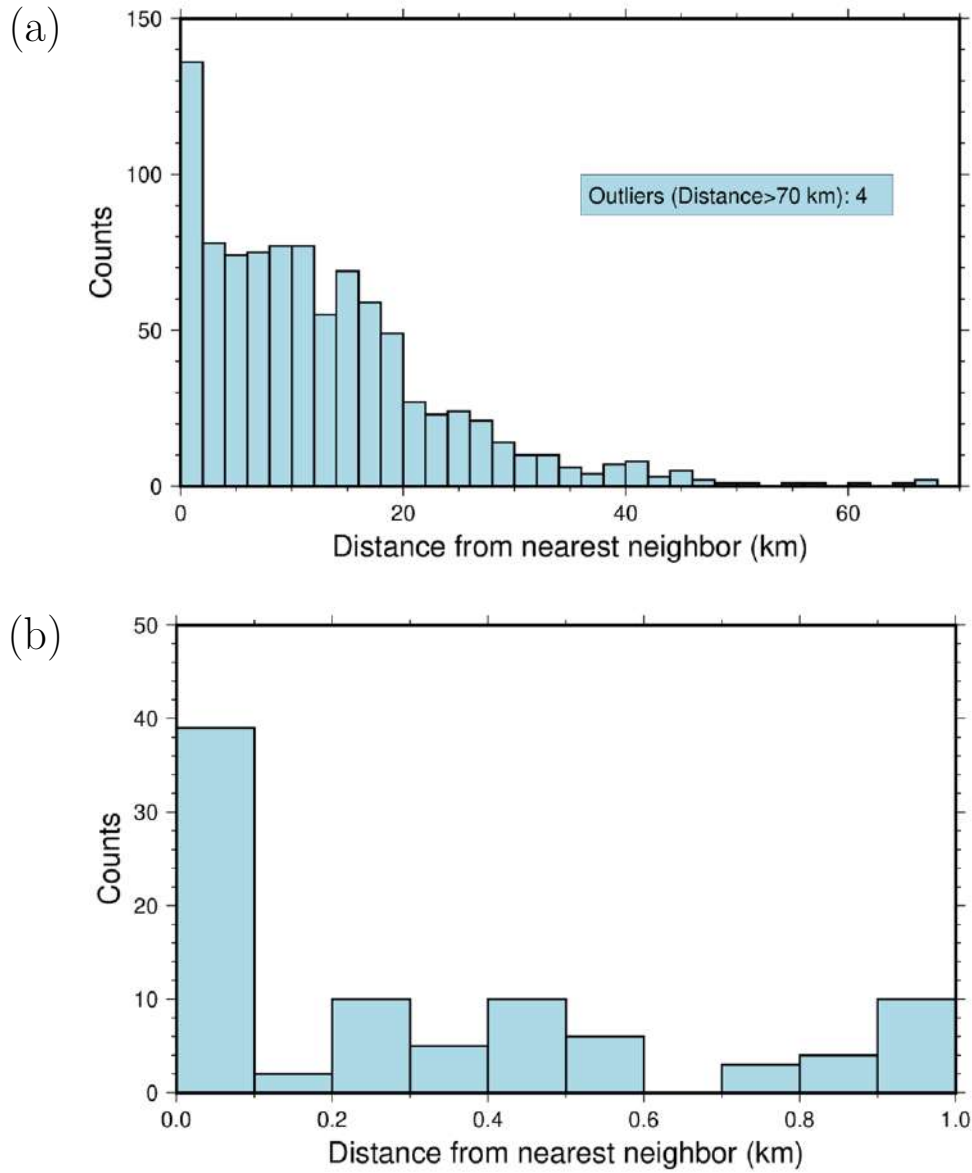


Figure 3.4: a) Histogram of distances of the nearest neighbor for stations b) Detail of the histogram (a) for distances less than 1 km.

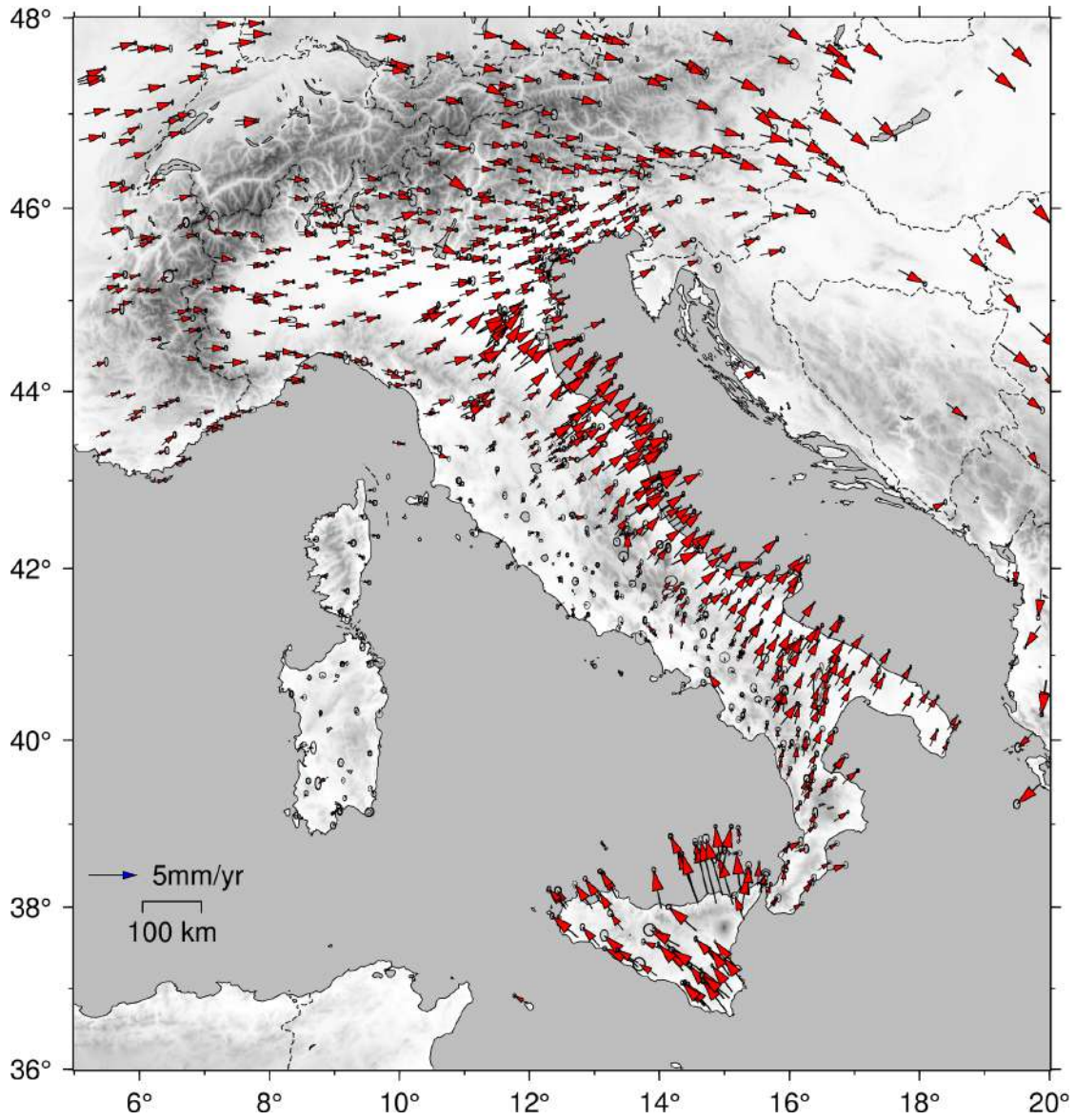


Figure 3.5: Horizontal GPS velocity field with 95% error ellipses filtered following the procedure described in this section. The field includes 899 stations.

Chapter 4

Computation of geodetic strain rate

Different methods to estimate the strain rate field from geodetic data can lead to considerably different strain rate maps (Sandwel 2010). These differences are due to the limited spatial resolution of GPS array and to different parametrizations implemented in methods. Some of them are based on a physical description of the system, e.g. elastic block models found on elastic deformation theory for faults in an half space (McCaffrey 2002), while others don't consider any particular physical model. In this study the focus is on the latter type of methods, considering three different ways to estimate strain rate from horizontal GPS velocity field. Differences between strain rate maps will be discussed and one model among the others will be chosen for the further analysis. The different methods (when applied to the GPS dataset shown in Figure 3.5) are presented in order of increasing complexity, together with their results, in the next three sections; the discussion of the deformation rate field provided by the chosen model is instead presented in the last section of this chapter.

4.1 The nearest neighbors algorithm

The first considered method is the nearest neighbors algorithm of Handwerker et al. 2018 that is employed through the Python library *Strain_2D* (Materna, Maurer, and Sandoe 2021). The algorithm works using two parameters that are:

- The radius R in km that defines a circle around each point of the spatial grid, used for the strain rate computation
- The number N of stations that are considered inside the circle

For each grid point, the nearest N stations inside a circle of radius R are considered and their GPS velocities are used to provide a numerical estimate of velocity and velocity gradients in that point (if there are no N stations inside a circle with radius R , the velocity gradients are set to zero). The strain rate can then be computed from the knowledge of the velocity field gradients through equation (2.4).

The algorithm is applied to our dataset making different trials in which we set $R = 200$ km and we vary N , using it as a smoothing parameter. Trying $N = 10, 20, 30, 40$, the results are shown in Figure 4.2 for the second invariant of the strain rate. Increasing the value of N results in maps with values of strain rate more distributed in space and an overall decreasing of the mean value for the second invariant I_2 ; instead, decreasing the value of N results in maps with more spatially localized deformation rate and an increasing of the mean value of I_2 . An appropriate value for N depends on the level of resolution that we desire; however, an increase of N results also in increasing the noise level of the map, i.e. spatial-localized deformation rate due to small, but highly localized variations in velocity field. A method to choose an appropriate value for N can be based on the improvement in fitting GPS velocities when the value for N decreases.

The *Root Mean Squared Error (RMSE)* provides an estimate of the agreement between data and model. In this case, data are the observed velocities at the N_s GPS stations in the two components: North $v_{N_i}^{obs}$ and East $v_{E_i}^{obs}$ for $i = 1, \dots, N_s$. Indicating with $v_{N_i}^{mod}$ and $v_{E_i}^{mod}$ the modeled velocities at the positions of the N_s stations we can write the RMSE as:

$$RMSE = \sqrt{\frac{\sum_1^{N_s} (v_{N_i}^{obs} - v_{N_i}^{mod})^2 + (v_{E_i}^{obs} - v_{E_i}^{mod})^2}{2N_s}} \quad (4.1)$$

In Figure 4.1 we plot the RMSE as function of N . We can see that there is a bigger improvement in RMSE when passing from $N = 35$ to $N = 30$. This suggests that a good compromise in choosing an appropriate map can be the one with $N = 30$, shown in Figure 4.2c.

In Figure 4.3 the dilatation rate field is shown for the case $N = 30$. For this map, the same reasoning made for the second invariant field holds: greater values of N result in a smoother map for dilatation rate, while smaller values of N imply less smoothed distribution of dilatation rate. The comparison between data and models is shown in Figure 4.4, together with the residual velocity map (residuals are computed as "observed velocities" - "modeled velocities"). The model with $N = 30$ produces a general good agreement between modeled and observed velocities and the 92 % of residuals is smaller than 1 mm/yr.

The main advantage of the method of Handwerger et al. 2018 is that it relies on few parameters that have to be set. On the other hand, it presents some

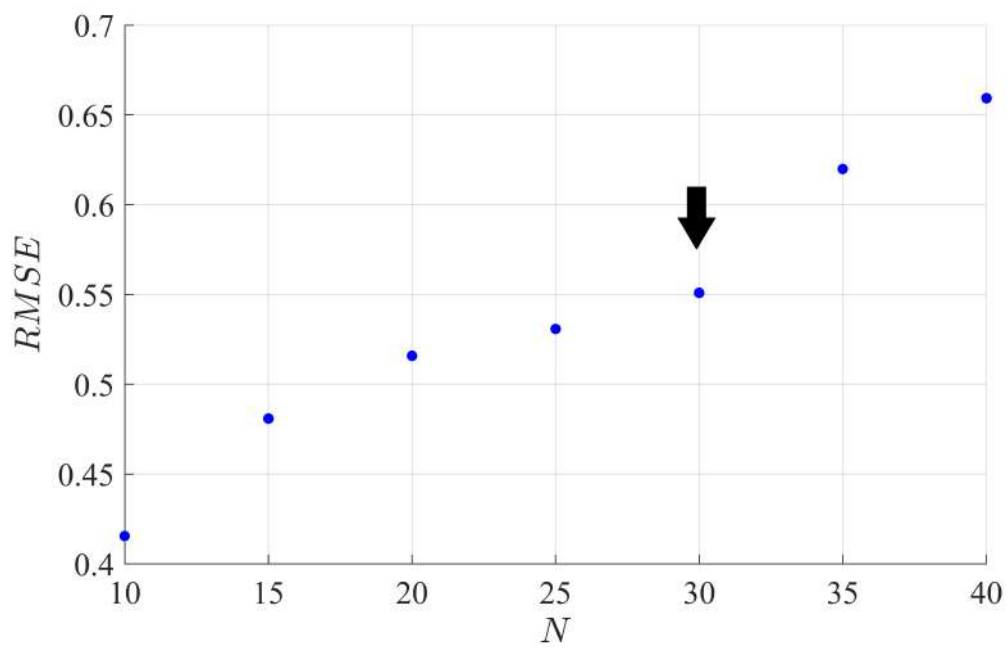


Figure 4.1: *RMSE computed for different values of N (blue points). The arrow shows the point for which a bigger improvement in RMSE happens (passing from $N = 35$ to $N = 30$).*

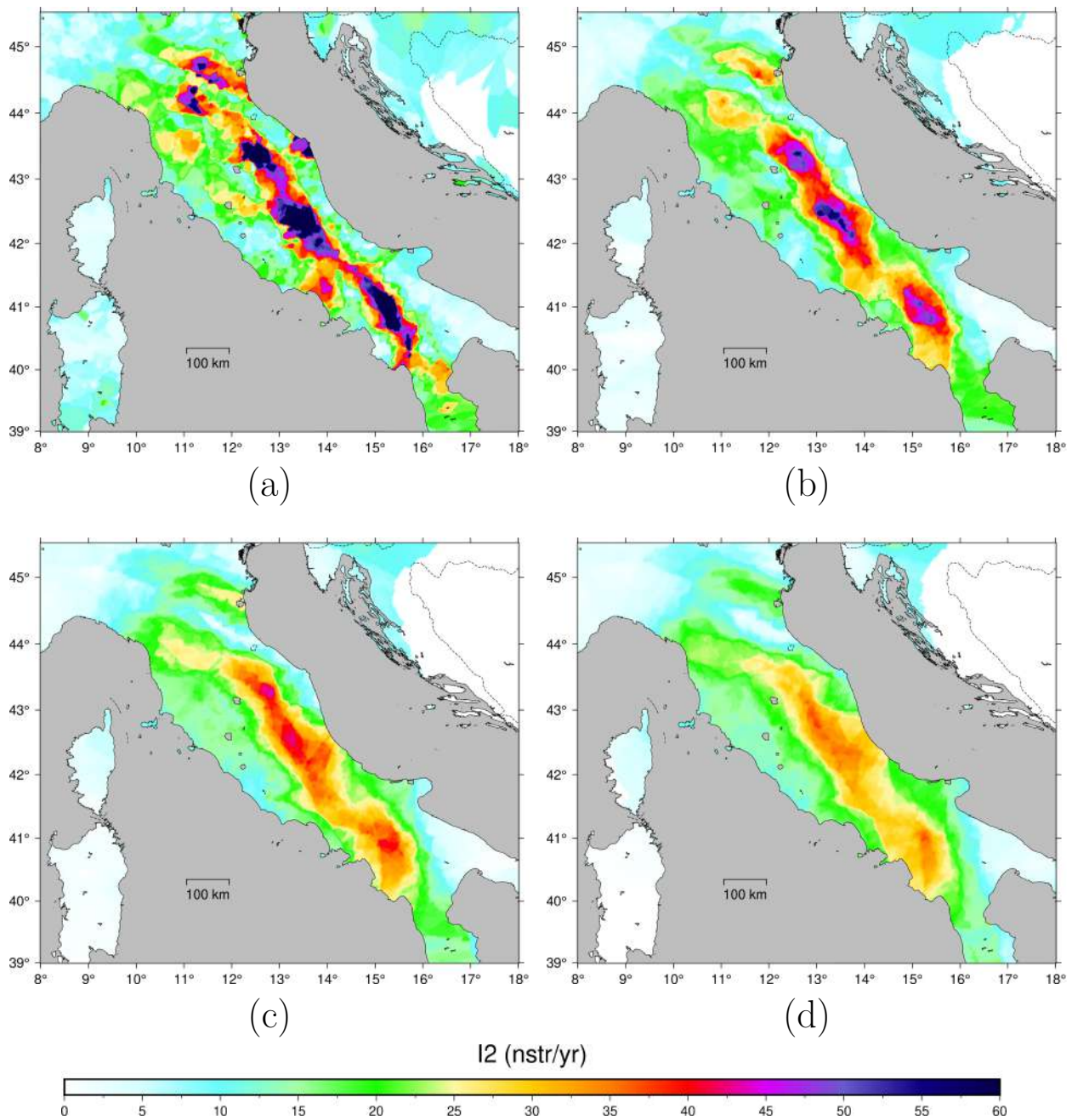


Figure 4.2: *Second invariant of the strain rate computed from the filtered GPS dataset through the nearest neighbors algorithm considering: a) $N = 10$, b) $N = 20$, c) $N = 30$, d) $N = 40$.*

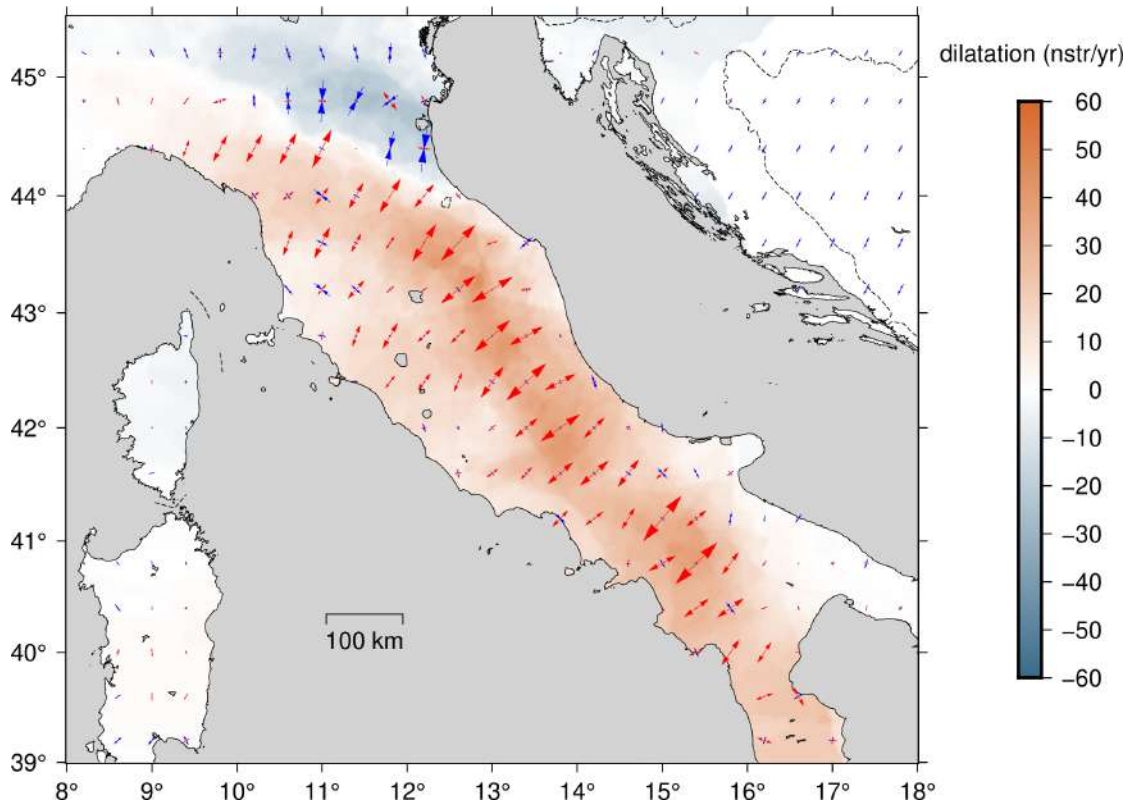


Figure 4.3: *Dilatation rate and principal axes of strain rate for the nearest neighbor method applied to the filtered dataset in the case with $N = 30$.*

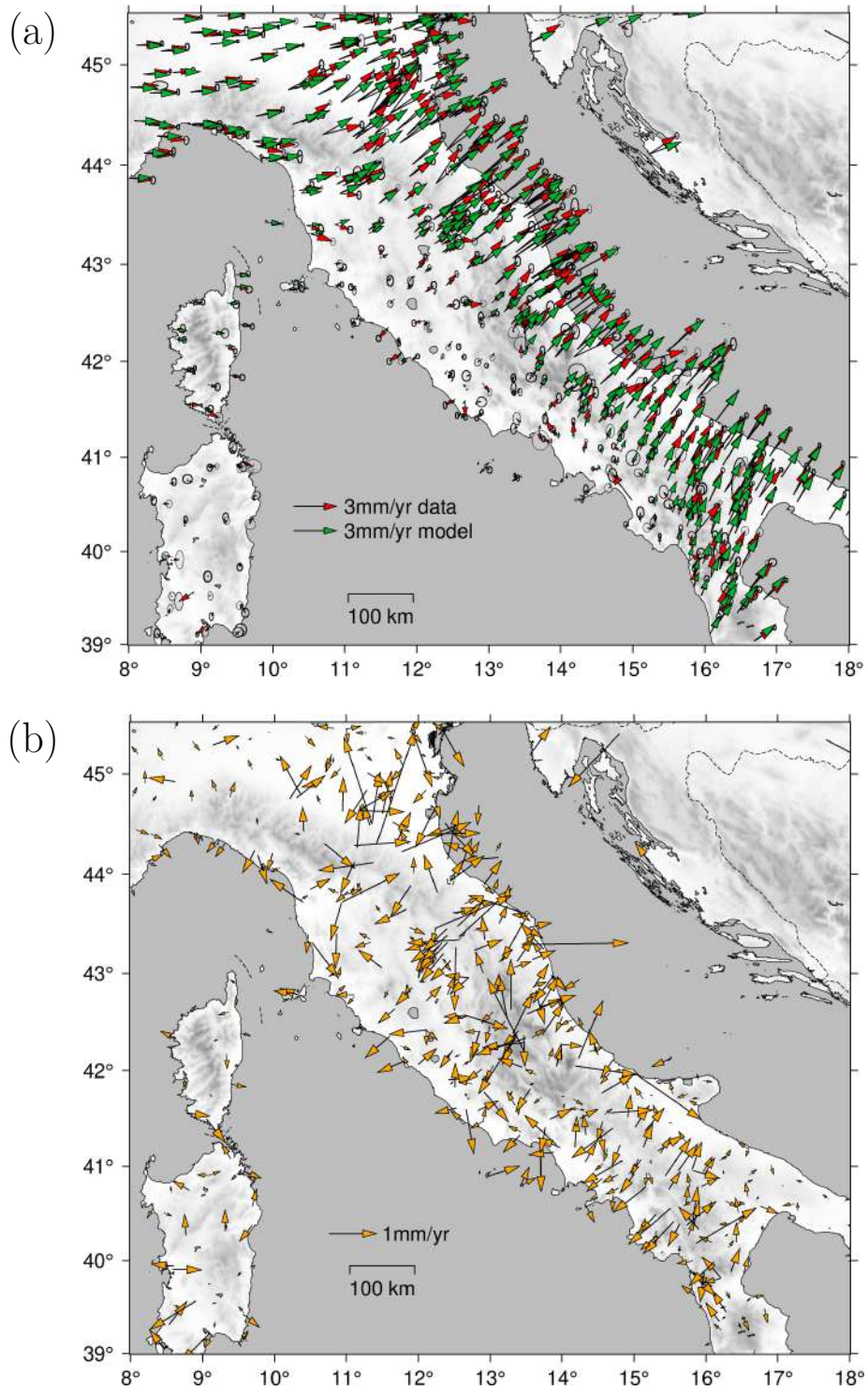


Figure 4.4: *a) Plot of the modeled velocity field from the nearest neighbors method with $N = 30$ (green arrows) against the GPS velocity dataset (red arrows). b) Residuals resulting as "observed velocities" - "modeled velocities" (orange arrows).*

drawbacks; the first is that it doesn't account for the different density in GPS station positions, but applies the same procedure for strain rate computation at each grid point. The only parameter that takes into account the different coverage is R , but it is a switch: if there are not N stations inside a circle with radius R , the velocity gradients are set to zero. The second drawback is that, regardless of the value of N , the resulting maps have region with uniform strain rate due to the geometry of the GPS network. This then results in homogeneous values of strain rate even on distances of several kilometers. The methods described in the following paragraphs overcome, at least partially, these drawbacks.

4.2 The VISR algorithm

The VISR algorithm of Shen et al. 2015 is the second method considered in this thesis. In order to understand how it works, let's start considering a small GPS array. We approximate the observed motion of the small array by an average strain rate within the array plus a rigid block motion of the array as a whole. This holds:

$$v_x = U_x + \dot{\epsilon}_{xx}\Delta x + \dot{\epsilon}_{xy}\Delta y + \omega\Delta y \quad (4.2a)$$

$$v_y = U_y + \dot{\epsilon}_{xy}\Delta x + \dot{\epsilon}_{yy}\Delta y - \omega\Delta x \quad (4.2b)$$

where v_x and v_y are the observed velocities at the array points, U_x and U_y are the velocities at the center of the array, Δx and Δy are the distances of the point from the center and ω is the angular velocity. The same reasoning can be applied for a bigger array: in any location \mathbf{x} , we consider a small array around \mathbf{x} for which we can apply the equations (4.2); given N stations distributed around \mathbf{x} , the vector \mathbf{v} of GPS velocity data collected from the N stations can be written, in a matrix form, as $\mathbf{v} = \mathbf{A}\mathbf{m} + \mathbf{n}$:

$$\mathbf{v} = \begin{bmatrix} v_{x_1} \\ v_{y_1} \\ v_{x_2} \\ v_{y_2} \\ \dots \\ v_{x_N} \\ v_{y_N} \end{bmatrix} = \begin{bmatrix} 1 & 0 & \Delta y_1 & \Delta x_1 & \Delta y_1 & 0 \\ 0 & 1 & -\Delta x_1 & 0 & \Delta x_1 & \Delta y_1 \\ 1 & 0 & \Delta y_2 & \Delta x_2 & \Delta y_2 & 0 \\ 0 & 1 & -\Delta x_2 & 0 & \Delta x_2 & \Delta y_2 \\ \dots & \dots & \dots & \dots & \dots & \dots \\ 1 & 0 & \Delta y_N & \Delta x_N & \Delta y_N & 0 \\ 0 & 1 & -\Delta x_N & 0 & \Delta x_N & \Delta y_N \end{bmatrix} \begin{bmatrix} U_x \\ U_y \\ \omega \\ \dot{\epsilon}_{xx} \\ \dot{\epsilon}_{xy} \\ \dot{\epsilon}_{yy} \end{bmatrix} + \begin{bmatrix} n_{x_1} \\ n_{y_1} \\ n_{x_2} \\ n_{y_2} \\ \dots \\ n_{x_N} \\ n_{y_N} \end{bmatrix} \quad (4.3)$$

Where \mathbf{n} is the vector of the uncertainties. Given the direct problem stated by (4.3) and if the uncertainties follow a normal distribution centered on zero, a least

square solution can be found as:

$$\mathbf{m} = (A^T C^{-1} A)^{-1} A^T C^{-1} \mathbf{v} \quad (4.4)$$

where C is the covariance matrix of the GPS velocity data. The solution (4.4) provides us the *mean* strain rate field for the region around \mathbf{x} . The same reasoning applied for a number of grid points \mathbf{x}_j $j = 1, \dots, M$, at which we assign the found values of strain rate, can supply an estimate of the non-homogeneous strain rate field inside the array. The problem is how to select and weight observations standing around each grid point. The covariance matrix is reconstructed by multiplying a weighting function to each diagonal term. The weighting function W_i for the i -th diagonal term and referred to the i -th station is defined as the product of two functions: $W_i = L_i Z_i$ (without sum on equal indices) where L_i is a *distance* dependent function and Z_i a *coverage* dependent function.

The L_i function weight the station contribution, basing on the distance between the station and the grid point; it takes two possible forms:

$$L_i = \exp(-\Delta R_i^2/D^2) \quad (4.5a)$$

or

$$L_i = 1/(1 + \Delta R_i^2/D^2) \quad (4.5b)$$

in which a spatial smoothing parameter D is introduced and ΔR_i is the distance of the i -th station from the grid point. The main difference between the two forms is that the Gaussian form (4.5a) reduces the weight at an higher rate with the distance ΔR_i than that of the quadratic form (4.5b). The quadratic form is then more conservative and provides a smoother solution. The smoothing parameter D is determined for each grid point in the following way: it is fixed an a-priori *weighting threshold* w_t before the algorithm starts and D is obtained posing the quantity $w = \sum_i W_i$ (the sum of the weighting functions) equal to w_t . In this way a uniform level of weighting w_t is chosen for the total array, while D is determined for each grid point, depending on the local data density: denser the array, smaller will be D . Once one of the two forms in (4.5) is chosen, the algorithm considers n data-points having L_i such that $\Delta R_i/D < c_d$ where c_d is a cutoff distance. The cutoff distance is set to 2.15 for (4.5a) and to 10 for (4.5b); in this way stations with $L_i < 0.01$ are excluded.

The coverage weighting function Z_i weights on the base of the angular distribution of the stations around the grid point. It is defined in two possible ways:

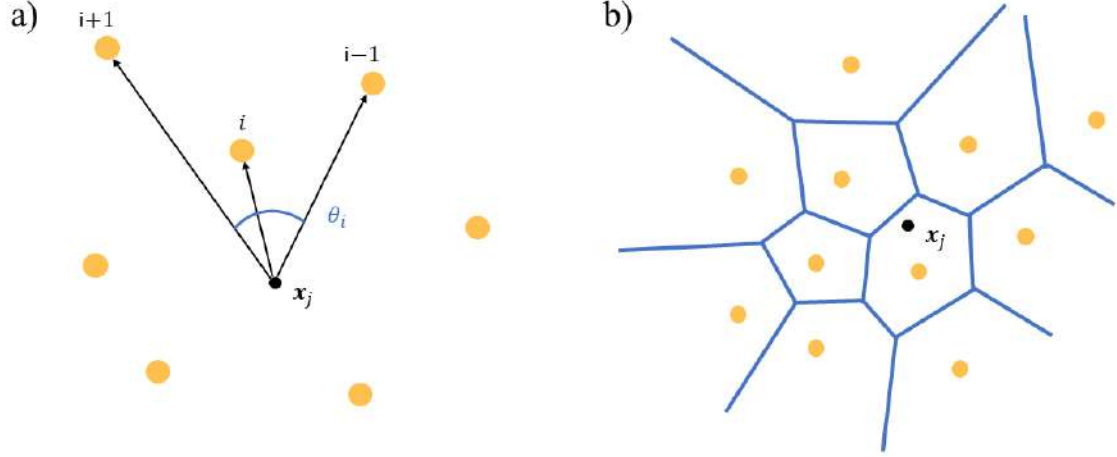


Figure 4.5: a) The azimuth angle θ_i relative to the i -th station for the grid point \mathbf{x}_j ; stations are indicated with yellow points and ordered counter-clockwise. b) Voronoi cells for a set of stations (yellow points) around the grid point \mathbf{x}_j . The Voronoi cells are a partition of a plane and each cell contains points closer to the station inside the cell than to any other station

$$Z_i = n\theta_i/4\pi \quad (4.6a)$$

or

$$Z_i = nS_i / \sum_{k=1}^n S_k \quad (4.6b)$$

In the first form (4.6a) (azimuthal weighting function), n is the total number of data points selected and θ_i is the angle between the station $i+1$ and $i-1$ once they are ordered counter-clockwise around the grid point (Figure 4.5a). In this way, stations isolated in space with respect to the grid point have a greater Z_i . The same rationale is applied for the second form (4.6b) in which S_i is the area of the Voronoi cell for the i -th station; in this case, the weight is given by the ratio between the area of the cell relative to the station i and the total area of all the cells around the grid point (Figure 4.5b). Comparing the two forms in (4.6), the first considers only the azimuthal coverage while the second is based also on the radial coverage for the grid point.

We start applying the VISR method to our dataset, considering the Gaussian form for the distance weighting function (4.5a) and the Voronoi form (4.6b) for the coverage weighting function. Four values for the weighting threshold w_t : 8,

16, 24, 38 are considered and the second invariant of the strain rate is computed according to (2.6b); the results are shown in Figure 4.6.

As w_t increases also the smoothing distances D increase and the strain rate becomes smoother; the regions with greater density of stations gain more resolution when w_t decreases. Following the approach in Shen et al. 2015, we search an optimal weighting threshold w_t , examining differential strain rate patterns from two strain rate field, obtained using a different w_t . In Figure 4.7, we show the three differential strain rate field obtained from the subtraction of the fields in Figure 4.6; in terms of weighting threshold, we consider: 16 – 8, 24 – 16 and 38 – 24. The differential strain rate field in Figure 4.7c (38 – 24) is smooth and diffuse along all the Apennines chain; observing Figure 4.7b (24 – 16) the differential strain rate present some spotted areas in comparison with Figure 4.7c but almost preserving the same pattern. In Figure 4.7a the pattern changes: even if strain rate is accumulated along the Apennines, now there are spikes of strain rate in localized area of few kilometers. These spikes don't represent an increase in resolution due to additional tectonic strain, but noise due to very localized heterogeneity of the velocity field. To choose a preferred model a trade-off between resolution and robustness is necessary; in this case, for a weighting threshold of 16, the improvement in resolution upon its point has only a small increasing in noise level, while, for a weighting threshold of 8, a major resolution is accompanied by an important increase of localized spots. A good compromise between resolution and noise is reached for a w_t of 16; the comparison between modeled and observed velocity and the residual map is shown in Figure 4.8. However, different choices of w_t can be made, according to the level of resolution required. The drawback is that an increase in resolution, after a certain level of w_t , can produce also a large amount of very localized spots of higher strain rate.

The comparison between observed and modeled velocity, together with the resulting residual map ("observed velocities" - "modeled velocities"), is shown in Figure 4.8. There is an overall good agreement between observed and modeled velocities with small residuals that don't show a preferential direction.

The data density reflects the level of resolution that can be obtained. In the VISR algorithm, this information is codified by the parameter D that is set on the basis of the local data strength. Figure 4.9 shows the distribution of the D values used to compute the velocity field in the case of the Gaussian + Voronoi weighting with $w_t = 16$. D clearly reflects the local data density and has the smaller values, where stations are close to each other; here the detail level of the strain rate map can be increased, choosing a smaller w_t .

Changing the coverage weighting function and using the relation (4.6a) with the weighting threshold of 16, provides a pattern comparable to the one shown in Figure 4.6b (that also have $w_t = 16$). The main differences are that the over-

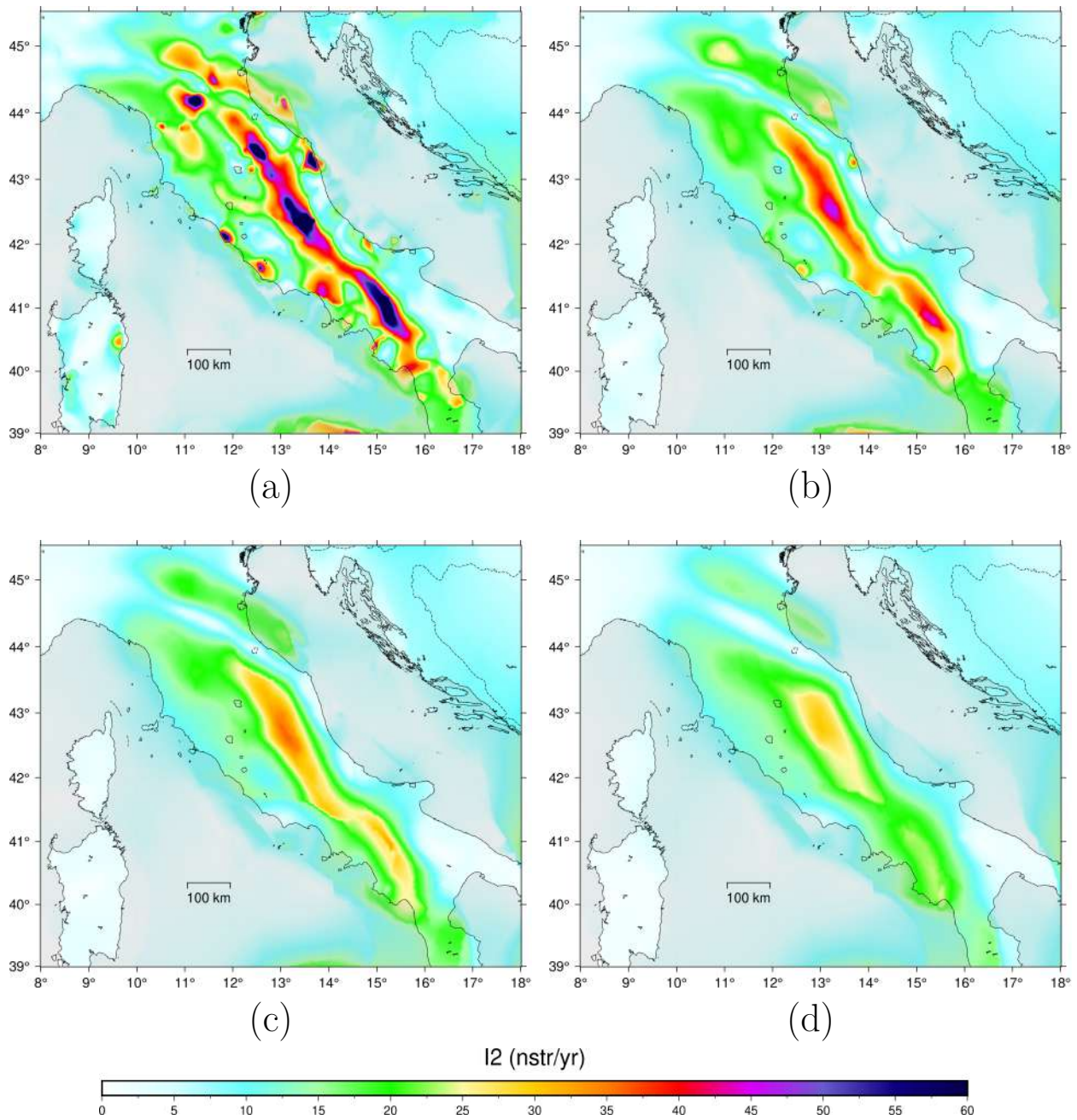


Figure 4.6: *Second invariant of the strain rate computed from the filtered GPS dataset through the VISR method with Gaussian+Voronoi weight and considering different weighting thresholds w_t : a) $w_t = 8$, b) $w_t = 16$, c) $w_t = 24$, d) $w_t = 38$.*

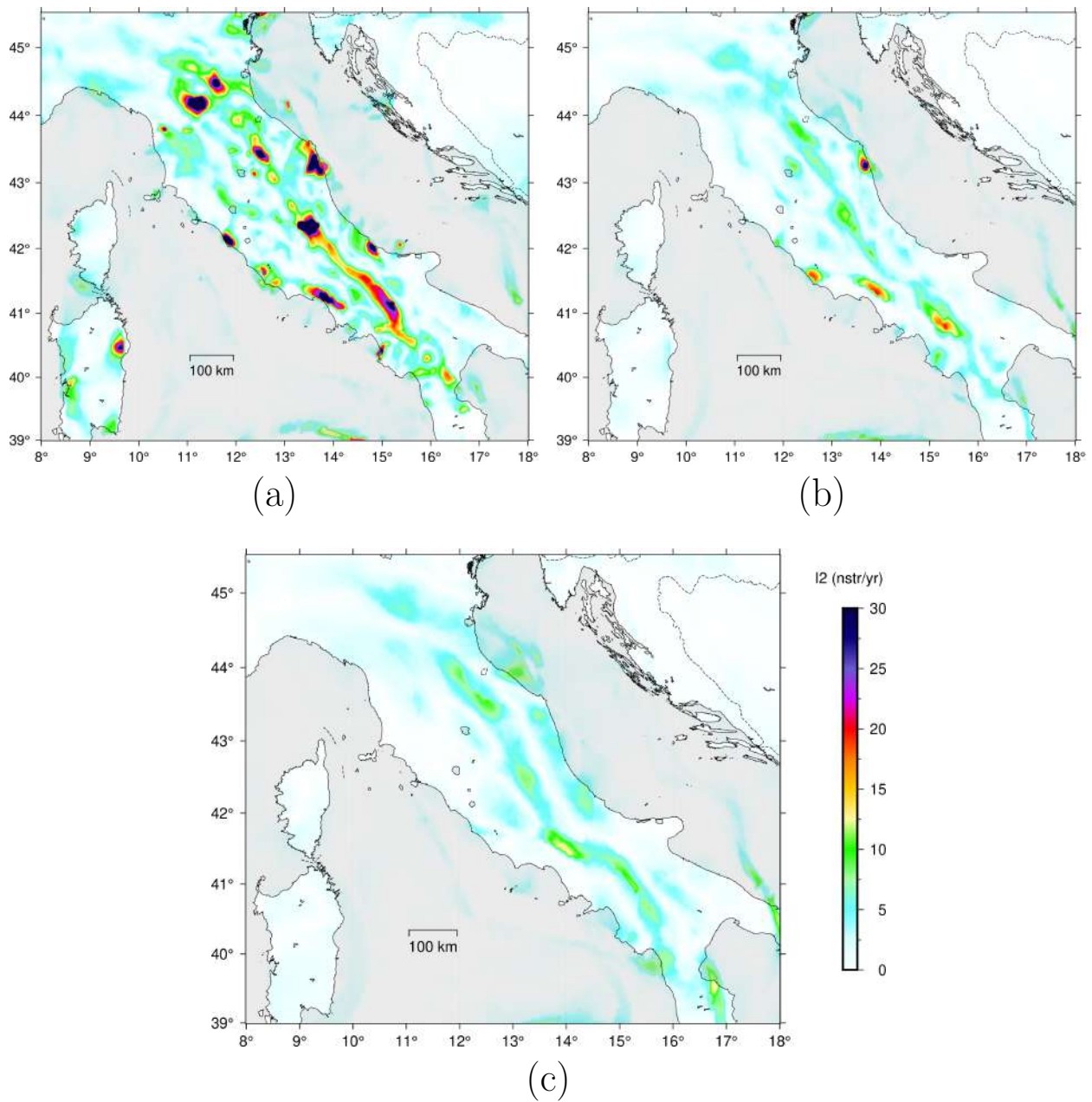


Figure 4.7: *Differential second invariant of the strain rate computed from the filtered GPS dataset through VISR method, in the case of Gaussian distance weighting and Voronoi coverage weighting, considering the differential maps. In terms of w_t : a) 16 – 8, b) 24 – 16, c) 38 – 24.*

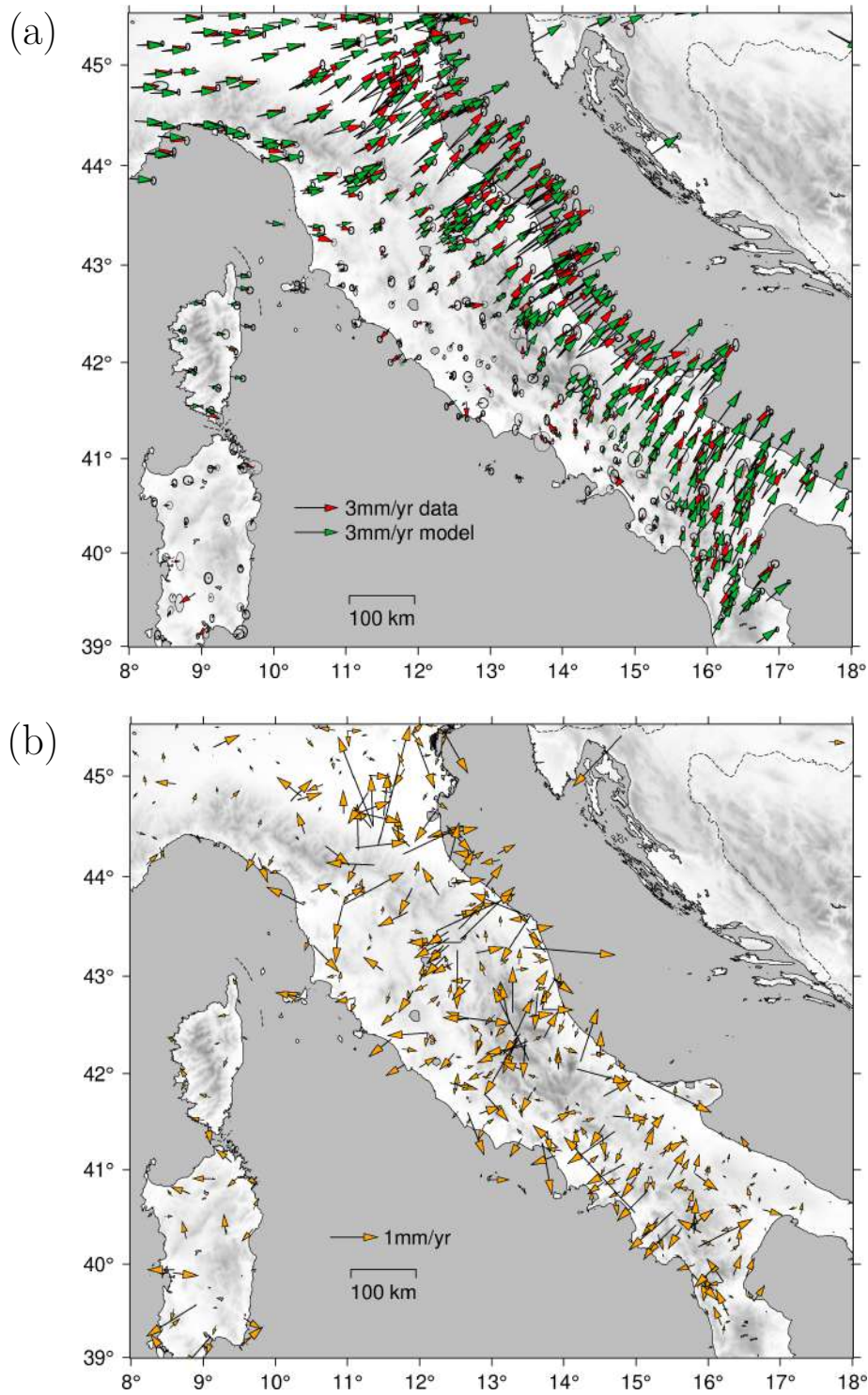


Figure 4.8: *a) Plot of the modeled velocity field from the VISR method for the Gaussian + Voronoi weighting with $w_t = 16$ (green arrows) against the GPS velocity dataset (red arrows). b) Residuals from the inversion (orange arrows).*

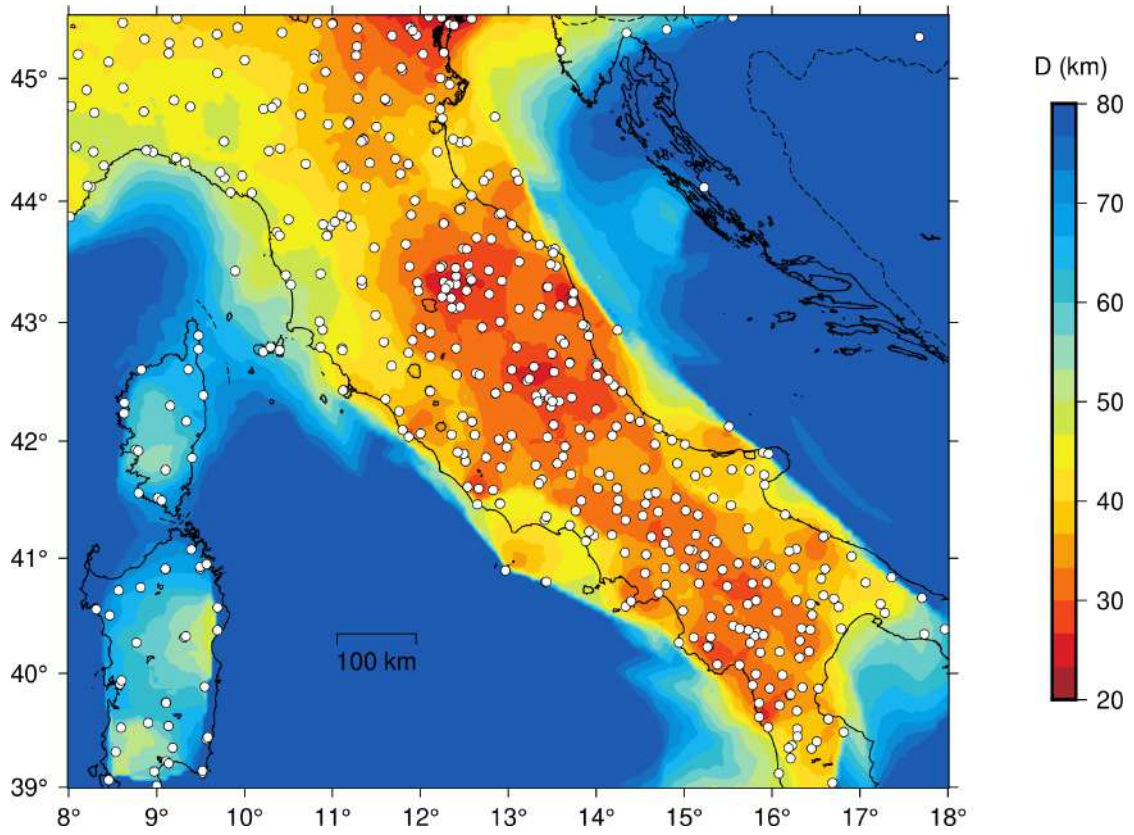


Figure 4.9: Values of the D parameters for VISR method based on the GPS station distribution. White circles represent GPS stations. The density of the geodetic points controls the selection of D .

all pattern is less smoothed and that areas with higher deformation rate on the Apennine chain are highlighted (Figure 4.10a). Instead, using the quadratic function (4.5b), but maintaining the Voronoi coverage weighting function, provides the same level of sharpness of the strain rate pattern of Figure 4.6b (with $w_t = 16$) at smaller weighting threshold. In particular, a similar result is reached at $w_t = 4$ (Figure 4.10b). The pattern is again similar, but not as smooth as the Gaussian + Voronoi case and seems very affected by local gradients in velocity field (that results in spots of higher deformation rate in the I_2 map); even if the quadratic form reduces the weight at a higher rate with the distance, the small w_t probably gives in some cases too much weight to the stations closest to each grid point. The same problem is enhanced using the azimuthal coverage weighting (Figure 4.10c); the map presents many localized spots with high strain rate. Using smaller values of w_t , the problems of localized spots disappears, but with values of I_2 smoothly distributed.

To conclude, the VISR algorithm overcomes some drawbacks of the nearest neighbor method, analyzed in the previous section. It accounts for the different density in GPS stations and the parameter D reflects the level of spatial resolution that can be obtained in each area. The main parameter that controls the resolution is the w_t and its value has to be calibrated in order to balance resolution and noise, due to small local velocity differences of the velocity field. One drawback of the method is that there is not an objective way to choose between the proposed different types of weighting; it is shown in this section that different types of weighting can lead to different results. The configuration Gaussian + Voronoi seems more robust since: the density of GPS stations in the Apennines is generally high (this is also represented by Figure 4.9) and then it is probably not necessary to use a distance weighting function as smooth as the quadratic form; moreover, the Voronoi weighting function takes into account both azimuthal and radial stations' distribution, while azimuthal weighting function does not.

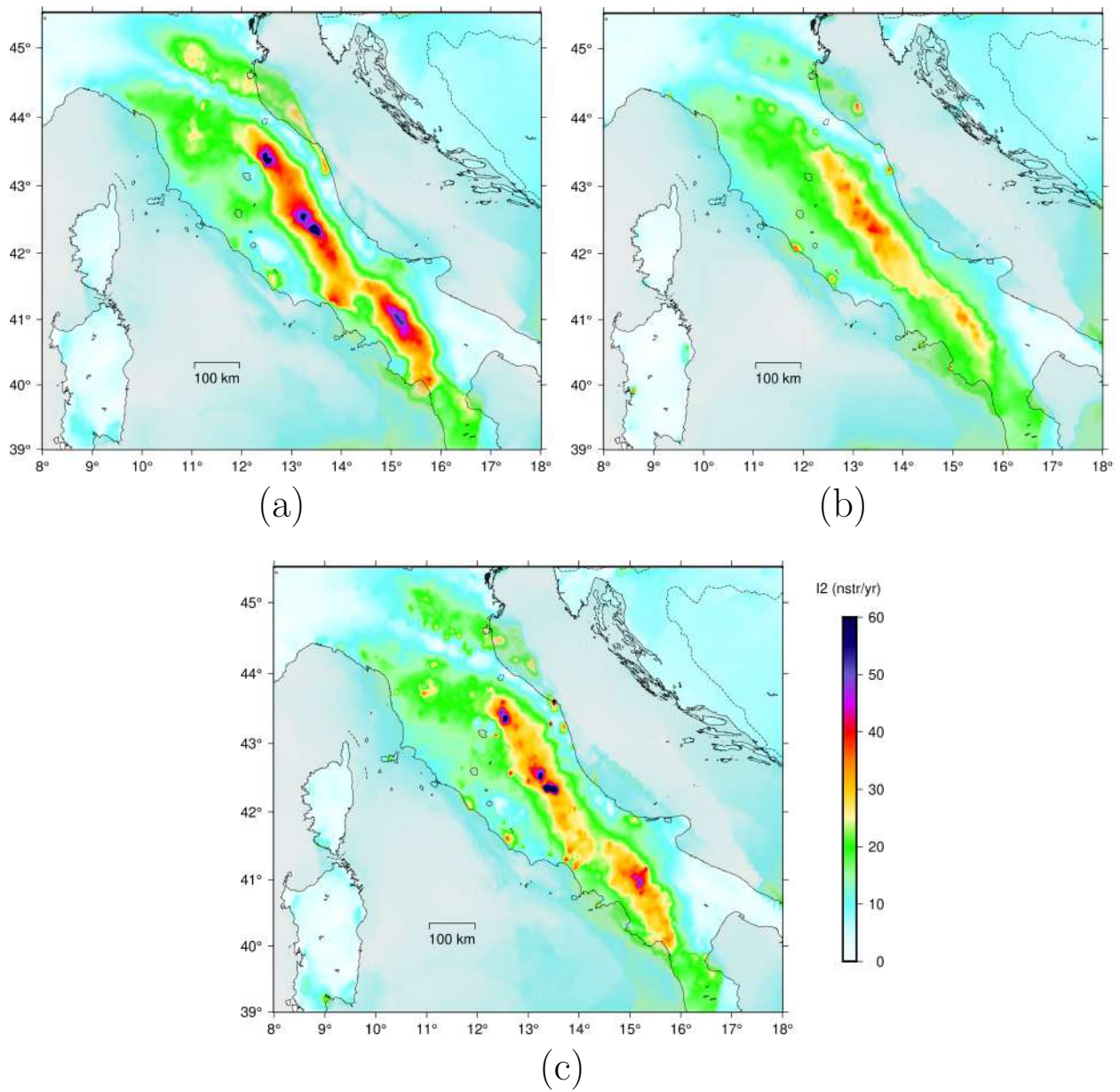


Figure 4.10: *Second invariant of strain rate computed through VISR method, from the filtered GPS dataset, in different cases: a) Gaussian + azimuthal weighting and $w_t = 16$ b) Quadratic + Voronoi weighting and $w_t = 4$ c) Quadratic + azimuthal weighting and $w_t = 4$*

4.3 Wavelets method

The wavelet-based method from Tape et al. 2009 consists in estimating a continuous spatial velocity field using an expansion of basis functions; these basis functions are a class of wavelets on a sphere.

The first step in wavelet analysis is to start with a function Ψ , called *mother function*, and generate a family of scaled and translated versions of the function; in one dimension this becomes:

$$\Psi_{a,b}(x) = \frac{1}{\sqrt{a}} \Psi\left(\frac{x-b}{a}\right) \quad (4.7)$$

Where a is the scaling parameter and b is the translating one. In wavelet analysis different types of mother wavelets are possible; given a set of wavelets, derived from the mother function through translation and scaling, a projection for a function f on this set is defined as:

$$W_{\Psi}(a, b) = \langle f, \Psi_{a,b} \rangle = \int_{-\infty}^{\infty} f(x) \bar{\Psi}_{a,b}(x) dx \quad (4.8)$$

Where $\bar{\Psi}_{a,b}$ indicate the complex conjugate of $\Psi_{a,b}$. This convolution, which is similar to a Fourier transform but in a scale-time domain, is called *continuous wavelet transform* (CWT) and holds only under specific conditions for ψ that makes it an *admissible wavelet*. For an admissible wavelet also the *inverse* continuous wavelet transform (iCWT) exists and lead to $f(x)$ from $W_{\Psi}(a, b)$.

For a function that is defined on the surface of a sphere, that is $f = f(\theta, \phi)$, where θ is the co-latitude and ϕ is the longitude, it is again possible to define a wavelet analysis. For a wavelet on a sphere (i.e. a spherical wavelet) translation is replaced by rotation with Euler angles and dilatation is re-defined properly through a sequence of: stereographic projection, dilatation by a to the projection and inverse stereographic projection (details in Antonie and Vandergheynst 1998). Thus, with the action of rotations and dilatations, it is again possible to define a CWT, in analogy with the 1-D simple case in (4.8), but *spherical*, i.e. for a function f defined on a sphere.

A continuous velocity field on a sphere is given by:

$$\mathbf{v}(\theta, \phi) = v_{\theta}(\theta, \phi) \hat{\boldsymbol{\theta}} + v_{\phi}(\theta, \phi) \hat{\boldsymbol{\phi}} \quad (4.9)$$

where θ and ϕ are distance from center, co-latitude and longitude respectively and $\hat{\boldsymbol{\theta}}$, $\hat{\boldsymbol{\phi}}$ the corresponding versors. Let's consider as mother function a *Difference of Gaussian* (DOG) spherical wavelet that is obtained as the difference of the inverse

stereographic projection of an isotropic Gaussian and of a dilated version of it (figure Figure 4.11B). We can then represent each component of the continuous velocity field in (4.9), which is a scalar function, with a set of wavelet functions derived from the mother. It is proved that it is possible to build a discrete set of wavelet functions spanning the whole space on the sphere surface appropriately discretizing the scaling parameter a and the positions \mathbf{x} for DOG wavelets on the sphere (Bogdanova et al. 2005). The discretization of position results from defining a set of grids G_q for a set of *resolutions* q (figure Figure 4.11A) and, for each resolution, q , a scale parameter given by $a_q = 2^{-q}$. This leads to define the set:

$$F = \{\Psi_{\mathbf{x}_{q,j}}(\mathbf{x}), \mathbf{x}_{q,j} \in G_q, q \in \mathbb{N}\} \quad (4.10)$$

If we want to represent a band-limited function, we don't need all the elements in the set F but only elements in a finite set $F_{q_{max}}$ with $q \leq q_{max}$ where q_{max} is associated to the maximum representable band-width and then to a minimum resolution spatial scale.

Any scalar function f whose band-width doesn't exceed the one associated to the finest scale q_{max} can be written as:

$$f(\mathbf{x}) = m_k g_k(\mathbf{x}) = \mathbf{g}^T \mathbf{m} \quad (4.11)$$

Where g_k are functions in the finite set $F_{q_{max}}$ of dimension M and m_k are scalar coefficients. In our problem we have a finite set of observations $(v_{\theta_i}, v_{\phi_i})$ on the sphere at points (θ_i, ϕ_i) where $i = 1, \dots, N$. Evaluating (4.11) at the observation points leads to:

$$v_{\theta_i} = c_k g_k(\theta_i, \phi_i) + n_{\theta_i} \quad v_{\phi_i} = d_k g_k(\theta_i, \phi_i) + n_{\phi_i} \quad (4.12)$$

Where n represents the noise contribution. If we insert v_{θ_i} and v_{ϕ_i} into a unique vector of measurements \mathbf{f} of dimension N we can write:

$$\mathbf{f} = \mathbf{G}\mathbf{m} + \mathbf{n} \quad (4.13)$$

where \mathbf{G} is a $N \times M$ matrix which has elements $G_{ik} = g_k(\theta_i, \phi_i)$ and \mathbf{m} is the model parameter vector. The problem of finding optimal coefficients \mathbf{m} is undetermined since $M > N$, because $F_{q_{max}}$ is not an orthogonal basis. In the inversion of the direct problem (4.13) it is then necessary a form of regularization. Tape et al. 2009 estimate the model vector minimizing the regularized least-squares functional and using the norm of the model gradient as regularization. Thus, the problem in

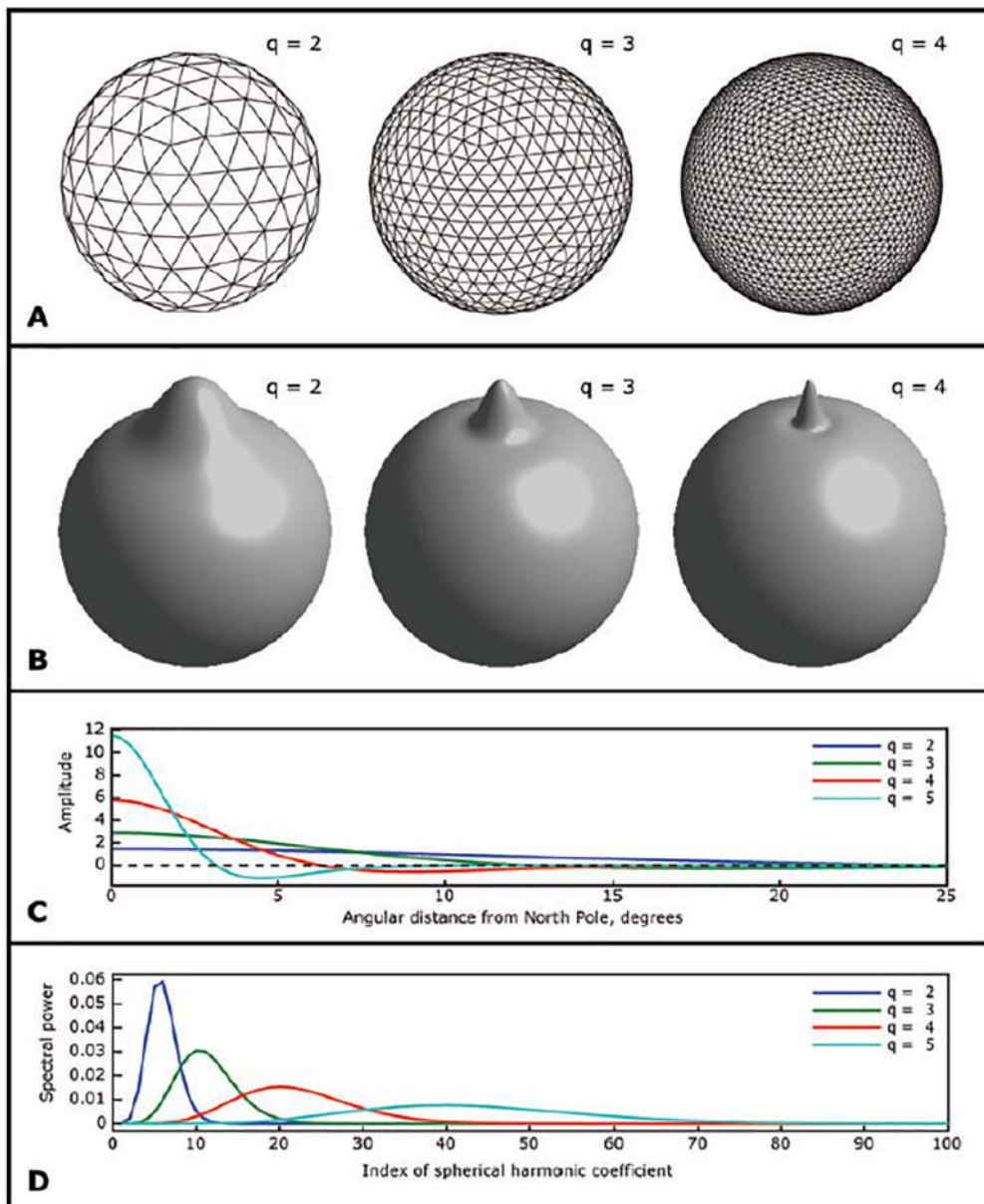


Figure 4.11: *Spherical wavelet frame functions. (A) Triangulated spherical grids used for determining the locations for the centres of the spherical wavelet frame functions. From left- to right-hand side are grids for orders $q = 2$ (162 vertices), $q = 3$ (642 vertices) and $q = 4$ (2562 vertices) (B) Three different scales of a DOG (Difference of Gaussian) spherical wavelet centred at the North Pole. (C) Corresponding profiles of wavelets in (B), for a fixed longitude ϕ . (D) Corresponding spectra of wavelets in (B). Figure from Tape et al. 2009*

(4.13) transforms in minimizing:

$$F(\mathbf{m}) = \frac{1}{2}(\mathbf{G}\mathbf{m} - \mathbf{d})^T \mathbf{C}^{-1}(\mathbf{G}\mathbf{m} - \mathbf{d}) + \frac{1}{2}\lambda^2 \mathbf{m}^T \mathbf{S}\mathbf{m} \quad (4.14)$$

Where \mathbf{d} is the vector of data, \mathbf{C} is the covariance matrix and \mathbf{S} is the regularization matrix. The solution of this direct problem is:

$$\mathbf{m} = (\mathbf{G}^T \mathbf{C} \mathbf{G} + \lambda^2 \mathbf{S})^{-1} \mathbf{G}^T \quad (4.15)$$

The proper parameter λ is chosen by ordinary cross validation taking the minimum resulting value.

We apply the wavelets method on the filtered dataset in Figure 3.5 . We estimate the strain rate using different values of the resolution q . The choice of q mainly depend on the spatial scale of interest that we desire (see Table 4.1). The allowable q -values depend on the local density of stations. Where stations are denser in space, higher values of q are admitted while for regions in which stations are sparse only small q -values are available. Figure 4.12 shows the maximum q scale wavelet that covers each area (q_{max}), where the coverage is determined by the length scale for each spherical wavelet (Table 4.1). We can observe that for all the region of interest a $q_{max} = 8$ is available; it corresponds to a spatial arc length of 27.55 km. A value of 9 is available in large part of the region while values grater then 9 don't cover the total region and are highly localized in space. It is in principle possible to apply the method exploiting, for each region, all the q values up to their maximum; however there are some drawbacks: the first is that very high resolutions ($q_{max} > 9$) are more sensible to local variations of velocity data at small scales of few kilometers, which could not reflect changes in tectonics; the second is that the strain rate derived by the resulting velocity field is computed at different scales in different points on the map allowing one to spuriously infer spatial variability where none exists. For these reasons, we prefer to limit q choosing values of q_{max} available for the whole, or for large part, of the region.

We compute different maps for different value of the q_{max} ; in Figure 4.13 we show the resulting scalar fields for the second invariant of the strain rate, defined by equation (2.6b), for $q_{max} = 7, 8, 9$. The qualitative difference between the figures consists in a different smoothing of the second invariant field, defined in equation (2.6b), from the map with smoother distribution of I_2 (a) with $q_{max} = 7$, to the more detailed one (b) with $q_{max} = 9$. We compute the *root mean squared error* RMSE and we plot it against q_{max} ; the result is shown in figure Figure 4.14. We observe a significant change in the slope for values of q_{max} ranging between 7 and 9.

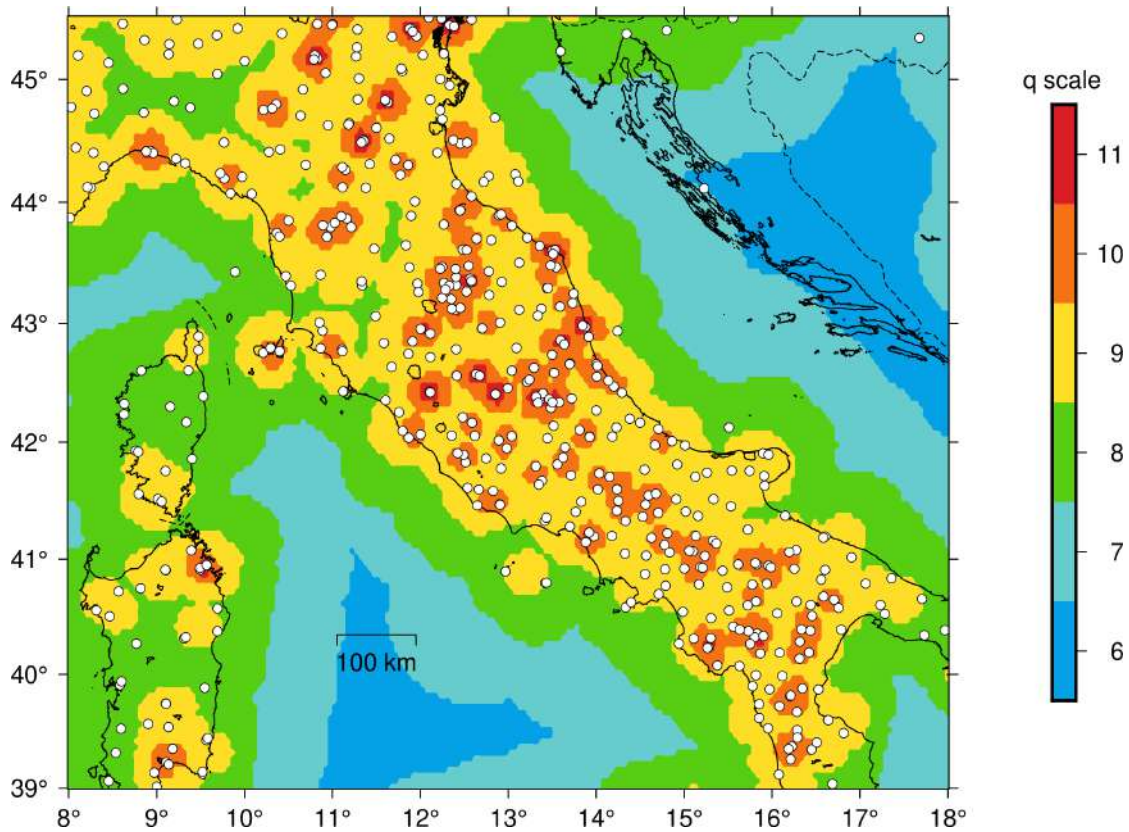


Figure 4.12: *Maximum values of spherical-wavelet orders based on the GPS station distribution. White circles represent GPS stations. The density of the geodetic points controls the selection of spherical wavelets (wavelet center points are not shown). The color map shows the maximum q scale wavelet that covers each area where the coverage is determined by the length scale for each spherical wavelet.*

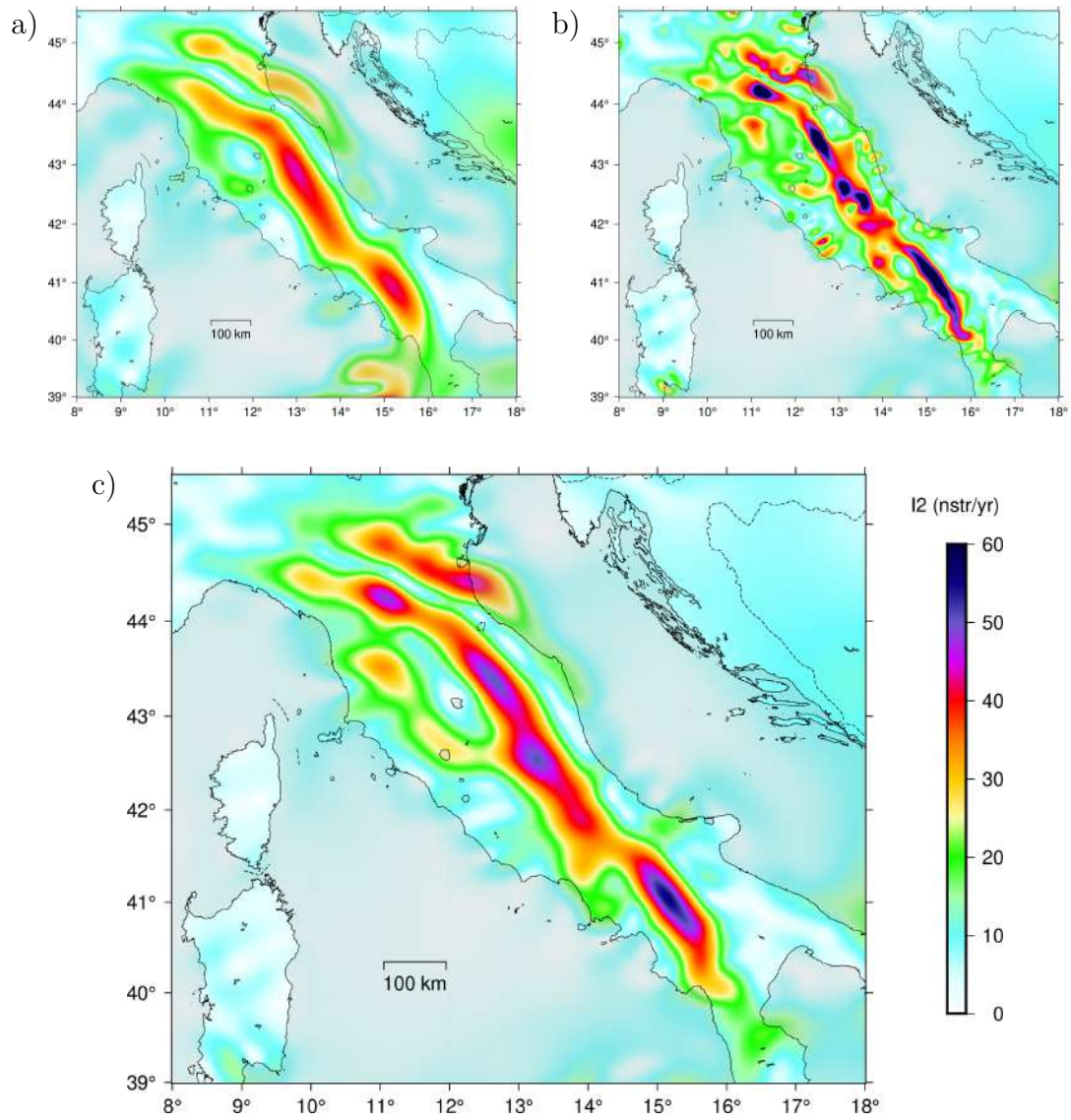


Figure 4.13: *Second invariant of the strain rate computed from the filtered GPS dataset considering: a) $q_{max} = 7$, b) $q_{max} = 9$, c) $q_{max} = 8$.*

Resolution q	Scale	Faces	Vertices	Average side arc length	
0	2^0	20	12	63.435°	7053.64 km
1	2^1	80	42	31.718°	3526.84 km
2	2^2	320	162	15.859°	1763.41 km
3	2^3	1'280	642	7.929°	881.71 km
4	2^4	5'120	2'562	3.965°	440.85 km
5	2^5	20'480	10'242	1.982°	220.43 km
6	2^6	81'920	40'962	0.991°	110.21 km
7	2^7	327'680	163'842	0.496°	55.11 km
8	2^8	1'310'720	655'362	0.248°	27.55 km
9	2^9	5'242'880	2'621'442	0.124°	13.78 km
10	2^{10}	20'971'520	10'485'762	0.062°	6.89 km
11	2^{11}	83'886'080	41'943'042	0.031°	3.44 km
12	2^{12}	335'554'320	167'772'162	0.016°	1.72 km

Table 4.1: Table showing geometric properties of spherical-triangular grids for a certain resolution q

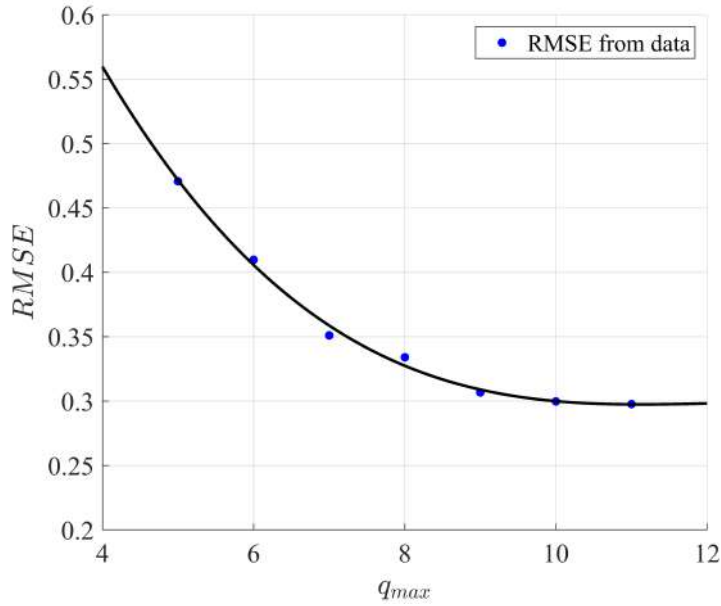


Figure 4.14: Root mean squared error computed for different trials with $q_{max} = 6, 7, 8, 9, 10, 11$ (blue points). The black line is a third order polynomial plotted as reference.

We consider the map with $q_{max} = 8$ to be a good choice since:

- The value of $q_{max} = 8$ is such that it lies in the region in which the RMSE curve changes its slope (see Figure 4.14).
- The corresponding spatial scale for wavelets (~ 28 km) is compatible with the scale length of tectonic changes.
- In all the studying region is available a value $q_{max} = 8$; the resulting map admit the same resolution in each point.

For the selected map we can analyze also the data vs model map and the residuals map (both are shown in Figure 4.15). The dilatation rate map is shown in Figure 4.16. The residuals are smaller, in average, than the ones considered from the previous two methods in sections 4.2 and 4.1. We see that this method, in comparison with the VISR method, is more robust with respect to outliers: a comparison between the wavelets method with $q_{max} = 8$ and the VISR map with weighting Gaussian + Voronoi with $w_t = 16$ (Figure 4.13c and Figure 4.6b respectively) shows that in the VISR map there are more small spots of localized strain, despite the comparable resolution. This justify the employment of this method to filter out outliers from the initial dataset (3.2).

In conclusion, the wavelets method has the advantage that the choice of resolution is based on a parameter directly linked with the spatial length of interest, i.e. q_{max} . Moreover, this method is more robust with respect to the outliers than the others employed in this thesis. For this reason, this method can be useful to identify anomalous values of velocity in the GPS velocity dataset. One con is that no intermediate resolutions are possible between the ones corresponding to subsequent values of q_{max} since q is a discrete parameter; then, intermediate maps to those presented are not possible.

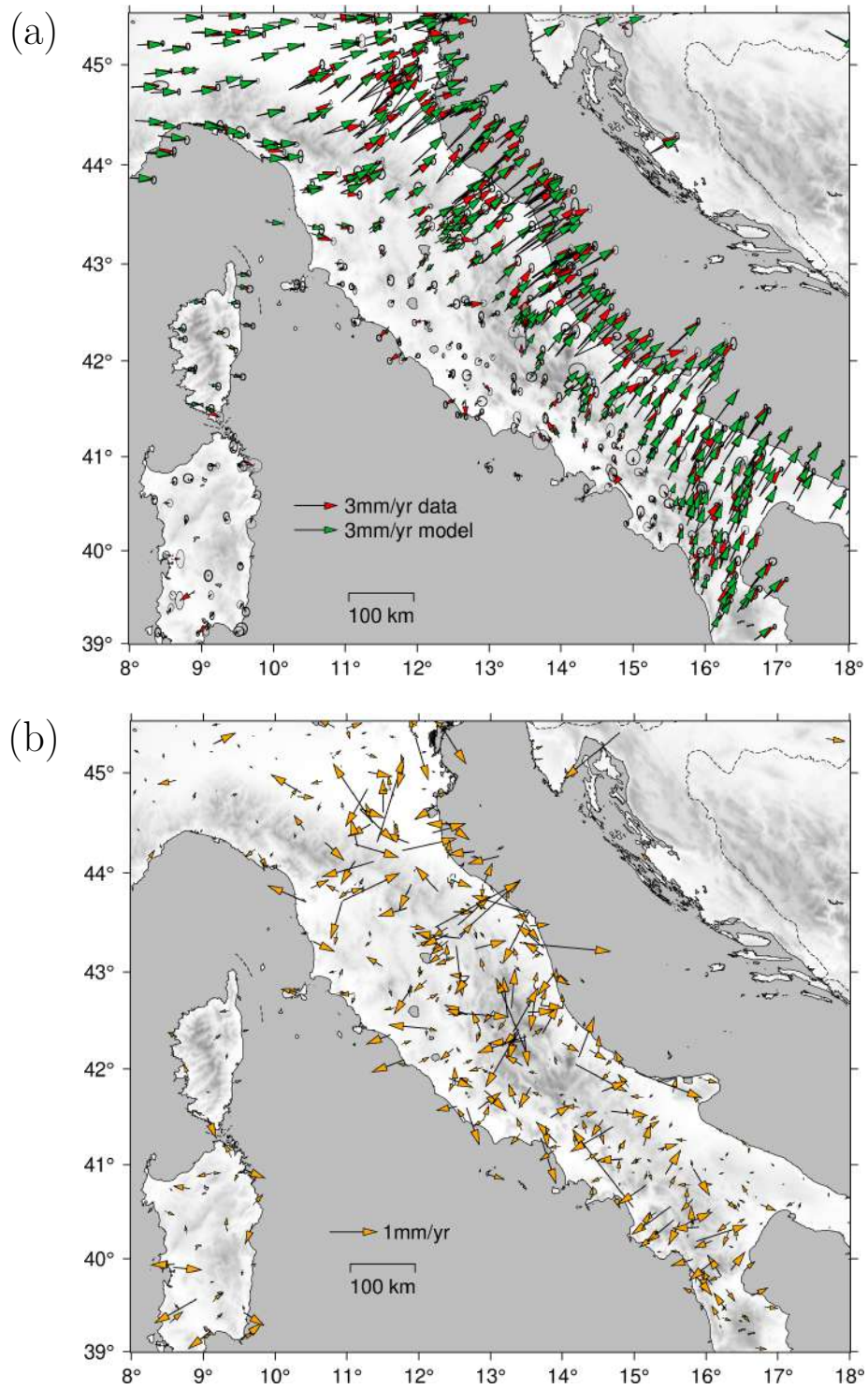


Figure 4.15: a) Plot of the modeled velocity field from wavelets method with $q_{max} = 8$ (green arrows) against the GPS velocity dataset (red arrows). b) Residuals from the inversion (orange arrows).

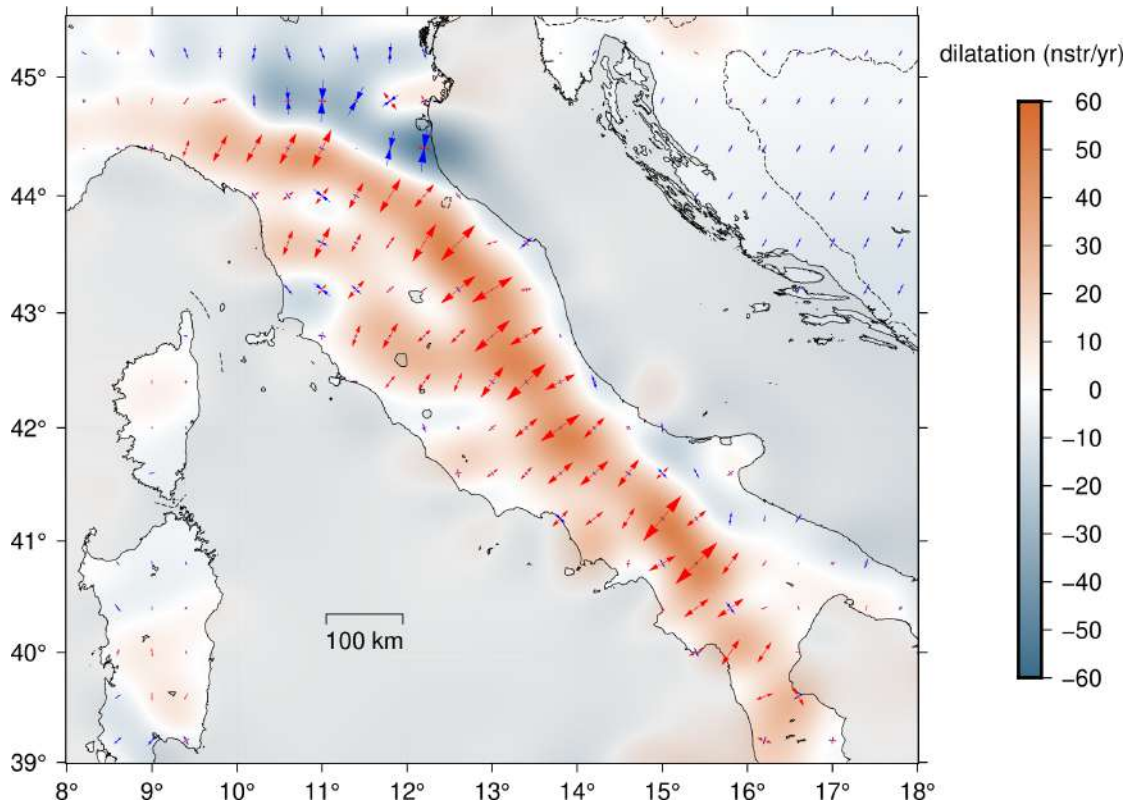


Figure 4.16: *Map of dilatation rate and principal axis of strain rate from wavelets method with $q_{max} = 8$.*

4.4 Discussion of the resulting strain rate field

In the previous sections we have explored different methods to compute the horizontal strain rate field from GPS velocity data. We indicate as a good compromise between resolution and robustness the strain rate map obtained through the wavelets method with $q_{max} = 8$ (Figure 4.13c). In fact, even if the strain rate map Figure 4.13c is comparable with Figure 4.6b for the VISR method and with Figure 4.2c (or Figure 4.2b) for the nearest neighbor algorithm, the wavelets map has some more advantages. It has a smooth distribution of I_2 , the method is robust with respect to the outliers and the choice of the best map is less subjective, since the main parameter q_{max} can be used to select the spatial length of interest (in our case, a spatial length of ~ 28 km, suitable to represent tectonic processes, correspond to $q_{max} = 8$); in fact, a main disadvantage of the other two methods is that there is not a golden rule that permits one to choose an appropriate map, but the choice has to be weighted basing on different parameters' configurations. In the case of wavelets method the choice is based only on the q_{max} parameter. For these reasons, we select for further analysis the map obtained by wavelets method with $q_{max} = 8$. We now discuss the fundamental features of the resulting deformation rate field (Figure 4.13c). The main characteristic is the presence of an extensional belt running along the Apennine chain from the Calabria region to the northern Apennines where three sub-parallel belts of deformation rate are observed. The central belt is a dilatation belt that lies on the inner Apennines as the north part of the extensional belt running through all Italy. An outer belt is located on the Apennine front and shows an almost N-S oriented shortening with its higher value in the Emilia Po Plain and lower rates offshore in the Adriatic sea; the shortening continues in the Marche region along the coast but NE-SW oriented. The third belt is located in the inner northern Apennines and it is characterized by NE-SW oriented extension in the Tuscany region and joins the central chain in correspondence of the Umbria region. A detail of this three-belts structure is shown in figure Figure 4.18 which shows a profile distribution along the line ranging from the point A to B (figure Figure 4.17); we consider stations, topography and second invariant of strain rate field in a rectangular box with a width of 100 km centered on the dashed blue line AB. The velocity passes from a value of ~ 0.5 mm/yr in the Tyrrhenian sector to values of ~ 2 mm/yr in the Adriatic sea with a peak value that goes over the 3 mm/yr and the velocity rising occurs crossing the Apennines. This results in three well defined peaks of the deformation rate as shown by the top of Figure 4.18. Another detail is shown in Figure 4.19 for the southern Apennines. It is again considered a rectangular box with a width of 100 km but this time centered on the line from C to D in Figure 4.17. We can see that this time the deformation rate has only one main peak that stands on the Irpinia region with a monotonically increasing velocity field when passing from B to C.

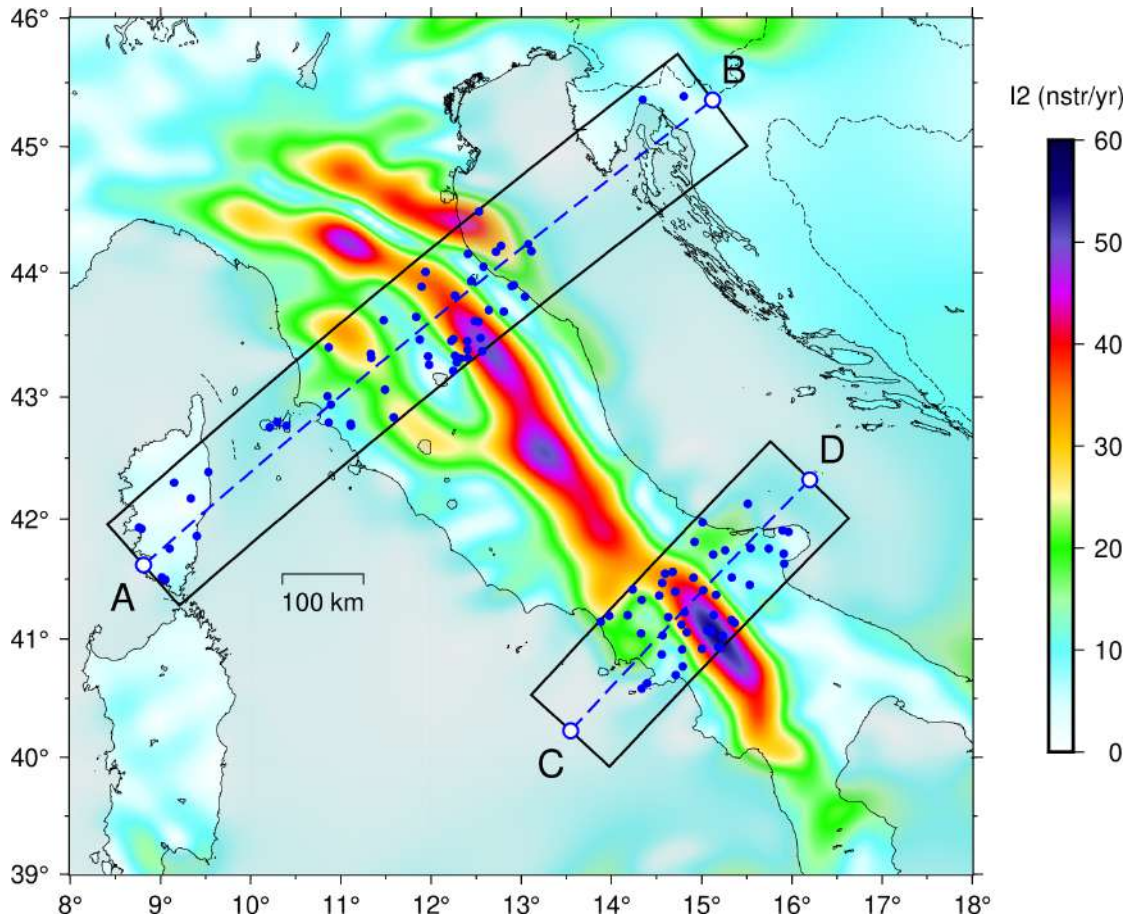


Figure 4.17: *Detail of the second invariant from wavelets method with $q_{max} = 8$. The rectangular regions in black are inspected in Figure 4.18 and Figure 4.19 in terms of velocity and deformation rate. Inside the 100 km wide rectangles, the GPS stations are shown with blue points while the dashed blue lines represent the tracks from the points A, B and C, D.*

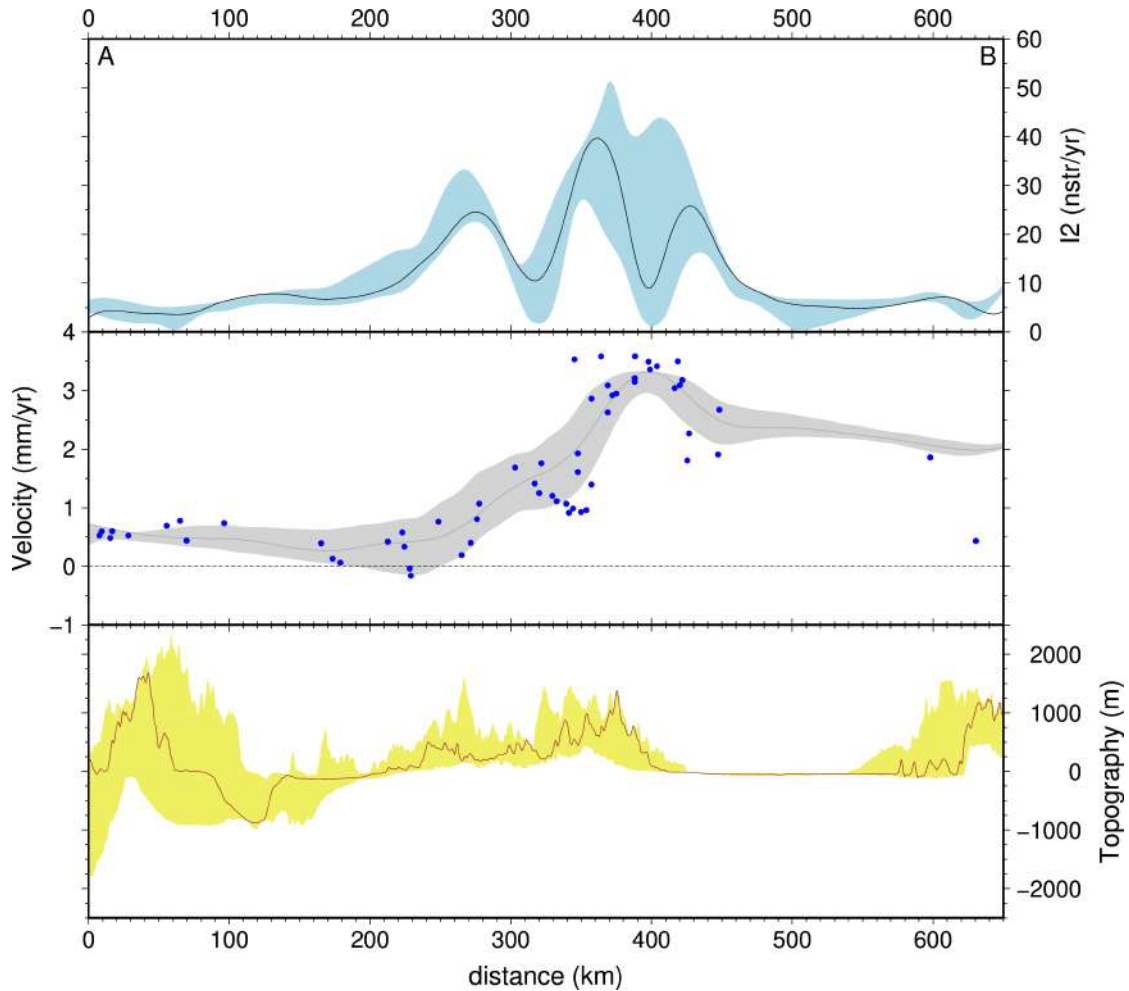


Figure 4.18: Analysis of the area shown in Figure 4.17. On the x -axis is shown the distance from the point A in km. Top: second invariant of the strain rate plotted along the AB line (grey) and its variation in the swath profile (blue shadow). Middle: GPS velocity (blue points), modeled velocity along the AB line (gray line) and its variation in the swath profile (gray shadow). Bottom: topography profile along the AB line (brown line) and its variation in the swath profile (yellow shadow)

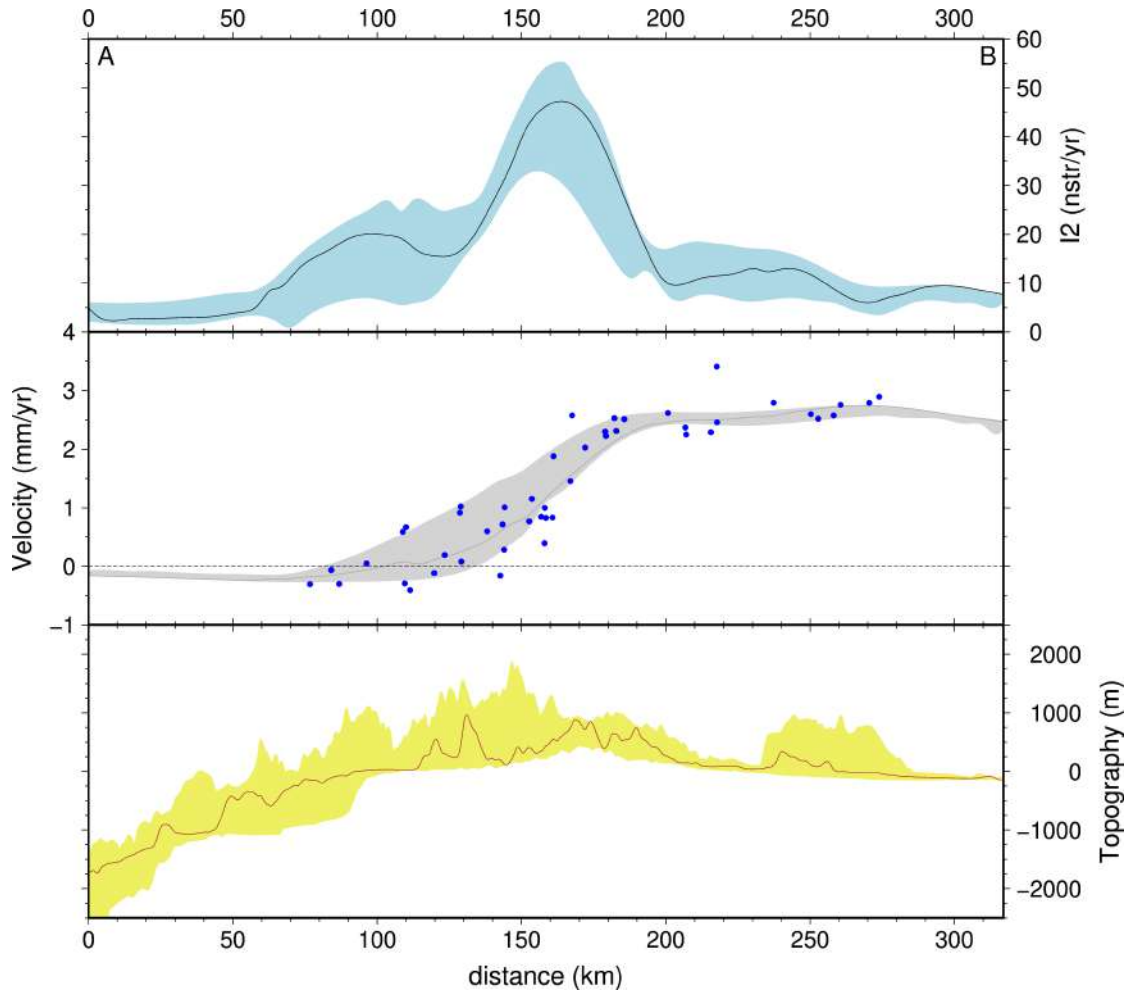


Figure 4.19: Analysis of the area shown in Figure 4.17. On the x-axis is shown the distance from the point C in km. Top: second invariant of the strain rate plotted along the CD line (grey) and its variation in the swath profile (blue shadow). Middle: GPS velocity (blue points), modeled velocity along the CD line (gray line) and its variation in the swath profile (gray shadow). Bottom: topography profile along the CD line (brown line) and its variation in the swath profile (yellow shadow)

Chapter 5

Comparison of seismic and geodetic strain rate

In this chapter we assess if the computed geodetic strain rate field is representative of the accumulated strain, ϵ_{ij}^R , $i, j = 1, 2, 3$, which is released through earthquakes. Following Stevens and Avouac 2021, a first order correspondence between principal axes of geodetic strain rate and those relative to the released strain rate is expected.

Focal mechanisms data on past earthquakes are used to test if this hypothesis holds. Focal mechanisms analyzed in this thesis are the result of the work of Sani et al. 2016. Sani et al. 2016 use focal mechanisms from various global and regional catalogs based on seismogram modeling, merging them into a dataset, containing overall ~ 4000 focal mechanisms data. They use the Kostrov method (Kostrov 1974, see equation (2.25)) to compute the "sum focal mechanism" on hexagonal equiareal cells with 10 km of side; moreover, using the upper-crust surface from Molinari and Morelli 2011, they differentiate them between upper crust focal mechanisms and deeper ones. In fact, on the basis of the seismic wave speed, Earth's continental crust can be divided into different layers; the upper crust is the shallowest part of the continental crust, having a brittle elastic behaviour with respect to its lower and more ductile part. The considered focal mechanism sum data are relative to the upper crust where earthquakes occurrence is expected.

We compare the distribution of ϵ_{ij}^R , resulting from the sum focal mechanisms, with the geodetic strain rate computed from the wavelets method using $q_{max} = 8$ (see section 4.3). The sum focal mechanisms computed in each hexagonal cell are shown in Figure 5.1. From now on, the border of the polygon centred on the Apennines (outer grey line in Figure 5.1) will delimit our studying region.

The comparison between geodetic strain rate and ϵ_{ij}^R is made by analyzing differences in principal strain axes orientations between the two tensors. A drawback of this analysis is that the geodetic strain rate is a 2D tensor, but ϵ_{ij}^R , computed through the Kostrov formula, is based on the sum of focal mechanisms and then it

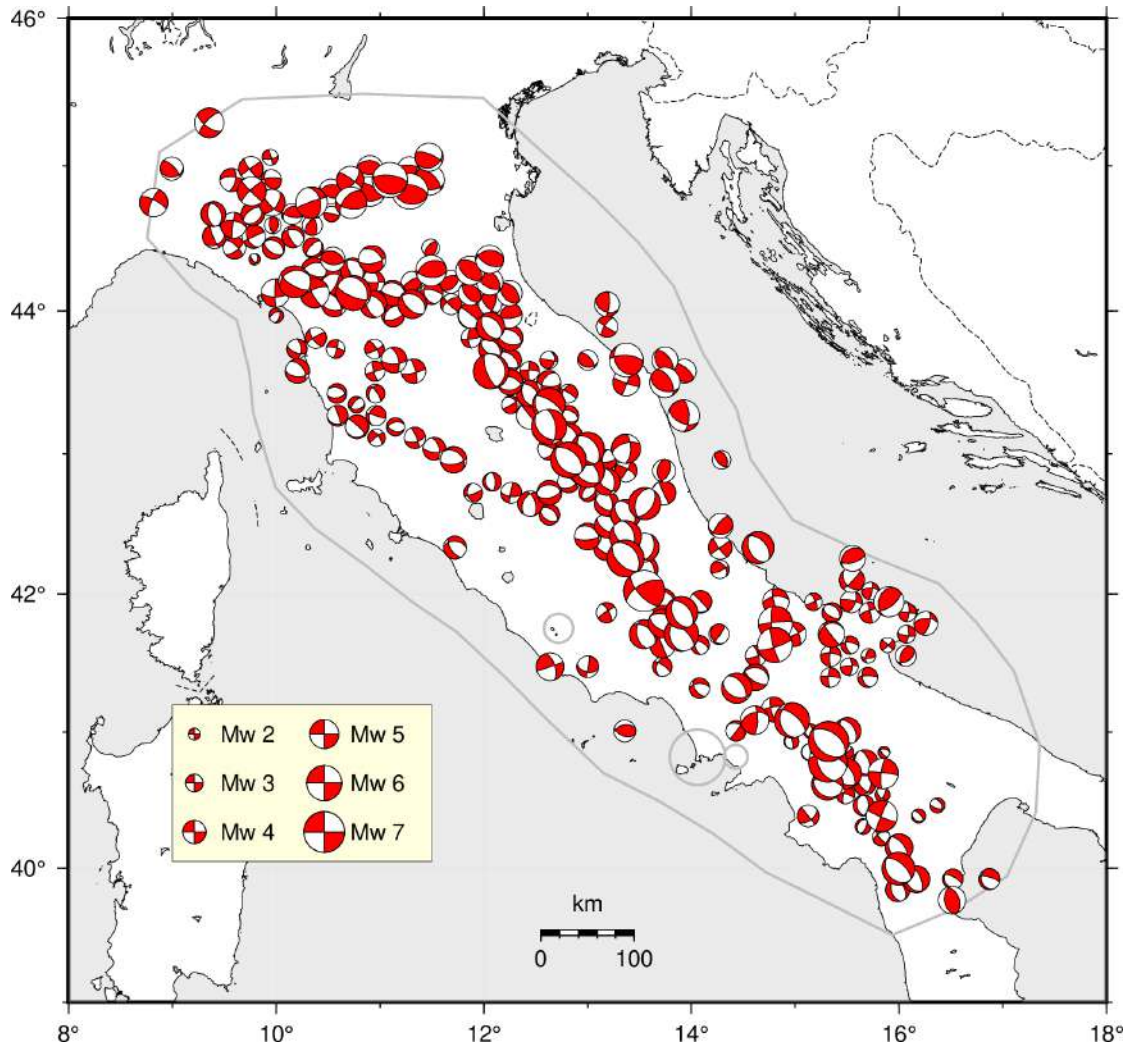


Figure 5.1: "Sum focal mechanisms" from Sani et al. 2016 collected in the time span 1905-2015. We consider events inside a polygon (delimited by the outer grey line) and we exclude events inside the circular volcanic masks presented in 3.2 (grey line circles). Beach balls' dimension is proportional to the moment magnitude M_w of the sum event.

is a 3D moment tensor. In order to obtain an even comparison, given the different dimension of the two tensors, we need to consider horizontal principal directions for ϵ_{ij}^R since, in general, its principal directions could not be horizontal. The adopted method to obtain horizontal principal directions is exposed in the following.

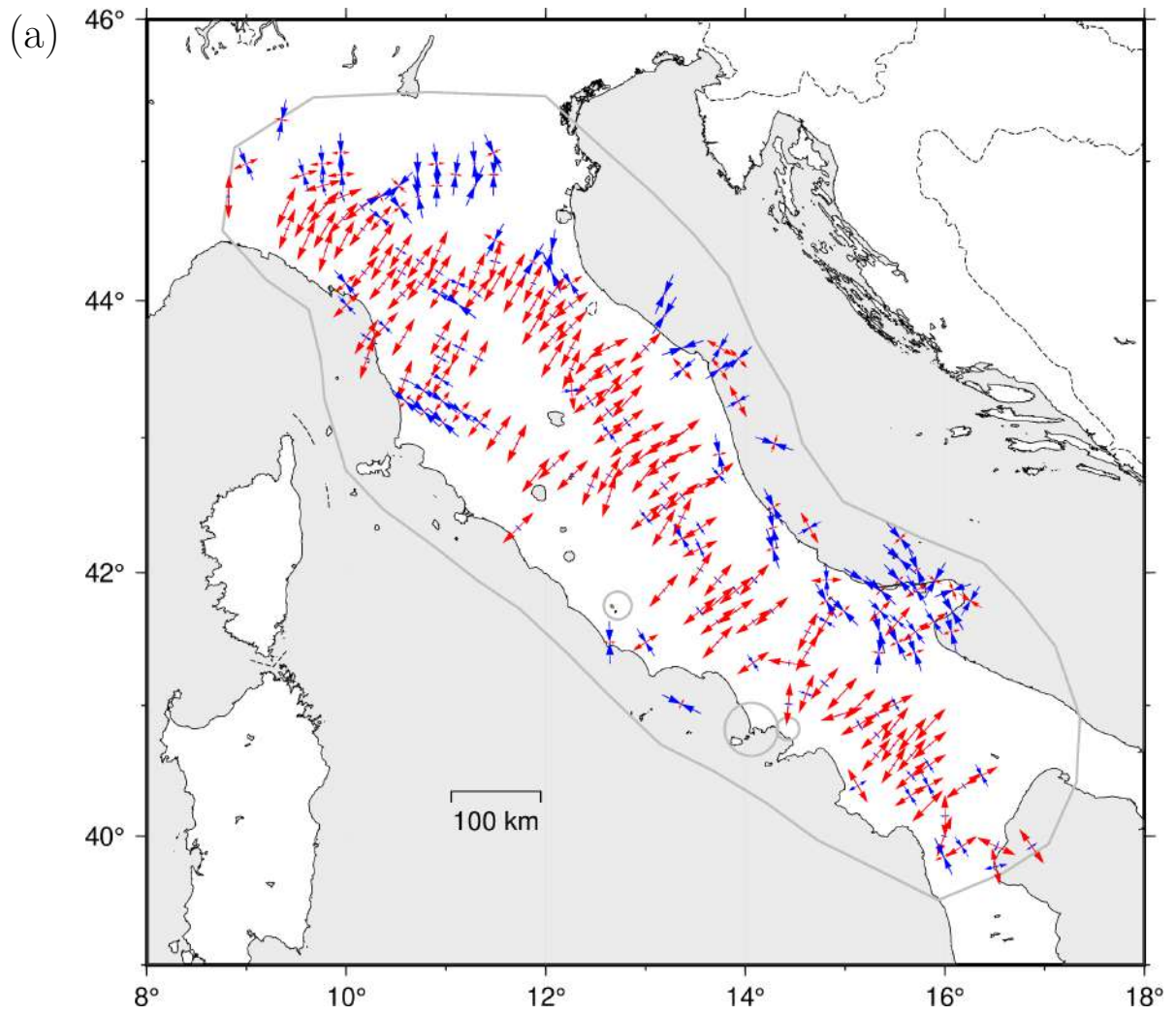
Let's focus on a general direction of strain rate identified by the unit vector \mathbf{n} having components n_k with $k = 1, 2, 3$. The strain value S_n along this direction will be given by:

$$S_n = n_i \epsilon_{ij}^R n_j \quad (5.1)$$

with sum on equal indices. If the direction of \mathbf{n} is horizontal then its third component n_3 is zero; this means that the computation of S_n through (5.1) involves only the 2x2 minor of the ϵ_{ij}^R tensor relative to the horizontal components, i.e. ϵ_{ij}^R with $i, j = 1, 2$. Searching for the principal horizontal components of the strain tensor means to find horizontal vectors \mathbf{n} that maximise and minimize S_n , but this procedure is also equivalent to find the eigenvectors for the 2x2 minor of the ϵ_{ij}^R tensor. In conclusion: to find the principal horizontal components of the ϵ_{ij}^R tensor reduces to find the eigenvectors of its 2x2 minor ϵ_{ij}^R with $i, j = 1, 2$.

Accounting for the previous considerations it is then possible to plot the resulting eigenvectors for the horizontal principal components of the two tensors. They are shown in Figure 5.2a for the geodetic strain rate tensor and in Figure 5.2b for ϵ_{ij}^R . Observing the two figures, the directions of horizontal principal strains appear similar even if those derived from earthquakes show locally a greater heterogeneity. Both figures show a dilatation belt running along the Apennines and an outer compressive belt toward the Adriatic sea. Part of this belt is visible in the Po Plain where the compression is roughly N-S. To quantify the disagreement (misfit) between the principal directions, we compute the angular difference (in absolute value) between the two couple of axes in the same spatial position; each angular difference will range from 0° to 90° and represents the misfit between accumulated strain rate and ϵ_{ij}^R . The distribution of the angular differences is shown in Figure 5.3 for each hexagonal cell in the region of interest. The misfit is also shown on the overall area in Figure 5.4; in the same figure it is also shown, as a reference, a simulation of a uniform distribution of angular misfit, representing a case of no correlation between the axes directions. The $\sim 51\%$ of the comparisons have an angular difference that is less than 25° . The spatial distribution of misfit shows a worse agreement in east Piedmont Apennine (in an area centered on 12°E and 44°N) where focal mechanisms indicate a change from extensional to compressive regime (see also Figure 5.1) that is not accounted by the geodetic strain rate.

To test if the agreement between principal strain directions is significant, we can compare the observed distribution of angular differences with a uniform dis-



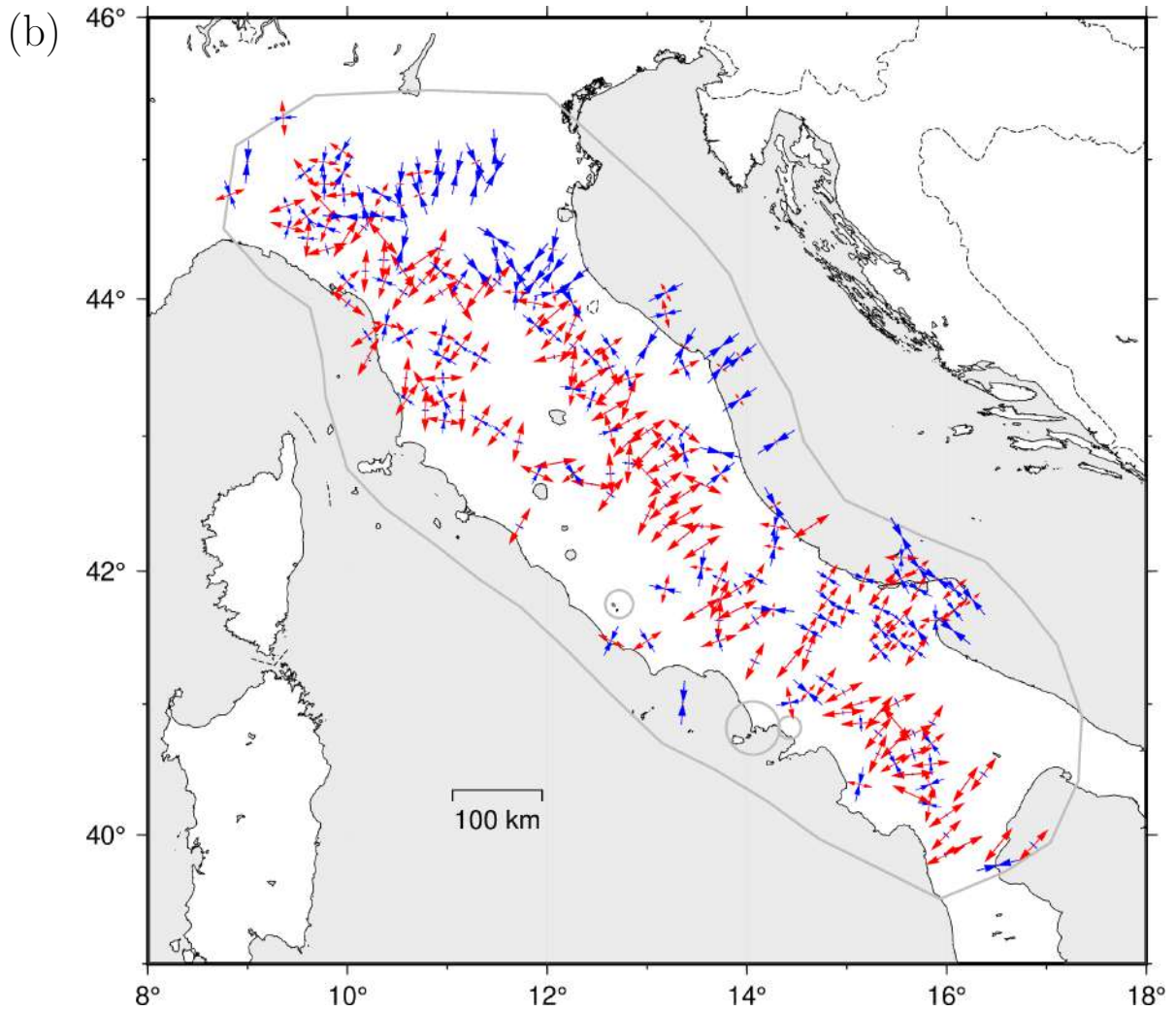


Figure 5.2: *Principal directions from: (a) geodetic strain rate resulting from wavelets method with $q_{max} = 8$ and (b) ϵ_{ij}^R from Sani et al. 2016. In both the cases, principal axes are normalized so that the sum of the vectors defining the axes has modulus equal to 1.*

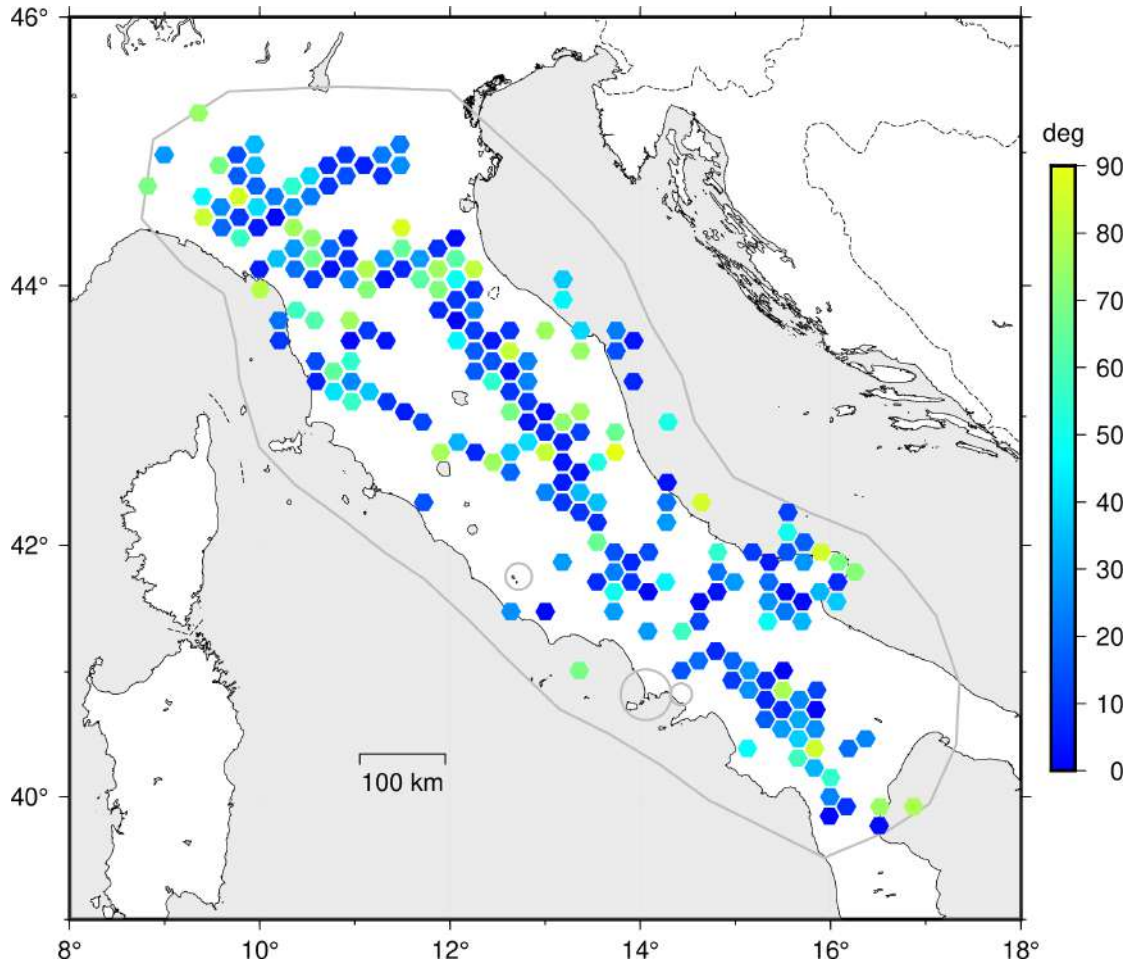
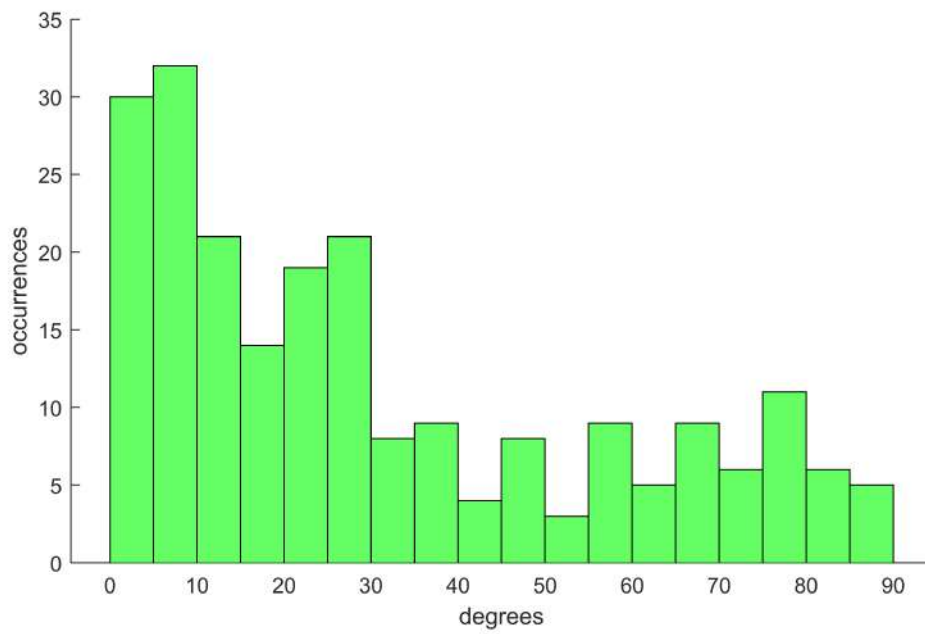


Figure 5.3: Angular misfit for directions of horizontal principal strains of geodetic strain rate and ϵ_{ij}^R computed for each hexagonal cell (used for the computation of ϵ_{ij}^R through the sum of focal mechanisms).

(a)



(b)

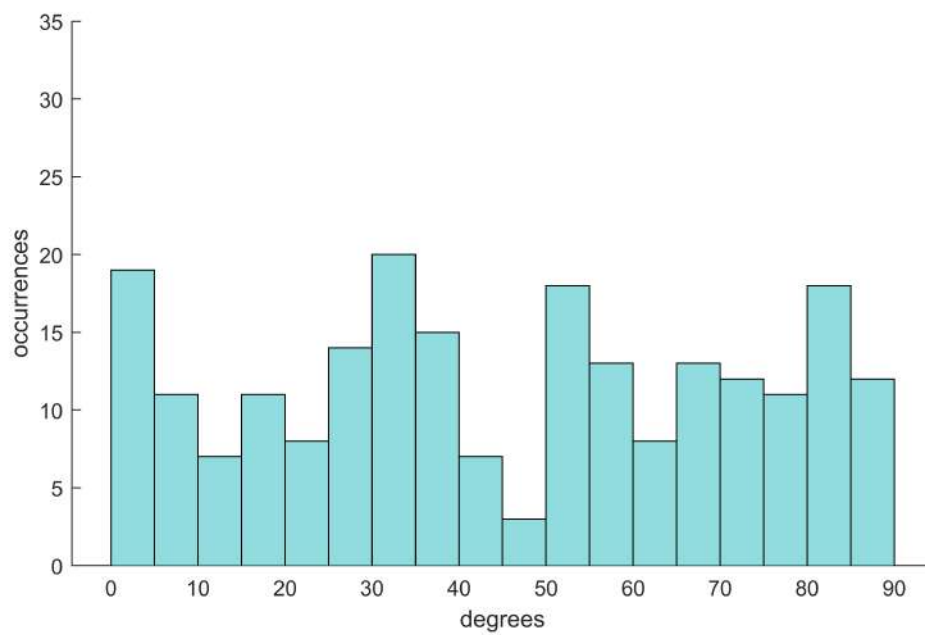


Figure 5.4: a) Histogram of the angular misfit for directions of horizontal principal strains of geodetic strain rate and ϵ_{ij}^R . b) Histogram representing a random distribution of misfit (a case of no correlation between directions)

tribution (Figure 5.4). A chi-square test on the goodness of fit with a random distribution results in rejecting the null hypothesis for which the observed distribution is uniform at less than 1% of significance.

The larger scatter in ϵ_{ij}^R shows that it is more heterogeneous than the geodetic strain rate (Figure 5.2). The larger variability could be due to a lack of resolution of the geodetic strain; the geodetic strain rate is, in fact, the result of an average over a certain spatial length of several km. The distribution of sum focal mechanisms suggests that heterogeneity occurs even at smaller length scales. On the other hand, this variability could be caused by other factors; for example by local heterogeneity of the stress field, induced, for example, by topography, or by heterogeneity in composition of the elastic medium. Even the interaction between earthquakes, through stress transfer, could have an influence in orientation of strain principal axes.

However, this first order agreement can be considered sufficient to sustain that the geodetic strain rate field is representative of the accumulated strain that is released through earthquakes. This enforces the hypothesis of a stationary accumulation and of a proportionality between stress rate and geodetic strain rate (hypotheses 1 and 2).

Chapter 6

Earthquake catalogue declustering and Poisson distribution assumption

6.1 Declustering method description

Earthquake clustering is a main character of seismicity and occurs both in space and time. Clustering in space is easily understood thinking at the concentration of earthquakes along main fault traces between tectonic plates and in regional fault systems. On the other hand, clustering in time can be exemplified by the significant increase of seismic activity after an earthquake (it involves the so-called *aftershock* sequences).

Even if a rigorous definition of seismic clusters is lacking, it is understood in a broad sense as a deviation from a time-stationary and space heterogeneous Poisson process. We generally refer to an *independent* seismic event when its occurrence is not caused by earthquake interaction processes (which happens during aftershocks sequences). In other words, an independent event is not triggered by previous events but is driven by interseismic loading. We refer to a set of independent events as the *background seismicity*.

One target of this thesis is to perform an analysis on a seismic catalog composed of independent events; moreover, we are interested in verifying if independent events follow a stationary Poisson process in time. This leads to the need of a declustering procedure, i.e. a method that could separate background events from triggered events. There are several algorithms for this task (an extensive list with a discussion of pros and cons of each method is found in Stiphout, Zhuang, and Marsan 2012); however, generally, applying different declustering models to the same catalog leads to different sets of independent events.

The method used in this thesis is the nearest neighbour clustering analysis technique presented in Zaliapin and Ben-Zion 2013. The method is based on an analysis of the nearest-neighbor distances of events (NDD). Let's consider a specific earthquake in the catalog that we label through the index i ; this event will be characterized by a position (the hypocentral coordinates x_i, y_i, z_i), its occurrence time t_i and a magnitude measured in a certain scale (e.g. a moment magnitude) m_i . The event is then identified as a 5-tuple in the space, time and magnitude (then energy) domain: $(x_i, y_i, z_i, t_i, m_i)$. Considering an event j subsequently occurred to i , we define the distance η_{ij} between the two events as:

$$\eta_{ij} = (t_j - t_i) r_{ij}^{d_f} 10^{-bm_i} \quad (6.1)$$

where r_{ij} is the spatial distance between the hypocenters of the two events, b is the parameter of the Gutenberg-Richter law and d_f is the fractal dimension characterizing the distribution of the hypocenters. The value of d_f is set to 1.2 according to Kagan 1991. The η_{ij} metric decreases as two earthquakes get closer in time and space and as the event i is bigger in magnitude. Note that the previous definition holds only if $t_j > t_i$, otherwise the distance between i and j is formally set to $+\infty$. For an earthquake j we define its *parent* event \bar{i} as the earthquake for which the distance (6.1) is the smallest among all the possible i . A parent event for j is then its closest event as stated in (6.1). Following Zaliapin and Ben-Zion 2013, it is convenient to represent the nearest-neighbor distance η_{ij} in terms of its space and time components:

$$R_{\bar{i}j} = r_{ij}^{d_f} 10^{-bm_{\bar{i}}/2} \quad (6.2a)$$

$$T_{\bar{i}j} = (t_j - t_{\bar{i}}) 10^{-bm_{\bar{i}}/2} \quad (6.2b)$$

With the property $\eta_{ij} = R_{\bar{i}j} T_{\bar{i}j}$ (without sum of indices) or equivalently $\log_{10} \eta_{ij} = \log_{10} R_{\bar{i}j} + \log_{10} T_{\bar{i}j}$. Plotting $R_{\bar{i}j}$ vs $T_{\bar{i}j}$ for all earthquakes j makes possible to identify two different populations. A bimodal distribution in the (T, R) space is observed: a first mode, located closer to the origin, is called *cluster* since is characterized by unusually small distances (representing then clustered events); the other is located farther from the origin (greater nearest-neighbor distances) and it is called *background* since it represents independent events. The bimodal distribution of the nearest-neighbor distances is a general feature of observed seismicity (Zaliapin and Ben-Zion 2013).

The bimodal distribution of events in the (T, R) space results in a bimodal distribution also in the η_{ij} space. The problem consists now in separating the background mode from the cluster one. The adopted method to separate independent events from dependent ones will be exposed in the next section.

6.2 Implementation and results

In this thesis we consider the CLASS catalog (Di Stefano and Chiaraluce 2022) that is a catalog of earthquakes occurred in Italy from 1981 to 2018. The catalog is composed of probabilistic locations, based on P and S waves arrival times recorded at INGV Seismic Network and other permanent networks. It includes a total of 350312 events with a magnitude estimation. Each event is located through the NonLinLoc Location code (Lomax et al. 2000), which performs a probabilistic non-linear location and provides accurate location uncertainties. The used model for velocities of waves is the one proposed by Di Stefano and Ciaccio 2014. The pros of this catalogue are the accurate locations of earthquake jointly with reliable uncertainties on the hypocenters; the main drawback is that the catalog is not homogeneous in magnitude. Indeed, all the declustering methods require a catalog with events having the same type of magnitude (different types of magnitude result in an uneven comparison between events). To overcome this issue it is applied a conversion to the moment magnitude M_w using the conversion relations presented in Gasperini, Lolli, and Vannucci 2013 and Lolli et al. 2020. In these works a conversion consists in linear relations between magnitudes:

$$M_w = A + BM \tag{6.3}$$

where M is the magnitude that has to be converted into M_w . The values of parameters A and B to convert the different magnitudes to M_w were taken from table 3 of the work by Gasperini, Lolli, and Vannucci 2013 and from table 9 of the work by Lolli et al. 2020. The Class catalogue in fact reports the type of magnitude for each magnitude, and this allowed us to use the equations developed in previous works and which form the basis of the HORUS catalogue (Lolli et al. 2020). Subsequently, in accordance with the binning of the magnitude provided by Class, we performed the magnitude round to classes of 0.1.

The total events are selected inside the previously defined polygon that includes the Apennines (see Figure 5.1). We exclude earthquakes in Vesuvio and Campi Flegrei areas, according to the masks defined in section 3.2, with the exception of the Colli Albani mask. Indeed, the exclusion of the Colli Albani area would have involved an abrupt cut on several clusters of extended seismicity across the mask; for this reason, it is preferred to retain seismic events inside this zone. In order to select events, which are interpreted as due to elastic strain accumulation and release, we consider events having an hypocentral depth not greater than 30 km. Furthermore, only events with errors on depth smaller than a threshold of 30 km are considered. The location uncertainties in the NonLinLoc Location code are due to the spatial relation between the network and the event, measurement uncertainty in the observed arrival times, and errors in the calculation of theo-

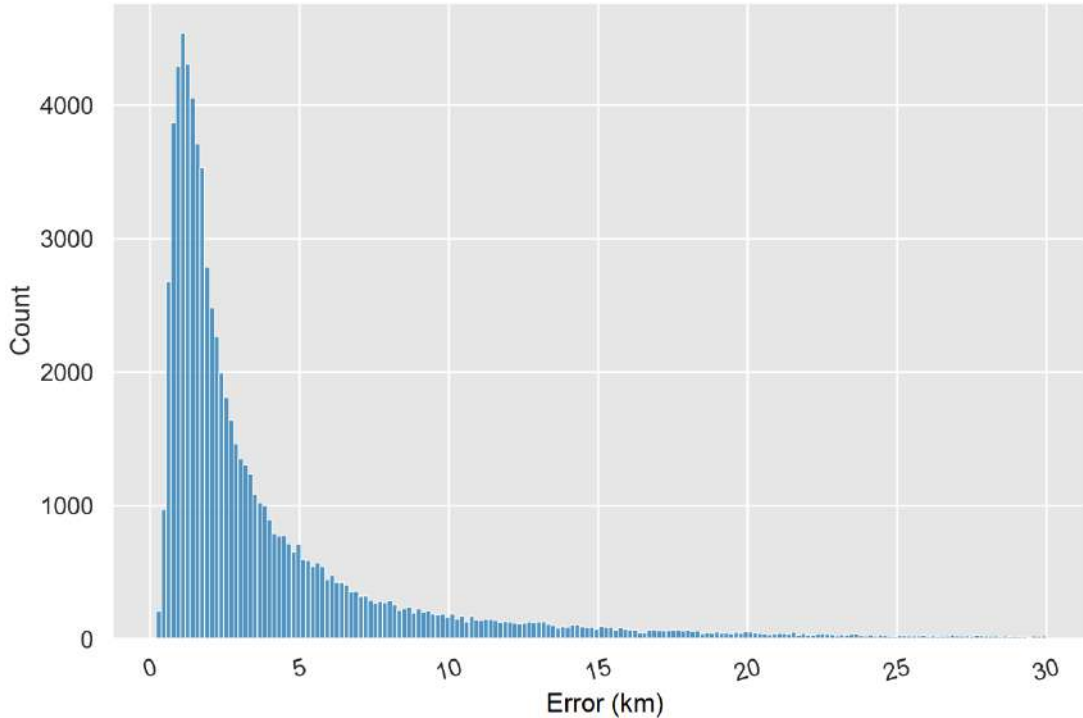


Figure 6.1: Distribution of the errors on depth of events in the CLASS catalog having depth and uncertainty on depth smaller than 30 km.

retical travel times. In this approach, the confidence ellipsoid is generated by the covariance matrix of the PDF scatter sample, and it represents the spatial error of location (Lomax et al. 2000). It is important to notice that correct evaluation of the errors is a complicated task (Garcia-Aristizabal et al. 2020). In fact, the error could be strongly affected by the velocity model, leading to very high errors in the case of an inadequate model of seismic wave propagation, whereas it could be lower than the reading errors where there are only a few time arrival readings. Figure 6.1 shows that only a few events show high values of error, with median values of 2.2 km. I have tested different thresholds for errors on depth and the results remain consistent.

The seismicity map resulting after these selections is shown in figure Figure 6.2. The declustering method described in the previous section is applied to the seismic catalog Figure 6.2 in order to include only independent events. Before proceeding with declustering on the catalog, it is necessary to know the completeness magnitude M_c of the catalog, i.e. the lowest magnitude such that in the considered area and time all seismic events with magnitude larger than M_c are recorded by the seismic network. There are several techniques for calculating the magnitude

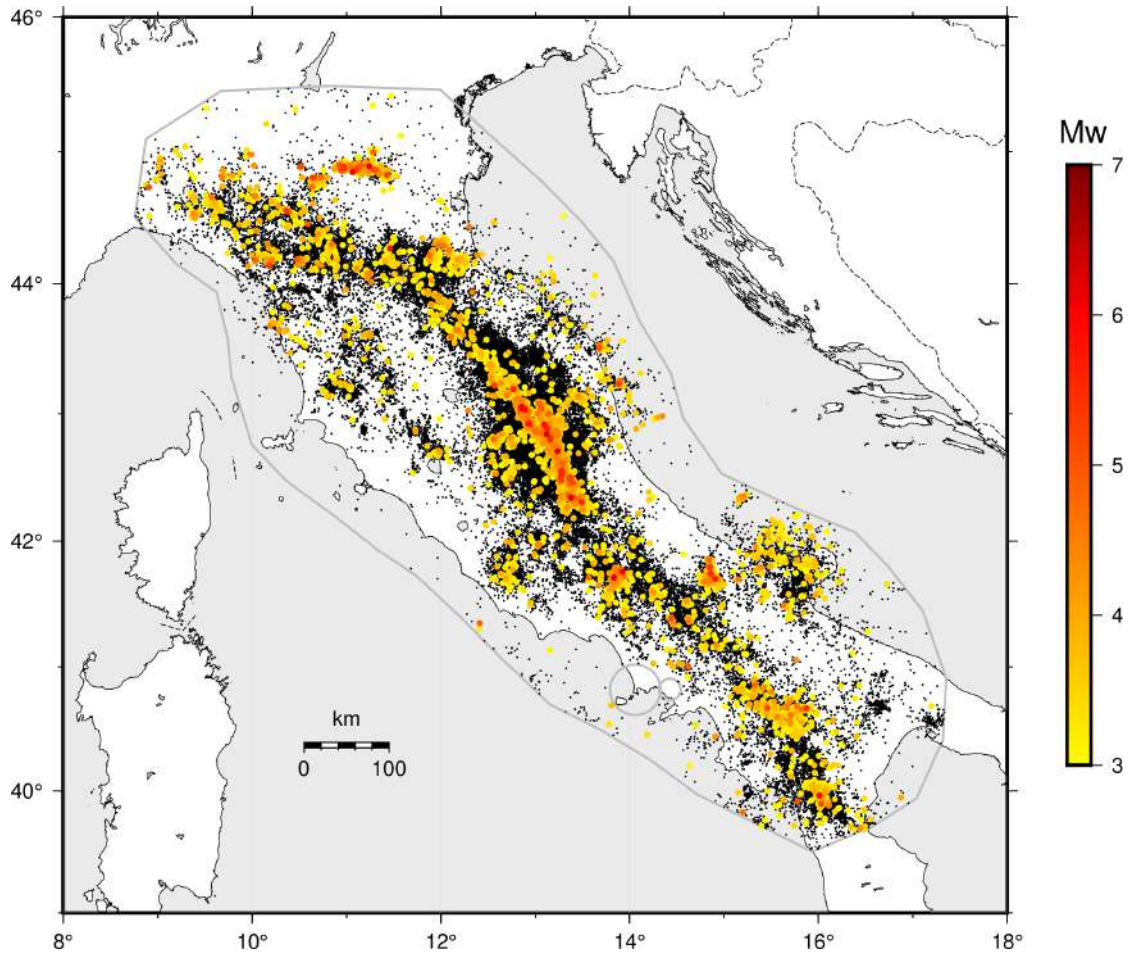


Figure 6.2: Map of the seismicity from CLASS catalog for earthquakes with depth less than 30 km. Black points are events with moment magnitude M_w less than 3; Colored circles are earthquake with magnitude greater than 3.

of completeness, which could lead to different values of the estimate. Mignan and Woessner 2012 provide a detailed analysis of the main algorithms available in literature. This thesis calculated M_c with the Goodness of fit test at 95% confidence bounds (Woessner and Wiemer 2005). The method to find M_c consists in a goodness of fit test, comparing the observed Frequency-magnitude distribution with synthetic G-R distribution for different M_c . When the observed distribution is modeled by the synthetic one at a certain confidence level we accept this M_c as completeness magnitude. Another parameter that has to be set is the b parameter of the G-R that appears in equation (6.1). The b parameter is estimated through the maximum likelihood estimator on the probability density function derived from the G-R law. In this thesis, the estimation of b is used as proposed by the work of Marzocchi and Sandri 2003. The computation of M_c and b is performed through the EPOS platform (Orlecka-Sikora, Lasocki, and Kocot 2020).

The completeness for the seismic catalog is analyzed in two different ways. First, the total catalog is used and $M_c = 1.8$ is obtained through a goodness of fit test at 95% of confidence interval. Subsequently, a year starting from which there is a substantial decrease of the M_c is searched; Amato et al. 2006 indicate 2005 as the year of a substantial improvement in the seismic network. A second analysis is then performed on the part of the catalog starting from the year 2005 and for which $M_c = 1.3$ is obtained (as before, through a goodness of fit test at 95% of confidence interval). The results of the analysis for these two data sets are presented in the following:

- The declustering method is applied on all the catalog from 1981 with magnitude greater than $M_c = 1.8$ including 76655 events. The G-R value of b is 0.90 and the resulting declustered catalog contains 19'330 events, i.e. $\sim 25\%$ of the starting catalog (they are shown in Figure 6.5). The resulting distribution of NND is shown in Figure 6.3. To decide if a fit with two Gaussian is better than a fit with only one the Akaike information criterion (AIC, Anderson, Burnham, and White 1998) was used. This method allows us to know which model, between the ones tested, fits better the data, on the basis of the AIC estimator value, which is the smallest one for the best model. In this case the AIC for a single Gaussian is 301395 while for two Gaussian is 289262; then two Gaussians significantly improve the fit.
- The declustering method applied on the filtered seismicity catalog from 2005 with magnitude greater than $M_c = 1.8$ includes 137446 events. The G-R value of b is 0.89 and the resulting declustered catalog contains 23396 events, i.e. $\sim 16\%$ of the starting catalog (they are shown in Figure 6.6). The resulting distribution of NND is shown in Figure 6.4. AIC for a Gaussian is 502904 while for two Gaussians is 492239.

For each catalog the two population of seismicity (independent and dependent) are distinguished through a cut-off in the intersection point between the two Gaussians. The dependent seismicity is shown in Figure 6.7 and Figure 6.8 respectively for the catalog from 1981 and from 2005.

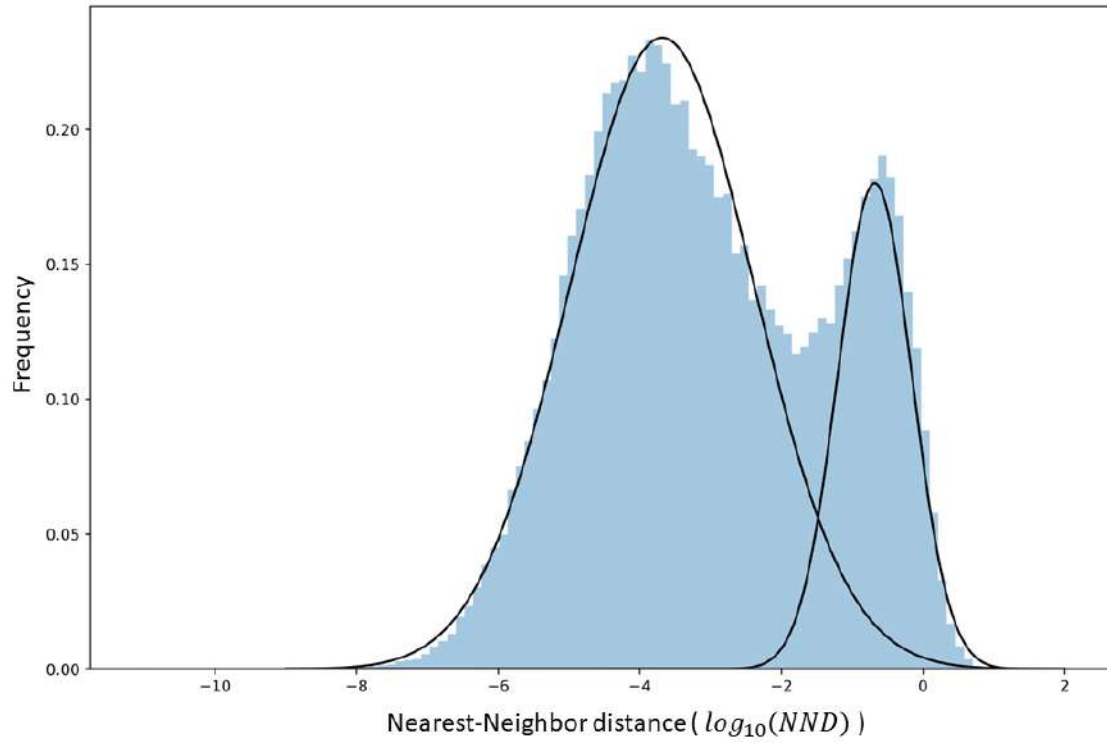


Figure 6.3: *Distribution of the nearest neighbor distances for the filtered seismic catalog from 1981 with $M_c = 1.3$ and $b = 0.90$.*

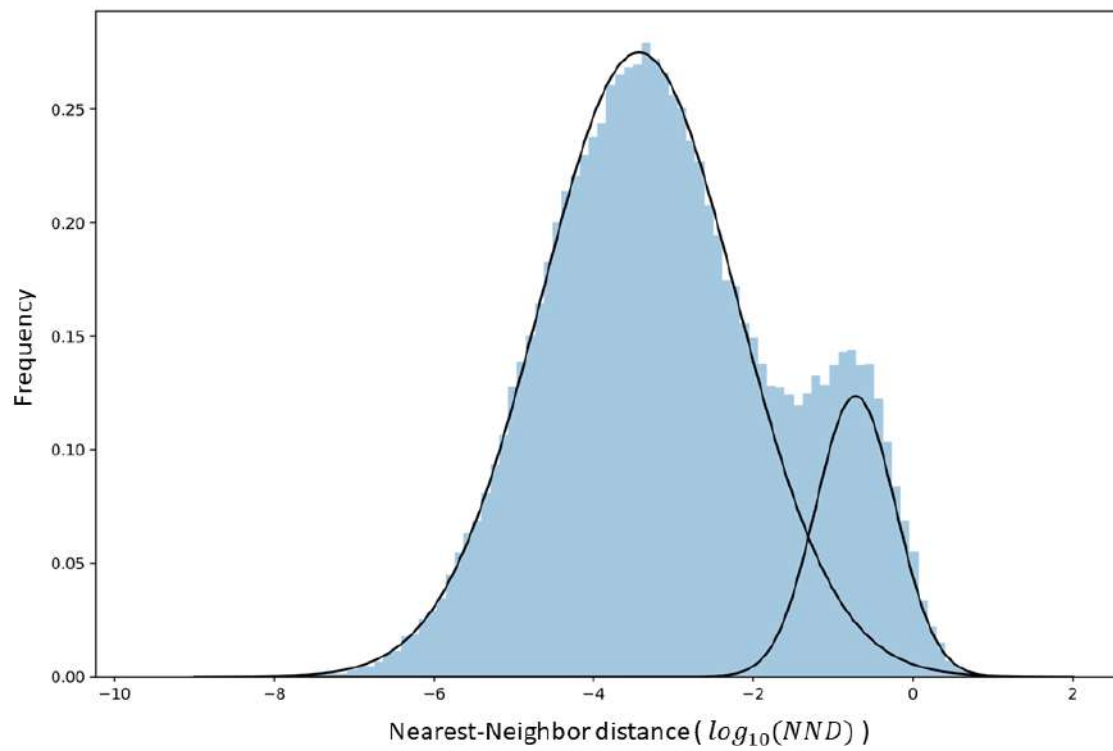


Figure 6.4: *Distribution of the nearest neighbor distances for the filtered seismic catalog from 2005 with $M_c = 1.3$ and $b = 0.89$.*

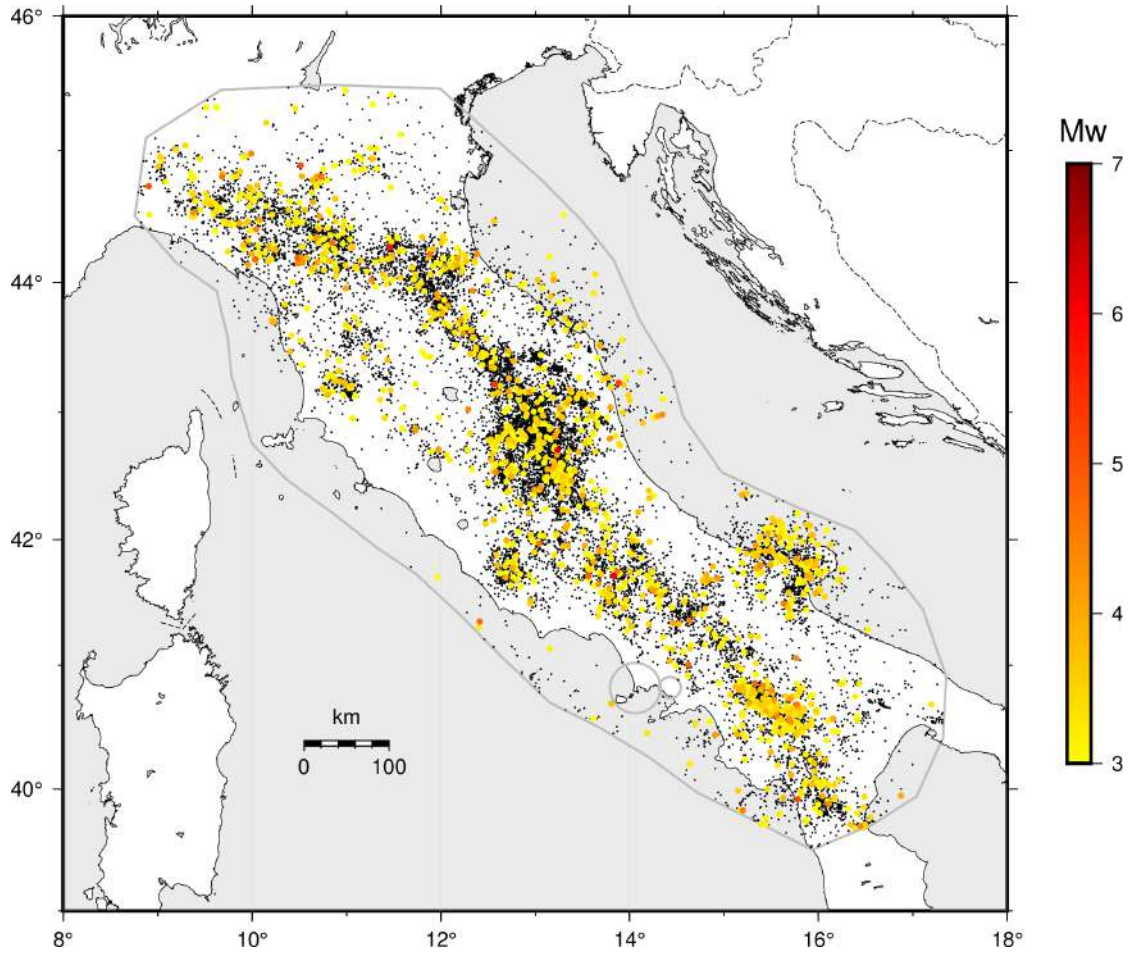


Figure 6.5: Map of the independent seismicity from CLASS catalog for earthquakes with depth less than 30 km from 1981 and completeness magnitude of 1.8. Black points are events with moment magnitude M_w less than 3; Colored circles are earthquake with magnitude greater than 3.

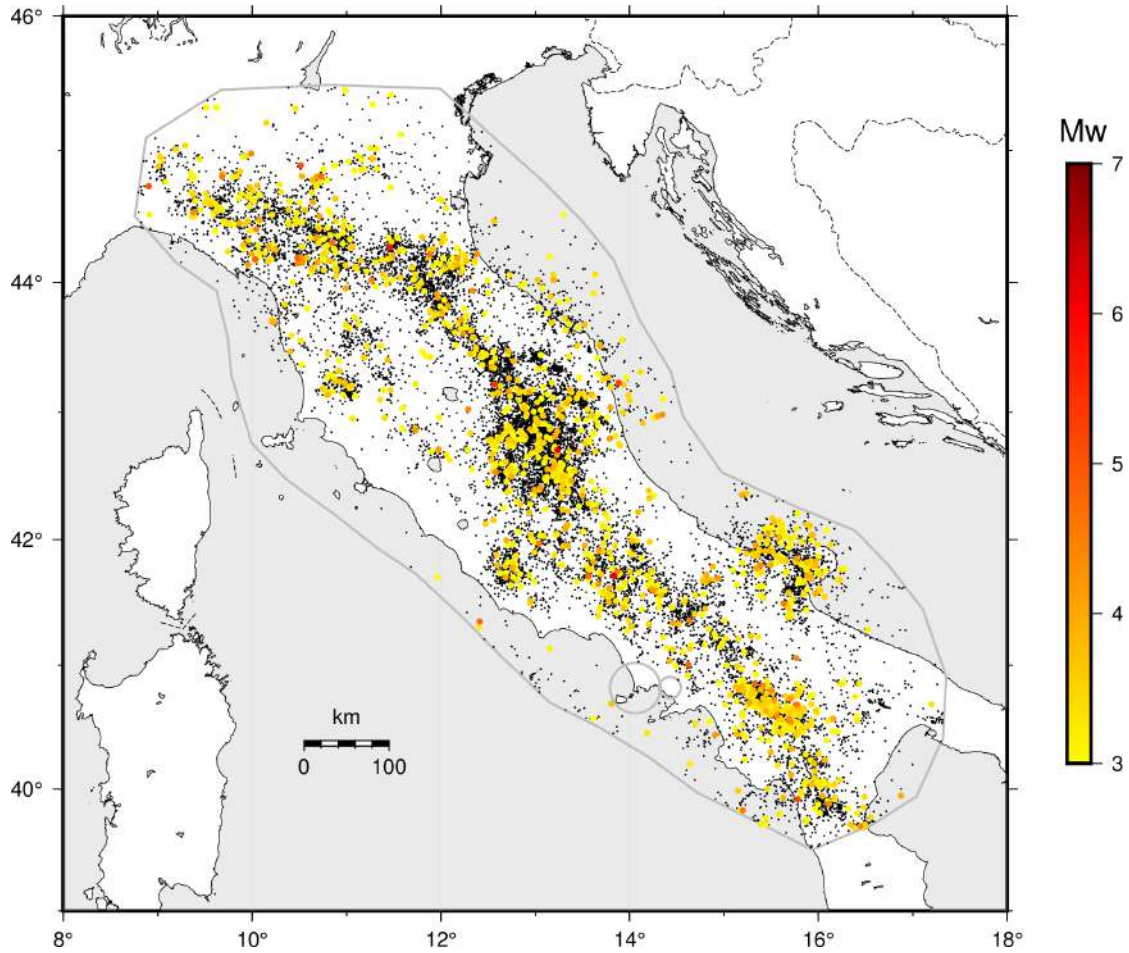


Figure 6.6: Map of the independent seismicity from CLASS catalog for earthquakes with depth less than 30 km from 2005 and completeness magnitude of 1.3. Black points are events with moment magnitude M_w less than 3; Colored circles are earthquake with magnitude greater than 3.

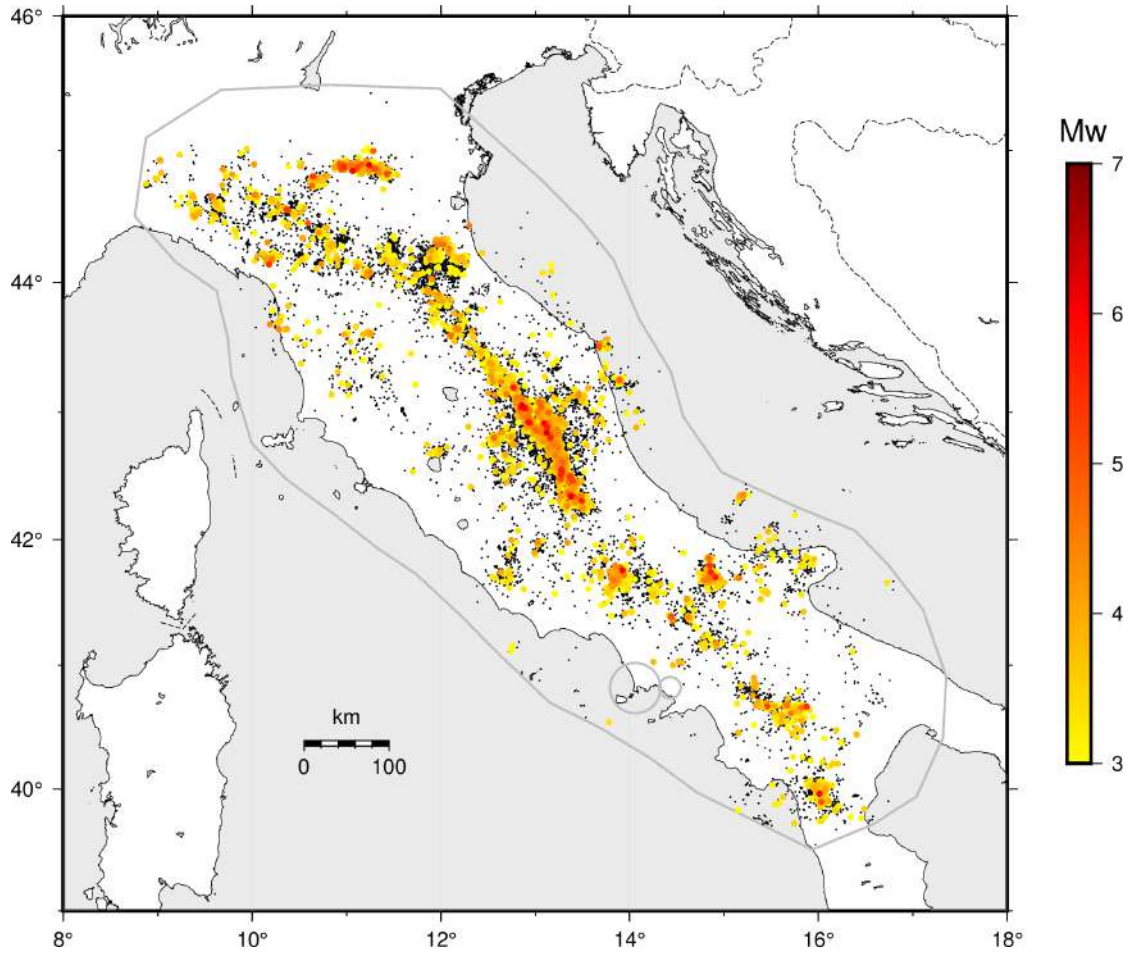


Figure 6.7: Map of the dependent seismicity from CLASS catalog for earthquakes with depth less than 30 km from 1981 and completeness magnitude of 1.8. Black points are events with moment magnitude M_w less than 3; Colored circles are earthquake with magnitude greater than 3.

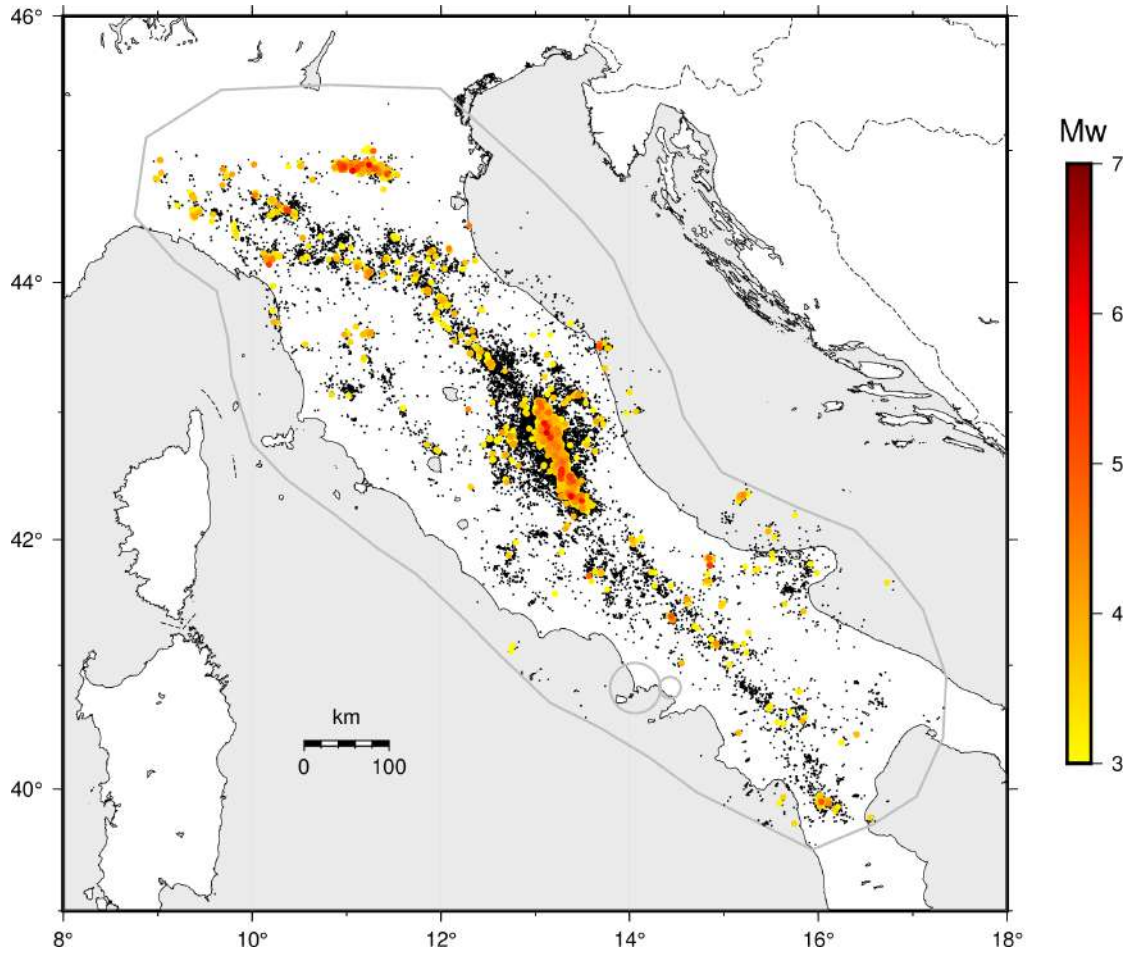


Figure 6.8: Map of the dependent seismicity from CLASS catalog for earthquakes with depth less than 30 km from 2005 and completeness magnitude of 1.3. Black points are events with moment magnitude M_w less than 3; Colored circles are earthquake with magnitude greater than 3.

6.3 Poisson distribution verification

In this section it is assessed if the events in declustered catalogs follow a Poisson process in time. A Poisson process has the property that the distance, in time, between couple of subsequent events follows an exponential distribution. We can then test for a Poisson process each independent catalog if inter-event times follow an exponential distribution in the form:

$$F(t; \bar{t}) = (1/\bar{t})e^{-t/\bar{t}} \quad (6.4)$$

where t is the inter-event time and \bar{t} is the mean inter-event time. Starting with the independent catalog from 1981, we graphically compare the distribution of observed inter-event times with an exponential distribution in the form of equation (6.4). The result is shown in Figure 6.9a. The visual agreement of the observed distribution with the exponential one is good for inter-event times smaller than 4 days but becomes poorer for longer time intervals. In particular, the observed distribution appears to be heavy tailed with respect to an exponential and seems to slightly underestimate the exponential distribution between 1.5 and 3 days.

The result for the independent catalog from 2005 is shown in Figure 6.9b. The agreement with an exponential distribution is good for inter-event times smaller than 1.2 days and, as before, the observed distribution is heavy tailed with respect to an exponential.

We can quantify the agreement with an exponential distribution through statistical tests. One possibility is the Anderson-Darling test that is a modification of the Kolmogorov-Smirnov (K-S) test that gives more weight to the tails of the distribution. Unfortunately, the observed distribution in Figure 6.9a and Figure 6.9b don't pass the test even at 0.01 significance level.

In conclusion, even if the visual agreement for the independent catalogs is good, the independent events don't formally follow a Poisson process. In Appendix, it is shown that Poissonianity is formally achieved considering threshold magnitudes greater than the completeness ones. However, considering the visual agreement as sufficient, we will employ the complete independent catalogs during the further analysis on the relationship between strain rate and seismicity rates. One advantage will be the possibility to make a more robust statistics on the events distribution in space, given the higher number of events.

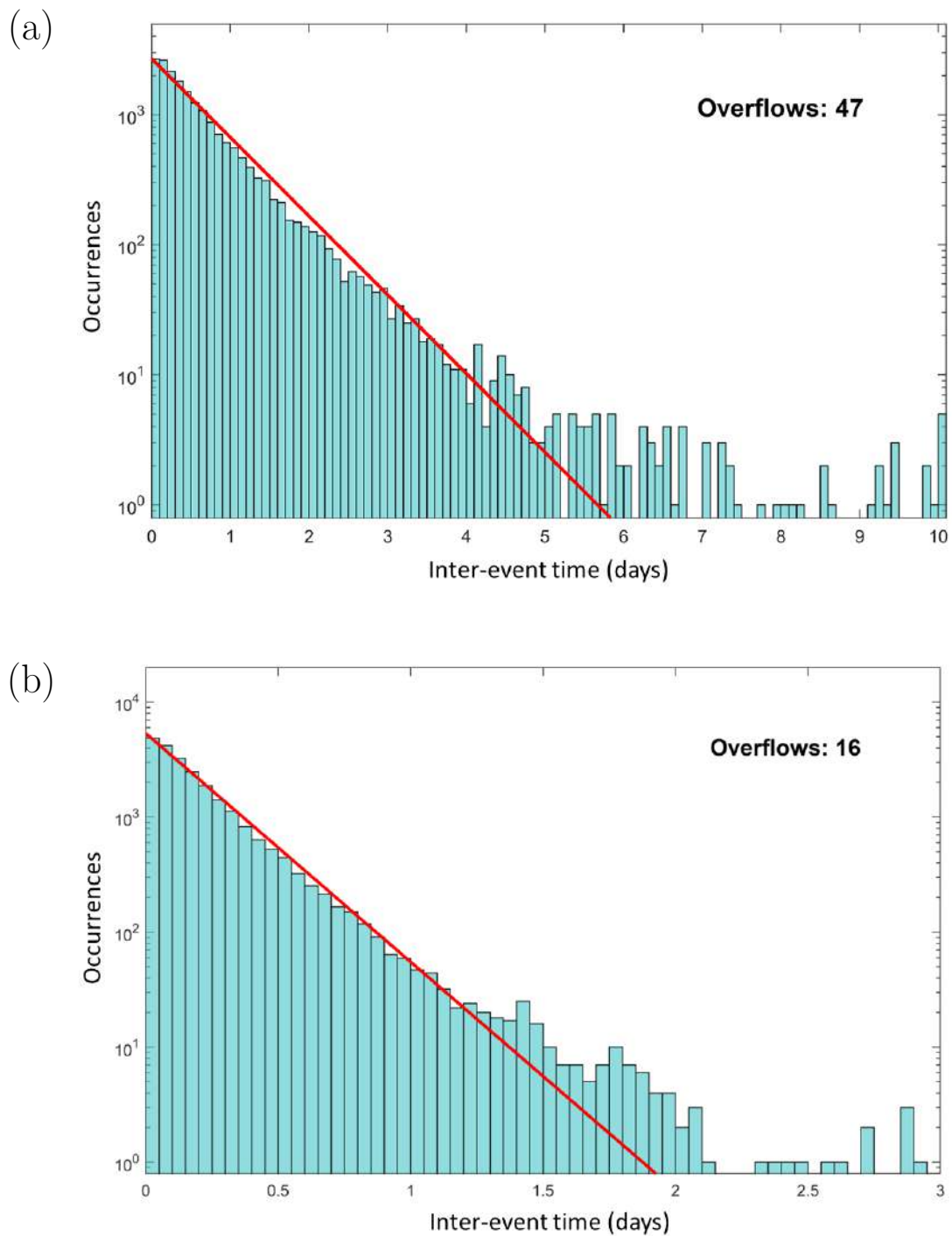


Figure 6.9: Histograms showing the distribution of inter-event times in days relative to: a) the independent catalog from 1981 and b) the independent catalog from 2005. Red line shows the expected distribution for a Poisson process. Overflows are the number of inter-event times greater than the maximum time shown on the horizontal axis.

Chapter 7

Relationship between strain rate and seismicity rate

In this chapter, the relationship between strain rate and seismicity rate in the Apennines is investigated following the approach of Stevens and Avouac 2021. Specifically, the two final hypotheses 4 and 5 will be tested, i.e. if:

- The earthquake spatial distribution has spatial density that depends, at first order, on the level of the deformation rate (section 7.1).

and if:

- The rate of earthquake nucleation is proportional to the geodetic strain rate (section 7.2).

Finally, in section 7.3, consequences that the relationship between seismicity rate and strain rate has on possible hazard estimates are discussed.

7.1 Spatial density of earthquakes and strain rate

After declustering, the distribution of independent (i.e., background) earthquakes in the polygon defined for the study area is not homogeneous (this is clear from Figure 6.5 and Figure 6.6). The hypothesis is that the spatial density of seismicity depends on the strain rate. According to this hypothesis, areas with similar values of deformation rates should have an homogeneous spatial density of events. In other terms, we expect an almost uniform distribution for events in areas with similar level of deformation rate. As indicator of the *level* of deformation rate, the second invariant of the geodetic strain rate I_2 is used (equation (2.6b)). Considering the I_2 map of strain rate derived from the wavelets method with $q_{max} = 8$

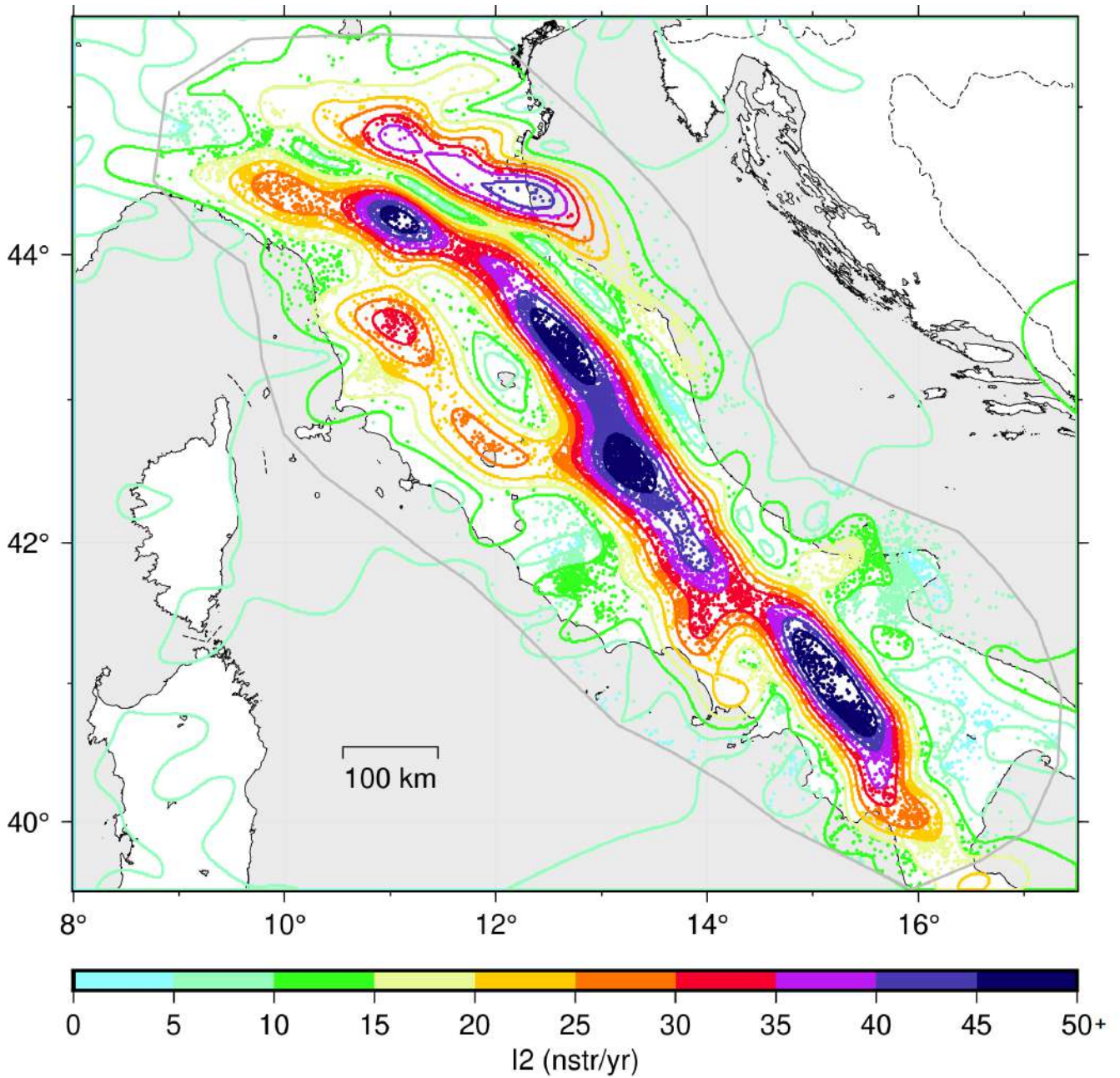


Figure 7.1: Contouring map of the distribution of I_2 , derived from geodetic strain rate, and seismicity, derived from the declustered catalog from 1981 (colored dots). The outer grey polygon defines the study region within which the declustering of the seismic catalog is performed. Both lines and dots are colored according to the intervals of I_2 and the last interval doesn't have an upper limit (≥ 45 nstr/yr)

(Figure Figure 4.13c), the total study area is divided into ten regions that correspond to ten different intervals of I_2 . The result is shown in Figure 7.1. The last interval, which starts from 45 *nstr/yr*, is considered up to the maximum value of the second invariant, in order to have corresponding areas that could be large enough to include a number of earthquakes sufficient to do statistical analyses. It can be noted that in the Po plain and in northern Adriatic an high value of second invariant I_2 does not correspond to an high nucleation rate. This can be reasonably addressed to a limited spatial coverage of the seismic network in that area (see Figure 7.2); on the other hand, the relatively high strain rate values in the northern Adriatic area are constrained by some GPS stations placed on platforms in the northern Adriatic and it is likely that the horizontal velocities of some of these stations are influenced by the on-site gas extraction activity. For these reasons, in order to not introduce a bias in the further analysis, the region of interest will be considered under 44°N of latitude in the following of this chapter.

Within each zone, we test if the seismicity is clustered or randomly distributed using the Ripley's K function. Given a set of N points distributed in a region having area A , the Ripley's K function depends on the spatial distance r and is defined as:

$$K(r) = \frac{1}{\lambda(N-1)} \sum_{i,j} I(d_{ij} < r) \quad (7.1)$$

where d_{ij} is the distance between the point i and j , $\lambda = N/A$ and $I(d_{ij} < r)$ is a function having value 1 if $d_{ij} < r$ and 0 otherwise. $K(r)$ defines how points are clustered for different investigation distances. To have a fair comparison between the observed distribution of points and a uniform distribution (inside a given region), the following steps are implemented:

- Given N observed points inside the region, N synthetic points are generated according to a uniform distribution using an *hit or miss* method: a rectangular box is considered that includes the region and random points inside this box are generated (points randomly distributed on a spherical surface); when a generated point falls inside the region it is kept and the procedure continues until we have N uniformly distributed points inside the area.
- The K-function for the simulated uniformly distributed points is computed according to equation (7.1) where the distance d_{ij} is the distance between points located on a sphere.
- The K-function for the observation points is computed, according to equation (7.1). The two obtained K functions, for the observed distribution and

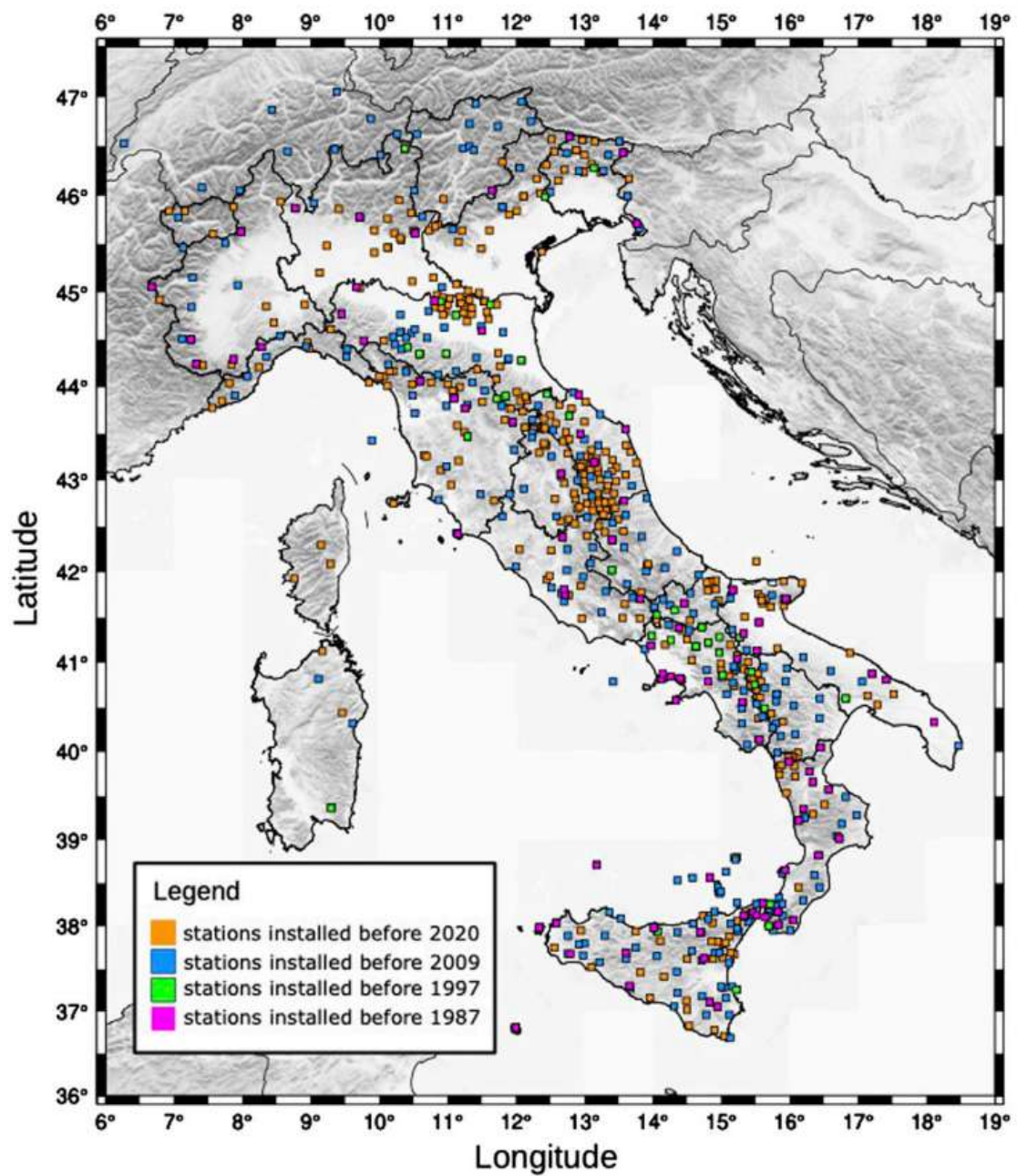


Figure 7.2: Temporal evolution of the deployment of monitoring seismic stations in Italy (from Garcia et al. 2021).

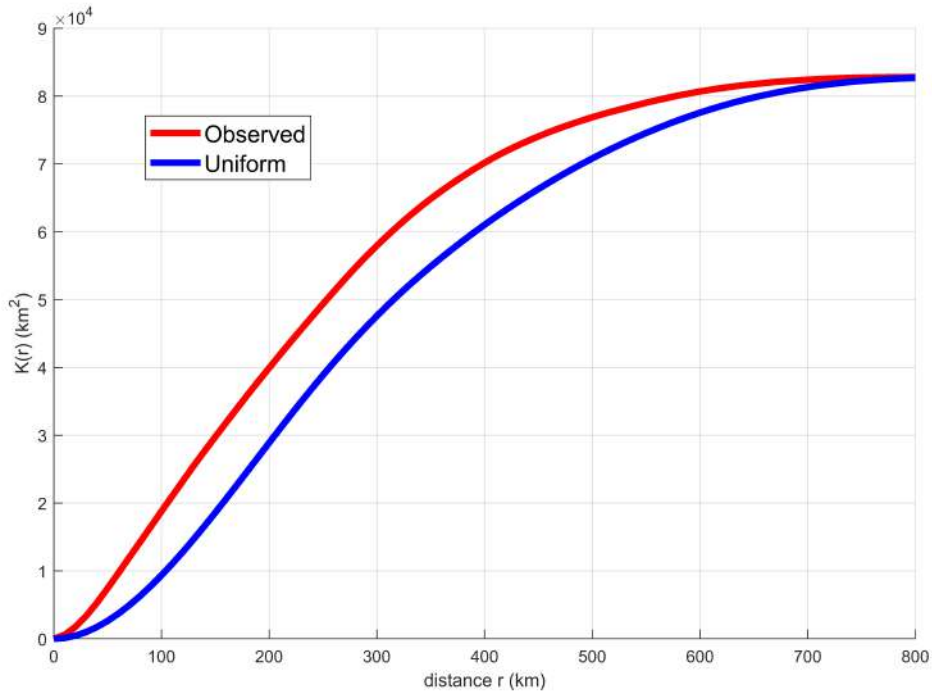


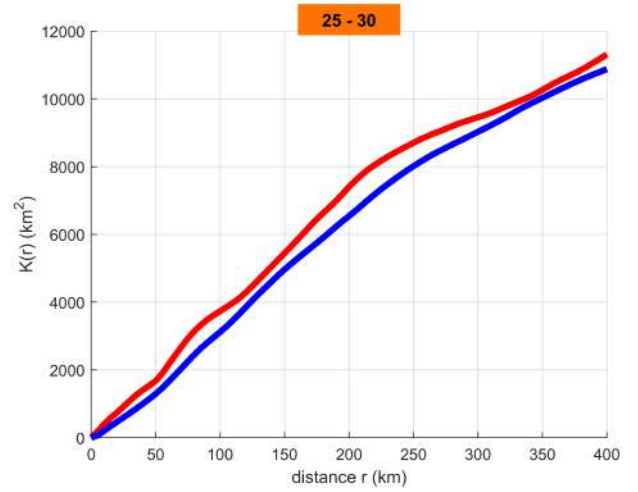
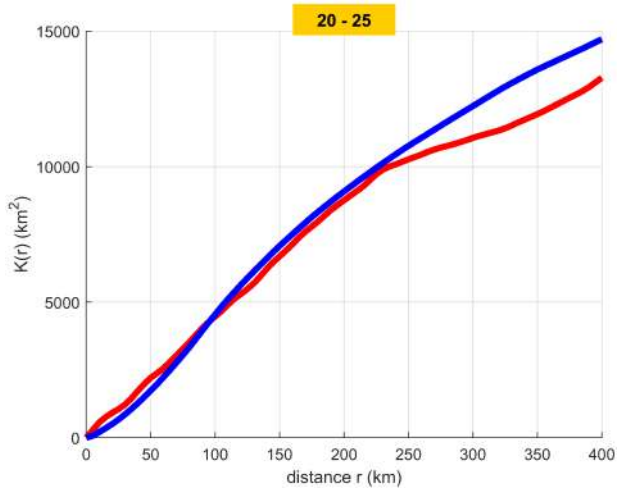
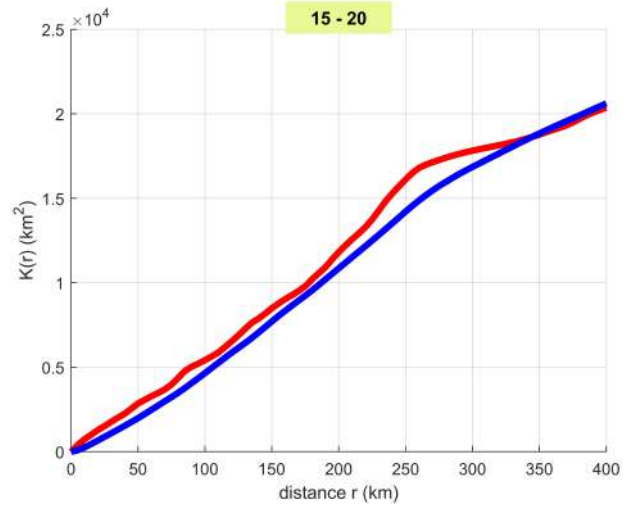
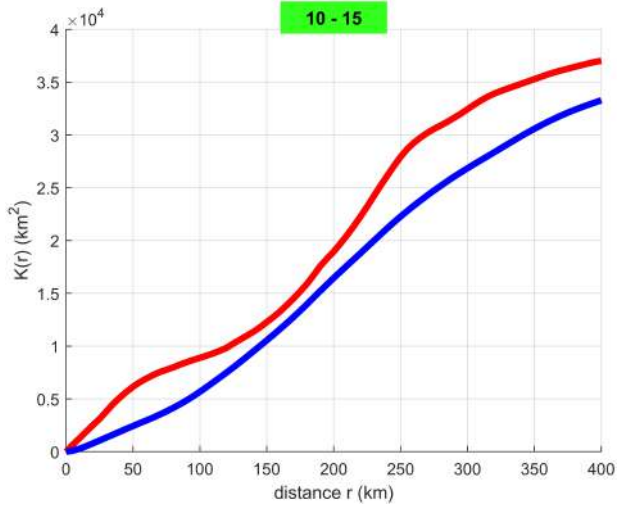
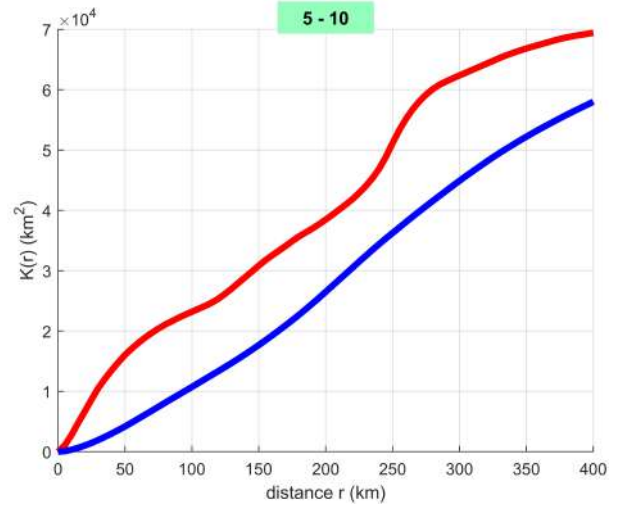
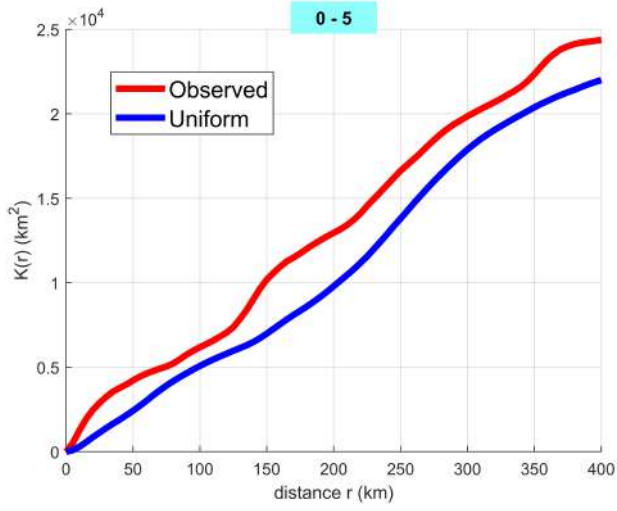
Figure 7.3: Ripley’s K functions for simulated points (blue line) from a uniform distribution within the grey polygon in Figure 7.1, considering the zone below 44° of latitude, and for the observed points (red line).

for the simulated uniform distribution, are then compared: if the observed distribution is uniform they should be close.

In this section, we consider the independent catalog from 1981 that covers a greater time span. However, similar results are obtained using the independent catalog from 2005.

The result of the analysis for the study region (for latitudes less than 44°N) is shown in Figure 7.3. As it was observed also by inspection of figure Figure 6.7, clustering is present at all the spatial distances. The results for the selected ten regions of strain rate are shown in Figure 7.4. There is a general good agreement between experimental and theoretical curves but the agreement on regions with low strain rate is poorer, as observed also by Stevens and Avouac 2021 for the Himalayan region. One explanation can be addressed to the difficulty to estimate very low values of strain rate from GPS data, since they imply only slight changes in velocity compared to the velocity uncertainty; contours for low strain area are then difficult to be drawn with precision. Excluding the first three regions of strain rate, the agreement with a uniform distribution is sufficiently good (except maybe

for the 40-45 nstr/yr region). In general, it is observed a significant improvement in uniformity with respect to the total distribution of events considering the whole area (Figure 7.3), even if is not possible to assume perfect homogeneity.



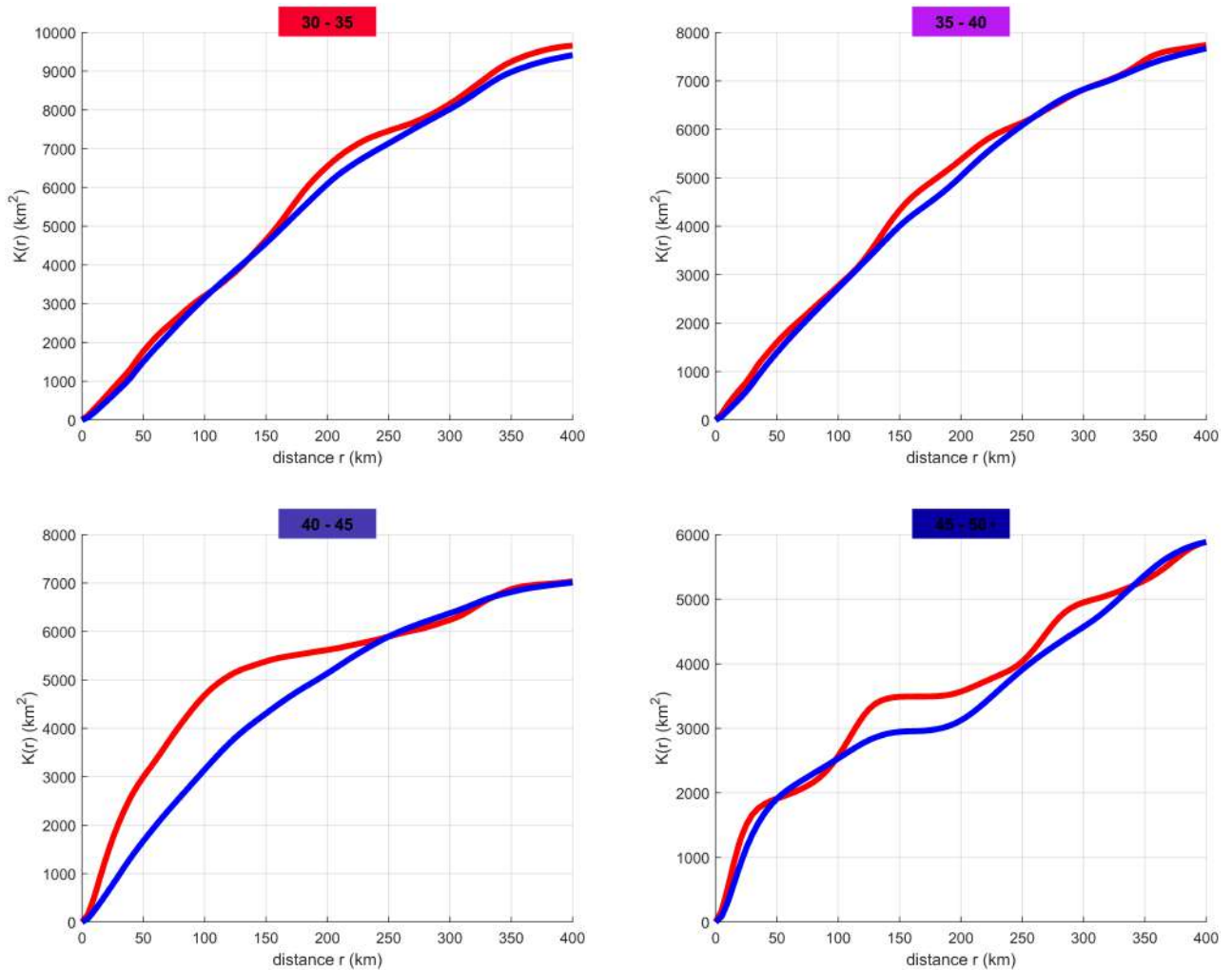


Figure 7.4: Ripley's K -functions of observed (red) and simulated data that follow a uniform distribution (blue); The ten plots refer to the ten regions with different strain rate shown in Figure 7.1 considering areas below 44° of latitude (intervals of strain rate are indicated by colored labels in nstr/yr)

7.2 Strain rate and seismicity rate

In order to investigate the the relationship between strain rate and seismicity rate (second hypothesis), we plot the seismicity rate per unit area in each region against the average strain rate inside that region. For the ten areas defined in Figure 7.1 the results are shown in figure Figure 7.5. Again, only areas and points under 44°N are considered. The simplest model to relate seismicity rate to strain rate is the one derived from Coulomb failure criterion (see section 2.4); a linear regression with 0 intercept is then performed on the data points in Figure 7.5 according to:

$$N_a = c_0 I_2 \quad (7.2)$$

where N_a is the seismicity per unit time and area while c_0 is a constant. I_2 is expressed in $nstr/yr$ while N_a in $1/(km^2yr)$. Seismicity rate per unit area and strain rate values show a linear correlation coefficient of 0.92 and it is found that a linear relationship between seismicity rate and strain rate produces $R^2 = 0.89$. Moreover, the null hypothesis for the F test, for which the slope is zero, is rejected with a p-value of $1.2 \cdot 10^{-5}$. These tests highlight that a linear relationship between seismicity rate and strain rate is able to explain a large part of the data variance.

Looking at Figure 7.5, it is reasonable to suppose a power-law relationship between strain rate and seismicity rate (as proposed also by Stevens and Avouac 2021) in the form:

$$N_a = c_1 I_2^{c_2} \quad (7.3)$$

The use of the power-law form leads to a decreasing of the residual standard error (RSE) from $18 \cdot 10^{-4}$ to $6.6 \cdot 10^{-4} (km^2yr)^{-1}$.

The choice of the width of the strain rate intervals that define the regions in Figure 7.1 has a certain degree of arbitrariness. Different interval sizes are shown in Figure 7.6. However, it is seen that the same pattern is preserved, even if a smaller interval size implies more dispersion of the points. Nevertheless, the linear fit and the power-law fit with the data provides very similar results (as it is seen in Figure 7.6 by the nearness of fit curves).

The resolution of the strain rate map influences the final result. A lower resolution map (from the wavelets method with $q_{max} = 7$, see section 4.3) and an higher resolution map ($q_{max} = 9$) are used to show this effect; the results, for the initial choice of strain intervals (Figure 7.1), under 44° latitude, are shown in Figure Figure 7.7. The plot relative to the map with $q_{max} = 7$ has one point less since the area between 40 and 45 $nstr/yr$ is too small to have a statistically significant number of data in its interior; the plot for the map with $q_{max} = 9$ has instead one more point since the medium value of strain rate is, in this case, higher: this

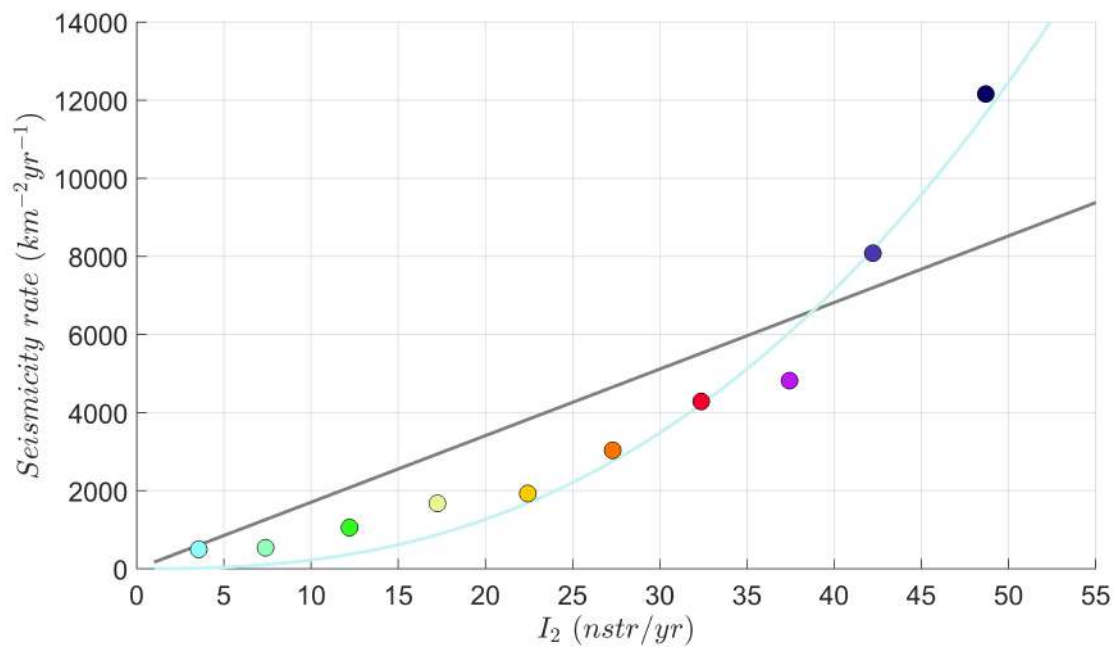


Figure 7.5: Relationship between strain rate and seismicity rate considering the ten regions of strain rate shown in Figure 7.1 (colored points); Grey line shows the linear fit having intercept 0 while light blue line shows the power-law fit.

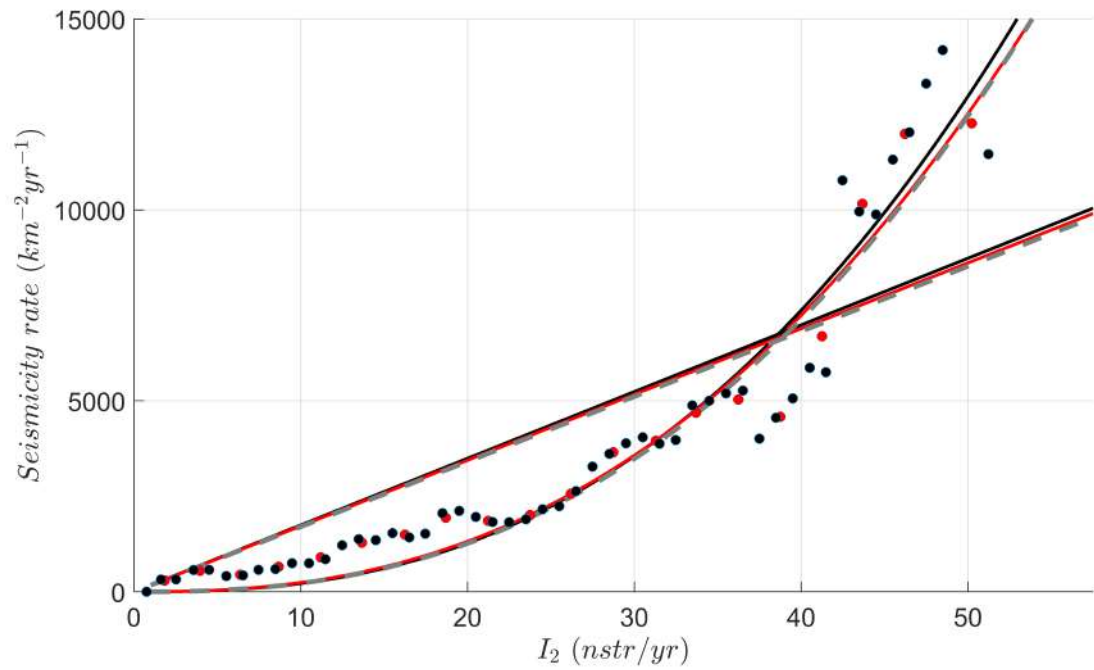


Figure 7.6: Relationship between strain rate and seismicity rate considering different strain rate intervals: 1 nstr/yr (black points) and 2.5 nstr/yr (red points). Linear and power-law fits for these points are superimposed to the ones in Figure 7.5 (dashed grey lines); black fit lines are referred to black points and red fit lines to red points.

q_{max}	c_0 (km^2 $nstr$) ⁻¹	R_{lin}^2	RSE_{lin} (km^2yr) ⁻¹	c_1 (km^2yr) ⁻¹	c_2	RSE_{p-law} (km^2yr) ⁻¹
7	$(2.0 \pm 0.4) \cdot 10^{-4}$	0.72	$33.6 \cdot 10^{-4}$	$(2 \pm 7) \cdot 10^{-12}$	(6 ± 1)	$12.2 \cdot 10^{-4}$
8	$(1.7 \pm 0.2) \cdot 10^{-4}$	0.89	$18.0 \cdot 10^{-4}$	$(7 \pm 6) \cdot 10^{-7}$	(2.5 ± 0.2)	$6.6 \cdot 10^{-4}$
9	$(1.54 \pm 0.09) \cdot 10^{-4}$	0.98	$9.7 \cdot 10^{-4}$	$(2.2 \pm 0.7) \cdot 10^{-5}$	(1.52 ± 0.08)	$3.9 \cdot 10^{-4}$

Table 7.1: *Fit results for the three map with different resolution. The events are from the declustered CLASS catalog from 1981.*

q_{max}	c_0 (km^2 $nstr$) ⁻¹	R_{lin}^2	RSE_{lin} (km^2yr) ⁻¹	c_1 (km^2yr) ⁻¹	c_2	RSE_{p-law} (km^2yr) ⁻¹
7	$(8 \pm 2) \cdot 10^{-4}$	0.67	$147.6 \cdot 10^{-4}$	$(7 \pm 20) \cdot 10^{-14}$	(7 ± 1)	$40.9 \cdot 10^{-4}$
8	$(7 \pm 1) \cdot 10^{-4}$	0.85	$84.8 \cdot 10^{-4}$	$(5 \pm 5) \cdot 10^{-7}$	(3.0 ± 0.3)	$29.1 \cdot 10^{-4}$
9	$(5.9 \pm 0.5) \cdot 10^{-4}$	0.94	$49.9 \cdot 10^{-4}$	$(5 \pm 3) \cdot 10^{-5}$	(1.7 ± 0.2)	$25.3 \cdot 10^{-4}$

Table 7.2: *Fit results for the three map with different resolution. The events are from the declustered CLASS catalog from 2005.*

allows the addition of the region between 45 and 50 $nstr/yr$. In Table 7.1 the fit results for the three different resolutions, using (7.2) and (7.3), are summarized. The same analysis is repeated for the events in the independent catalog from 2005. Considering this catalog the points patterns are very similar to the ones shown in Figure 7.5 and Figure 7.7 and the fit result for the three resolutions is exposed in Table 7.2.

The lower resolution map is not well fitted by none of the model proposed, as demonstrated by the low R^2 , the high uncertainties on the parameters and also by inspection of Figure 7.7a. For both the independent catalogs, the goodness of the linear fit increases with the resolution of the strain rate map. A possible explanation is that for greater resolutions of the strain rate map areas with high strain rate are larger and then the seismicity rate per unit area in these regions decreases. The values of c_0 become smaller with the increase of the resolution and, for each catalog, the resulting three values of c_0 , corresponding to three resolutions, are different but compatible within the errors. On the other hand, the power-law fit provides too different values of c_2 , the exponent of I_2 in equation (7.3), with varying the resolution, which are not comparable even taking into account their errors and values of c_1 having a large uncertainty. It can be even noted that, for both the fits, the agreement is poor for points with smaller I_2 where the models tend to underestimate the seismicity rates. For these reasons, in the next section will be considered the linear case stated by (7.2) and expected from the Coulomb failure criterion.

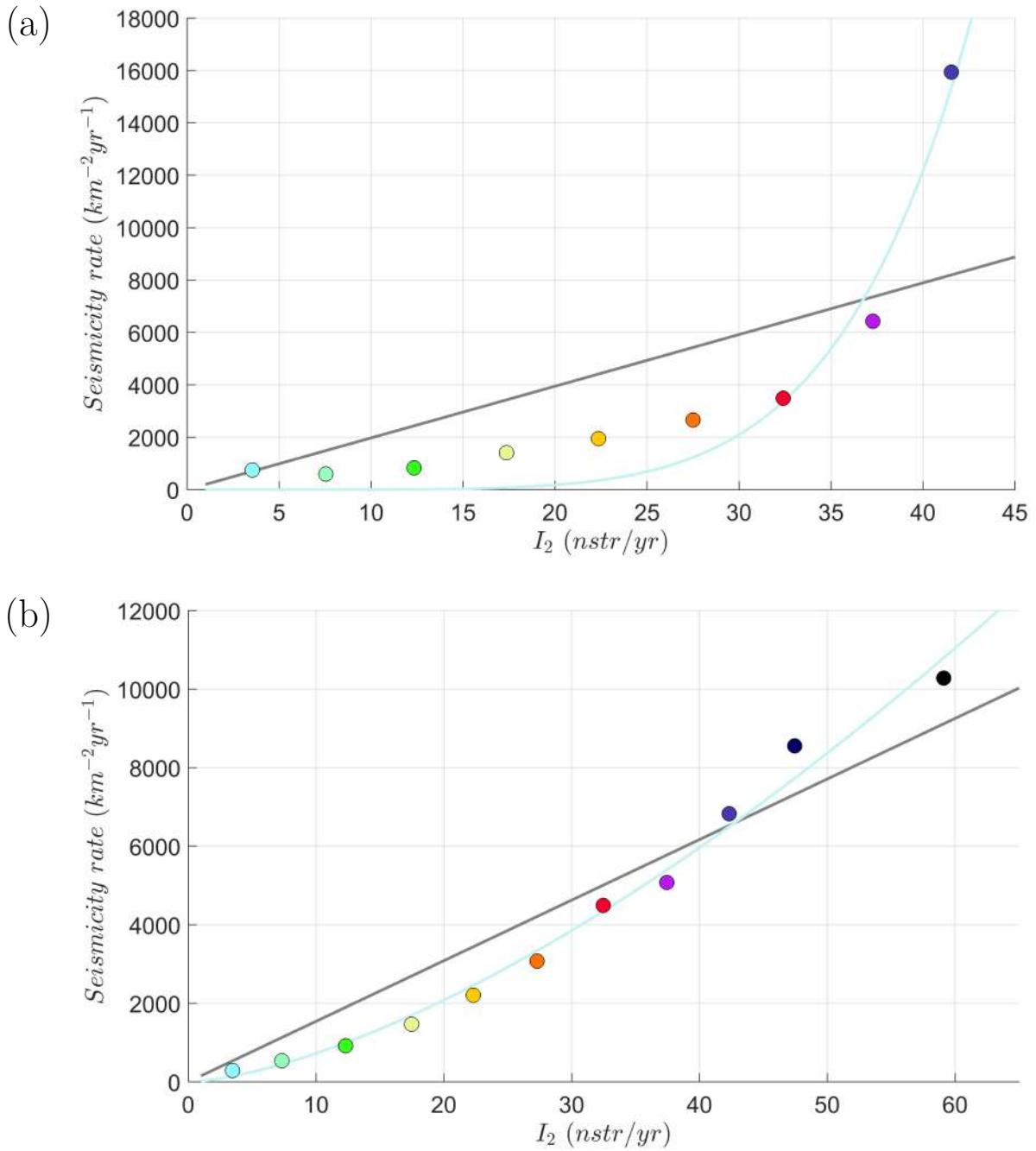


Figure 7.7: Relationship between strain rate and seismicity rate considering different resolutions of the second invariant map (colored points). a) $q_{max} = 7$, b) $q_{max} = 9$. Grey line shows the linear fit having intercept 0 while light blue line shows the power-law fit.

7.3 Implications for seismic hazard estimates

In this section I examine how the results obtained for the relationship between strain rate and seismicity rate impact on parameters that contribute to hazard estimates. From the Gutenberg Richter law evaluated for the completeness magnitude of the catalog we obtain:

$$\log_{10} N(M \geq M_c) = a - bM_c \quad (7.4)$$

where $N(M \geq M_c)$ is frequency of earthquakes with $M \geq M_c$ and a' is given by (2.15). The seismicity rate per unit area is related to the I_2 . Indicating with $f(I_2)$ this relationship, It is possible to write the previous equation as:

$$\log_{10} f(I_2)A = a' - bM_c \quad (7.5)$$

where A is the area for the region having mean second invariant equal to I_2 . From the knowledge of $f(I_2)$, the completeness magnitude M_c and b , it is possible to compute a' for the considered region. Remembering that $a' = a - \log_{10}(\Delta t)$ where Δt is the considered time-span i.e., the duration of one independent catalog, we can compute a as:

$$a = \log_{10} (f(I_2)A) + bM_c + \log_{10}(\Delta t) \quad (7.6)$$

This equation permits us to constrain the a value from the knowledge of I_2 if the functional form for the relationship between strain rate and seismicity rate is provided. In the previous section it was shown that a linear relationship between strain rate and seismicity rate can be appropriate for the Apennines, but with a dependence on the resolution of strain rate map; specifically, a good agreement is reached for $q_{max} = 8$ and $q_{max} = 9$. Considering these cases, the a -value for each region of strain rate is obtained through (7.6) and shown, for unit area, in Table 7.3. Observing Table 7.3 it's possible to note that there is an important dependence of the a values on the seismic catalog and a smaller dependence on the resolution of the strain rate map. The values of M_c and b likely may affect the estimate of parameter a shown in Table 7.3.

Let's now recall the equation (2.21) that is expression of the seismic moment conservation. If we substitute the a' value for the considered region from (7.6), we obtain:

$$M_w^{max} = \frac{1}{(1/c - b)} \left(-\frac{d}{c} + \log_{10} \alpha \dot{M}_0 + \log_{10} (1 - cb) - \log_{10} (f(I_2)A) - bM_c \right) \quad (7.7)$$

$I_2(nstr/yr)$	catalog from 1981		catalog from 2005	
	$q_{max} = 8$	$q_{max} = 9$	$q_{max} = 8$	$q_{max} = 9$
0-5	-6.04	-6.09	-6.30	-6.39
5-10	-5.72	-5.76	-5.98	-6.06
10-15	-5.50	-5.54	-5.77	-5.84
15-20	-5.35	-5.39	-5.62	-5.68
20-25	-5.24	-5.28	-5.50	-5.58
25-30	-5.15	-5.19	-5.42	-5.49
30-35	-5.08	-5.12	-5.34	-5.41
35-40	-5.01	-5.06	-5.28	-5.35
40-45	-4.96	-5.00	-5.23	-5.30
45-50	-4.90	-4.95	-5.16	-5.25
≥ 50	-4.90	-4.86	-5.16	-5.15

Table 7.3: Values of the a parameter of the Gutenberg Richter computed for unit area (considering equation (7.6) with $A = 1m^2$ and using the time lengths of the independent catalogs).

This equations provides a constraint on the maximum magnitude event from the knowledge of the relationship between strain rate and seismicity rate $f(I_2)$, the moment build-up rate \dot{M}_0 and the fraction α of the moment build-up rate that is released through seismic processes. Actually α and \dot{M}_0 are not easy to be estimated. \dot{M}_0 , for a single fault structure, has its formal expression in (2.10). Without specifying the fault structures, \dot{M}_0 can be related to the geodetic strain rate tensor, but the relationship is not unique (Savage and Simpson 1997). Stevens and Avouac 2021 use a relationship with the second invariant of the geodetic strain rate I_2 having the form:

$$\dot{M}_0 = c_g \mu T_s A I_2 \quad (7.8)$$

where c_g is a geometric factor that depends on the orientation and dip angle of the faults taking up the strain, μ is the rigidity of the medium, T_s is the *seismogenic thickness* and A is the area of the region having second invariant I_2 . For dip-slip faults:

$$c_g = 1/(\sin \delta \cos \delta) \quad (7.9)$$

where δ is the dip angle. Through equation (7.8), now the geometric factor c_g and

the seismogenic thickness T_s have to be set.

Equation (7.7) prescribes a dependence of the maximum magnitude on I_2 for a general relationship $f(I_2)$ between seismicity rate and strain rate. If $f(I_2) = c_0 I_2$, accounting for (7.8), (2.20) simplifies in:

$$M_w^{max} = \frac{1}{(1/c - b)} \left(-\frac{d}{c} + \log_{10} \alpha c_g \mu T_s + \log_{10} (1 - cb) - \log_{10} (c_0) - b M_c \right) \quad (7.10)$$

If c_g , α and T_s are assumed to be spatially constant, the previous relationship prescribes a single value of maximum magnitude for all the area inside the grey polygon in Figure 7.1. This may seem not intuitive; actually, even if the maximum magnitude is unique for all the regions with different strain rate, the *recurrence time* of the maximum magnitude event changes from one region to another (Stevens and Avouac 2021).

A first estimate of the maximum magnitude can be done assuming c_g , α and T_s constant with reasonable values for the Apennines. The parameters c and d are respectively set equal to $2/3$ and 6 . Since the presence of normal faults with $\sim 45^\circ$ of dip (recent earthquakes of Amatrice, Norcia and Colfiorito took place on faults approximately having this dip value), the geometric factor c_g can be set equal to 2 . According to the previous choice for the cut on the earthquakes' depth in the catalog, the seismogenic thickness T_s should be set equal to 30 km. Finally, α is set equal to 1 , meaning that aseismic moment release is negligible, while μ is set equal to 30 GPa. Using the linear relationship for a map having $q_{max} = 8$, which is the map that we have selected over the others in chapter 4, we obtain a maximum magnitude greater than 7.9 considering both the catalogs. This is clearly an unreasonable value for the Apennines. One possible wrong assumption is to consider the seismogenic thickness equal to 30 km. In fact, even if, during the catalog declustering, we considered only events with a depth less than 30 km, there are evidences that the seismogenic thickness for Apennines has values less than 30 km (Chiarabba and De Gori 2016). Considering as mean value for the seismogenic thickness 10 km we would obtain a first order more reasonable maximum magnitude values of 7.55 , for the catalog from 1981, and of 7.19 for the catalog from 2005. Still the value of 7.55 is greater than the magnitude value of the largest event in CPTI15 catalog (Rovida et al. 2022) while the estimate provided by 2005 seismic catalog seems to be more realistic. It's worth to notice that the seismic catalog from 2005 has a smaller magnitude of completeness than the catalog from 1981.

Moreover, constant values of c_g , α and T_s on all the study region could be an oversimplification for the Apennines. The geometric factor depends on the local geometry of the faults that vary through the Apennines. The seismogenic thickness

	reference value	percentage change	M_w^{max} % change
c_g	2	+25%	+2.2%
α	1	-25%	-2.9%
c_0	7	+14% or -14%	-1.3% or +1.5%

Table 7.4: *Relative changes of M_w^{max} for variations of the input parameters.*

T_s is not constant for the study region but has a spatial variability (Chiarabba and De Gori 2016) while α can be different from 1 for certain areas. A value for α equal to 1 can, in some cases, lead to overestimate the actual moment build-up rate. For example, there are evidences that the Alto-Tiberina fault is creeping (Anderlini, Serpelloni, and Belardinelli 2016) standing inside an area with high interseismic strain rate. To have an idea of what extent α , c_g and c_0 influence the estimate of the maximum magnitude, each uncertain parameter is varied by a certain percentage to see how the maximum magnitude estimate changes (Table 7.4). The allowed variability for c_0 is within the interval of uncertainty of this parameter according to Table 7.1. The reference configuration is the one with $T_s = 10\text{km}$, $\alpha = 1$, $c_g = 2$, $c_0 = 7$, $b = 0.89$ and $M_c = 1.3$ (using the independent catalog from 2005) that leads to a M_w^{max} of 7.19.

In this preliminary sensitivity test, we didn't examine the variability of M_w^{max} with respect to variations of b , T_s and M_c since, strictly, their variation is correlated to the seismicity rate estimate and then the c_0 estimate. Given the sensibility to the input parameters, an objective evaluation of the maximum magnitude can not disregard uncertainties of each parameter involved in (7.10). From Table 7.4 it can be noted that the parameters have a significant impact on the final estimate of the maximum magnitude. For example, a 2% change for M_w^{max} means, for this case, a magnitude change of ~ 0.14 , which is not negligible.

Chapter 8

Conclusions and future developments

In this thesis three different methods to estimate the horizontal geodetic strain rate field in the Apennines were examined. The preferred method is the one of Tape et al. 2009 that permits the generation of different strain rate maps based on a spatial length scale representing the GPS station's density. We retain that the map corresponding to a length scale of ~ 30 km ($q_{max} = 8$) can be the best compromise between robustness and resolution, avoiding, or minimizing, high strain rate concentrations due to local problems. However, the method, as the others examined, has a certain degree of subjectivity in the choice of the optimal resolution.

In the second part of this thesis I have examined if the geodetic strain rate is representative of the strain accumulated and released through earthquakes, ϵ_{ij}^R . It has been observed that the agreement between geodetic strain rates and ϵ_{ij}^R can hold for a first order comparison. This means that both hypotheses 1 (interseismic loading is stationary) and 2 (the geodetic strain rate reflects the stress rate), hold at first order. However, the distribution of orientations of principal axes of seismic strain from focal mechanisms shows a larger variability that can be mainly due to stress transfer mechanisms during earthquake sequences. We have also examined if independent events from declustering of the seismic catalog follow a Poisson distribution (hypothesis 3). This is verified reasonably well for both the independent catalogs, but formally only for threshold magnitudes larger than the completeness ones.

In the last part of this thesis, the spatial density of earthquakes has been studied to find the dependence on the strain rate as supposed by Stevens and Avouac 2021 (hypothesis 4). Dividing the study area in regions with different strain rate improves the spatial homogeneity of independent events inside each area with respect to the distribution on the overall area. On the other hand, the hypothesis of a formal uniform distribution inside each area seems to be too strong

for the Apennines.

A linear relationship between strain rates and seismicity rates (hypothesis 5) can well explain the observed variance only for enough high resolution strain rate maps ($q_{max} = 8$ and $q_{max} = 9$). This is an indication that different strain rate maps have a different impact on the relationship between strain rate and seismicity rate, which is an original result of the present thesis. In principle this relationship can provide important constraints on the seismogenic potential, for example allowing the estimates of the a parameter of the Gutenberg Richter law for different strain rate regions and the maximum allowed magnitude in the Apennine region. However, the last estimate is influenced by multiple parameters; among the others the aseismic fraction α that is not easy to be set.

This work is a first step in the analysis of the relationship between strain rate and seismicity rates in the Apennines. A future development of the method should consider a more accurate filter on seismic catalogs; for shallow earthquakes a depth cut-off of 30 km may be excessive and statistical distribution of earthquakes along depth could be considered. Moreover, one possibility is to use physical models to estimate the geodetic strain rate such as elastic block models, which accounts also for our knowledge on active faults. Finally, uncertainties and variations of important parameters, such as b and M_c , should be considered and formally propagated to the final results in order to estimate the uncertainties.

Appendix

For each independent catalog, considering events having magnitude greater than a threshold magnitude M_t (larger than the completeness one), the agreement between the observed inter-event time and an exponential distribution increases with respect to Figure 6.9a and Figure 6.9b. This can be verified by a visual comparison of Figure 8.1 and Figure 8.2, in which two values values of M_t are considered for each catalog, with Figure 6.9a and Figure 6.9b. At the same time, the agreement can be verified quantitatively through the Anderson-Darling test.

Starting with the independent catalog from 1981, we consider different values of M_t and we find that the statistical test is passed for $M_t = 3$ with a p-value of 0.09. This case is shown in Figure 8.1b. Considering the independent catalog from 2005, it is found that the test is passed for $M_t = 2.5$. This corresponds to Figure 8.2b and the test is passed with a p-value of 0.22.

The Poisson process in time is then formally verified for each catalog considering certain values of threshold magnitude M_t greater then the completeness magnitudes.

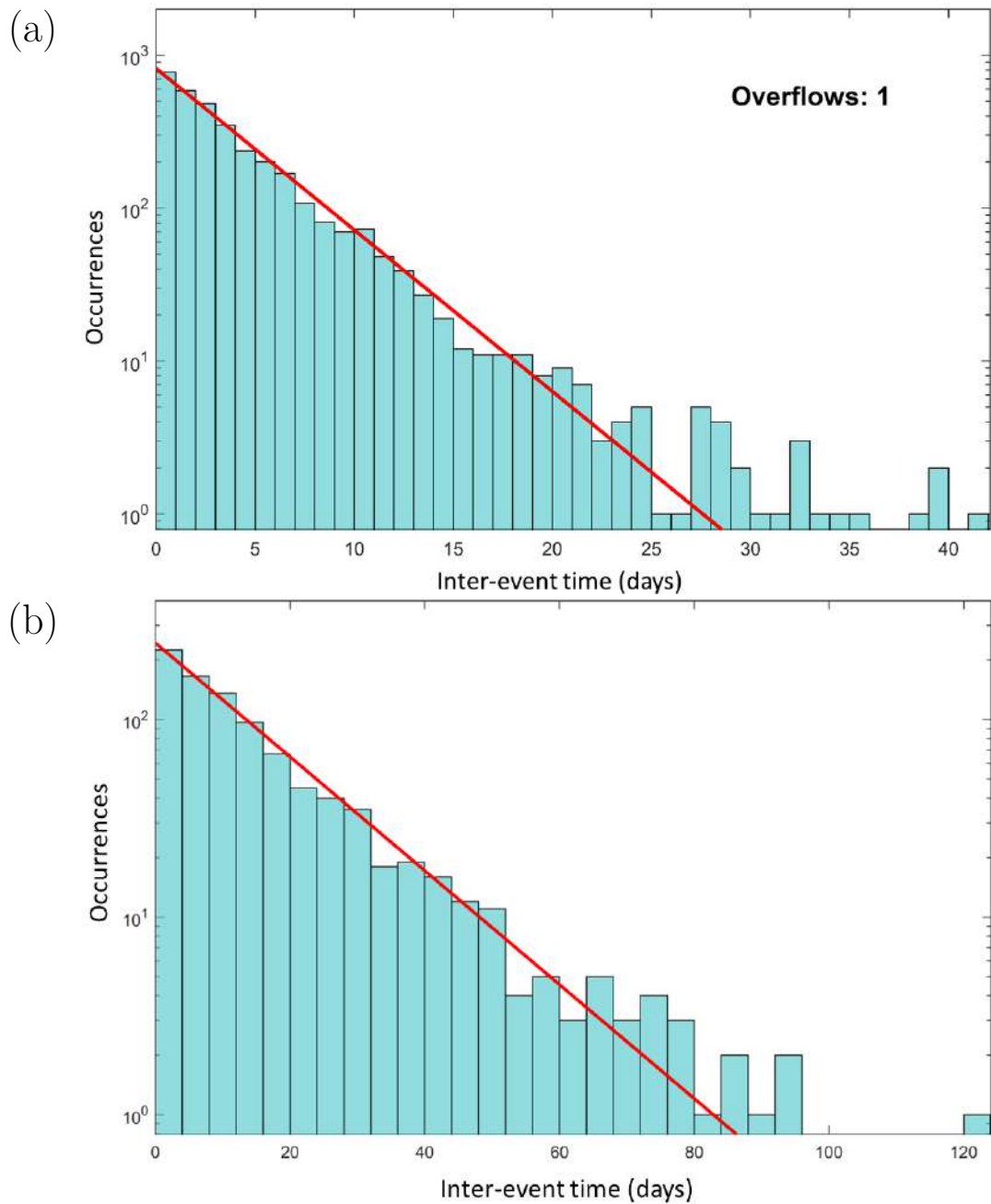


Figure 8.1: Histograms showing the distribution of inter-event times in days relative to the declustered catalog from 1981 and for two different threshold magnitudes: a) 2.5 c) 3. Red lines show the expected distribution for a Poisson process. Overflows are the number of inter-event times greater than the maximum time shown on the horizontal axis.

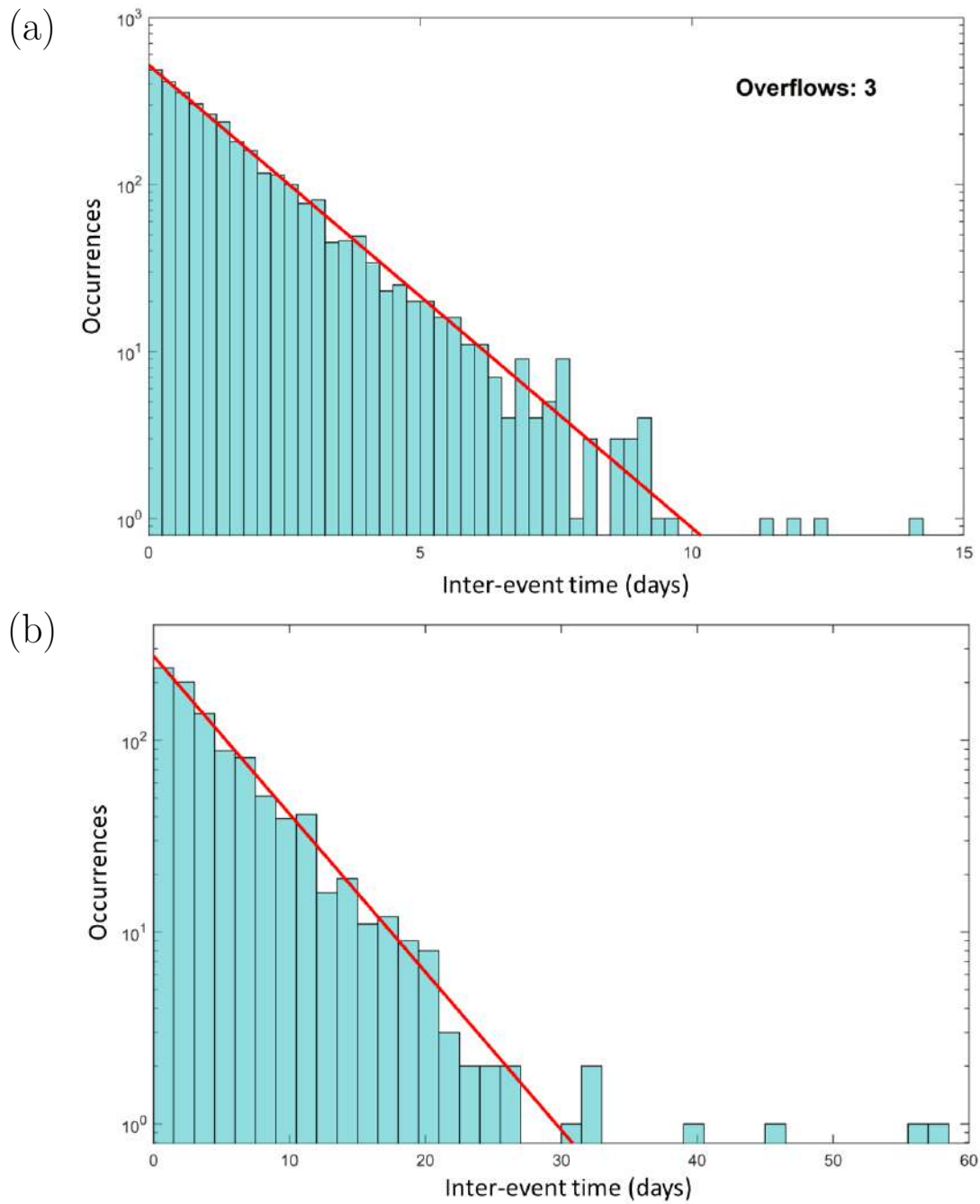


Figure 8.2: Histograms showing the distribution of inter-event times in days relative to the declustered catalog from 2005 and for different threshold magnitudes: a) 2 b) 2.5. Red lines show the expected distribution for a Poisson process. Overflows are the number of inter-event times greater than the maximum time shown on the horizontal axis.

Bibliography

- Ader, Thomas J., Lapusta, N., Avouac, J-P., and Ampuero, J-P. (2014). “Response of rate-and-state seismogenic faults to harmonic shear-stress perturbations”. In: *Geophys. J. Int* 198, pp. 385–413.
- Amato, A., Badiali L. and Cattaneo, M., Delladio, A, Doumaz, F, and Mele, F. (2006). “The real-time earthquake monitoring system in Italy”. In: *Géosciences* 4.
- Anderlini, L., Serpelloni, E., and Belardinelli, M. E. (2016). “Creep and locking of a low-angle normal fault: Insights from the Altotiberina fault in the Northern Apennines (Italy)”. In: *Geophysical Research Letters* 43.9, pp. 4321–4329. DOI: 10.1002/2016GL068604.
- Anderson, D., Burnham, K., and White, G. (1998). “Comparison of Akaike Information Criterion and consistent Akaike Information Criterion for model selection and statistical inference from capture-recapture studies”. In: *Journal of Applied Statistics* 25, pp. 263–282.
- Antonie, J.-P. and Vandergheynst, P. (1998). “Wavelets on the 2-Sphere: A Group-Theoretical Approach”. In: *Applied and Computational Harmonic Analysis* 7, pp. 262–291.
- Avouac, J.-P. (2015). “From Geodetic Imaging of Seismic and Aseismic Fault Slip to Dynamic Modeling of the Seismic Cycle”. In: *Annu. Rev. Earth Planet. Sci.* 43, pp. 233–271. DOI: 10.1146/annurev-earth-060614-105302.
- Bogdanova, I., Vandergheynst, P., Antonie, J-P., Jacues, L., and Morvidone, M. (2005). “Stereographic wavelet frames on the sphere”. In: *Appl. Comput. Harmon. Anal.* 19, pp. 233–252.
- Chiarabba, C. and De Gori, P. (2016). “The seismogenic thickness in Italy: constraints on potential magnitude and seismic hazard”. In: *Terra Nova* 28, pp. 402–408.

- Di Stefano, R. and Chiaraluce, L (2022). *Italian CataLogue of Absolute earthquakeS LocationS*. Report. INGV.
- Di Stefano, R. and Ciaccio, M. G. (2014). “The lithosphere and asthenosphere system in Italy as inferred from the Vp and Vs 3D velocity model and Moho map”. In: *Journal of Geodynamics* 82, pp. 16–25. DOI: <https://doi.org/10.1016/j.jog.2014.09.006>.
- Garcia, A., Faenza, L., Morelli, A., and Antoncicchi, I. (2021). “Can Hydrocarbon Extraction From the Crust Enhance or Inhibit Seismicity in Tectonically Active Regions? A Statistical Study in Italy”. In: *Front. Earth Sci.* 9. DOI: 10.3389/feart.2021.673124.
- Garcia-Aristizabal, A., Danesi, S., Braun, T., Anselmi, M., Zaccarelli, L., Famiani, D., and Morelli, A. (2020). “Epistemic Uncertainties in Local Earthquake Locations and Implications for Managing Induced Seismicity”. In: *Bull. Seismol. Soc. Am.* 110.5, pp. 2423–2440. DOI: 10.1785/0120200100.
- Gasperini, P., Lolli, B., and Vannucci, G. (2013). “Empirical Calibration of Local Magnitude Data Sets Versus Moment Magnitude in Italy”. In: *Bulletin of Seismological Society of America* 103.4, pp. 2227–2246. DOI: 10.1785/0120120356.
- Handwerger, A. L., Huang, M.-H., Fielding, E. J., Booth, A. M., and Bärghmann, R. (2018). “A shift from drought to extreme rainfall drives a stable landslide to strophic failure”. In: *Scientific reports* 9, pp. 1–12. DOI: 10.1038/s41598-018-38300-0.
- Kagan, Y. Y. (1991). “Fractal dimension of brittle fracture”. In: *Journal of Non-linear Science* 1, pp. 1–16. DOI: 10.1007/BF01209146.
- Kostrov, V. V. (1974). “Seismic moment and energy of earthquakes, and seismic flow of rock”. In: *Phys. Solid Earth* 1, pp. 13–21.
- Lolli, B., Randazzo, D., Vannucci, G., and Gasperini, P. (2020). “The Homogenized Instrumental Seismic Catalog (HORUS) of Italy from 1960 to Present”. In: *Seismological Research Letters* 91.6, pp. 3208–3222. DOI: 10.1785/0220200148.
- Lomax, A., Virieux, J., Volant, P., and Berge-Thierry, C. (2000). “Probabilistic Earthquake Location in 3D and Layered Models”. In: *Advances in Seismic Event Location*. Dordrecht: Springer Netherlands, pp. 101–134.
- Marzocchi, W. and Sandri, L. (2003). “A review and new insights on the estimation of the b-value and its uncertainty”. In: *Annals of Geophysics* 46.6, pp. 1271–1282.

- Materna, Kathryn, Maurer, Jeremy, and Sandoe, Lucy (Aug. 2021). *Strain_2D*. Version 1.0.0. DOI: 10.5281/zenodo.5240908.
- McCaffrey, Robert (2002). “Crustal Block Rotations and Plate Coupling”. In: *AGU Monograph*, pp. 1–40.
- Meletti, C, Marzocchi, W., D’Amico, V., Lanzano, G., Luzi, L., and Martinelli, F et al. (2021). “The new Italian Seismic Hazard Model (MPS19)”. In: *Annals of Geophysics* 64.1. DOI: 10.4401/ag-8579.
- Mignan, A. and Woessner, J. (2012). “Estimating the magnitude of completeness for earthquake catalogs”. In: *Community Online Resource for Statistical Seismicity Analysis*, pp. 1–45. DOI: 10.5078/corssa-00180805.
- Minelli, L., Billi, A., Faccenna, C., Gervasi, A., Guerra, I., Orecchio, B., and Speranza, G. (2013). “Discovery of a gliding salt-detached megaslide, Calabria, Ionian Sea, Italy”. In: *Geophysical research letters* 40, pp. 4220–4224. DOI: 10.1002/grl.50818.
- Molinari, I. and Morelli, A. (2011). “EPcrust: a reference crustal model for the European”. In: *Geophys. J. Int.* 185.1, pp. 352–364. DOI: dx.doi.org/10.1111/j.1365-246X.2011.04940.x.
- Orlecka-Sikora, B., Lasocki, S., and Kocot, J. et al. (2020). “An open data infrastructure for the study of anthropogenic hazards linked to georesource exploitation.” In: *Sci Data* 7.89. DOI: 10.1038/s41597-020-0429-3.
- Pondrelli, S., Visini, F., Rovida, A., D’Amico, V., Pace, B., and Meletti, C. (2020). “Style of faulting of expected earthquakes in Italy as an input for seismic hazard modeling”. In: *Nat. Hazards Earth Syst. Sci.* 20, pp. 3577–3592. DOI: 10.5194/nhess-20-3577-2020.
- Rovida, A., Locati, M., Camassi, R., Lolli, B., Gasperini, P., and Antonucci, A. (2022). “Catalogo Parametrico dei Terremoti Italiani (CPTI15), versione 4.0. Istituto Nazionale di Geofisica e Vulcanologia (INGV)”. In: DOI: 10.13127/cpti/cpti15.4.
- Sandwel, David T. (2010). *Comparison of Strain Rate Maps*. Research note. UCERF.
- Sani, F., Vannucci, G., Boccaletti, M., Bonini, M., Corti, G., and Serpelloni, E. (2016). “Insights into the fragmentation of the Adria Plate”. In: *Journal of Geodynamics* 102, pp. 121–138. DOI: dx.doi.org/10.1016/j.jog.2016.09.004.

- Savage, J. C. and Simpson, R. W. (1997). “Surface Strain Accumulation and the Seismic Moment Tensor”. In: *Bulletin of the Seismological Society of America* 87.5, pp. 1345–1353.
- Serpelloni, E., Cavaliere, A., Martelli, L., Pintori, F., Anderlini, L., Borghi, A., Randazzo, D., Bruni, S., Devoti, R., Perfetti, P., and Cacciaguerra, S. (2022). “Surface Velocities and Strain-Rates in the Euro-Mediterranean Region From Massive GPS Data Processing”. In: *Frontiers in Earth Science* 10. DOI: 10.3389/feart.2022.907897. URL: <http://hdl.handle.net/2122/15673>.
- Shen, Z.-K., Wang, M., Zeng, Y., and Wang, F. (2015). “Optimal Interpolation of Spatially Discretized Geodetic Data”. In: *Bulletin of the Seismological Society of America* 105.4, pp. 2117–2127. DOI: 10.1785/0120140247.
- Stevens, V. L. and Avouac, J.-P. (2021). “On the relationship between strain rate and seismicity in the India–Asia collision zone: implications for probabilistic seismic hazard”. In: *Geophys. J. Int.* 226, pp. 220–245.
- Stiphout, T. van, Zhuang, J., and Marsan, D. (2012). “Seismicity Declustering”. In: *Community Online Resource for Statistical Seismicity Analysis*. DOI: 10.5078/corssa52382934. URL: <http://www.corssa.org>.
- Tape, C., Muse, P., Simons, M., Dong, D., and Webb, F. (2009). “Multiscale estimation of GPS velocity fields”. In: *Geophysical Journal International* 179, pp. 1681–1698. DOI: 10.1111/j.1365-246X.2009.04337.x.
- Ward, S. N. (1994). “A Multidisciplinary Approach to Seismic Hazard in Southern California”. In: *Bulletin of the Seismological Society of America* 84.5, pp. 1293–1309.
- Woessner, J. and Wiemer, S. (2005). “Assessing the Quality of Earthquake Catalogues: Estimating the Magnitude of Completeness and Its Uncertainty”. In: *Bulletin of the Seismological Society of America* 95.2, pp. 684–698. DOI: 10.1785/0120040007.
- Zaliapin, Ilya and Ben-Zion, Yehuda (2013). “Earthquake clusters in southern California I: Identification and stability”. In: *Journal of Geophysical Research: Solid Earth* 118, pp. 2847–2864. DOI: 10.1002/jgrb.50179, 2013.
- Zecchin, M., Accaino, F., Ceramicola, S., Civile, D., Critelli, S., Da Lio, C., Magnano, G., Prosser, G., Teatini, P., and Tosi, L. (2018). “The Crotona Megalandslide, southern Italy: Architecture, timing and tectonic control”. In: *Scientific reports* 8. DOI: 10.1038/s41598-018-26266-y.

Ringraziamenti

Vorrei ringraziare la Prof.ssa Maria Elina Belardinelli e il Dott. Enrico Serpelloni per avermi dedicato tempo e affiancato in questi mesi di tirocinio.

Un doveroso *grazie* alla Dott.ssa Licia Faenza e al Dott. Alexander Garcia per il fondamentale aiuto nell'analisi del catalogo sismico e per aver condiviso con me importanti riflessioni.

Ringrazio i miei amici, in particolare Serena e Andrea.

Ringrazio i miei genitori Germana e Giuliano che mi hanno sostenuto in questi anni e mia sorella Asia che ha dato colore a molte delle mie giornate.